BERGISCHE
UNIVERSITÄT
WUPPERTAL

Investigation of Brake Wear Particle Emissions on the Dynamometer and the Vehicle under Real-Driving Simulation

Inauguraldissertation

zur Erlangung des akademischen Grades

Doktor der Naturwissenschaften
(Dr. rer. nat.)

an der Fakultät für Mathematik und Naturwissenschaften
der Bergischen Universität Wuppertal

vorgelegt von
Ferdinand H. Farwick zum Hagen, M.Sc.
aus Münster

Wuppertal, 2019

The PhD thesis can be quoted as follows:

urn:nbn:de:hbz:468-20200616-090157-0
[http://nbn-resolving.de/urn/resolver.pl?urn=urn%3Anbn%3Ade%3Ahbz%3A468-20200616-090157-0]

DOI: 10.25926/f1j5-fp87
[https://doi.org/10.25926/f1j5-fp87]

Die vorliegende Arbeit wurde in der Zeit von September 2015 bis Oktober 2018 am FORD Research and Innovation Center, Aachen, in Zusammenarbeit mit der Physikalischen und Theoretischen Chemie der Fakultät Mathematik und Naturwissenschaften der Bergischen Universität Wuppertal angefertigt.

Erster Gutachter: Univ.-Prof. Dr. Thorsten Benter

Zweiter Gutachter: Priv.-Doz. Dr. Rainer Vogt

Danksagung

Mein besonderer Dank gilt meinem Betreuer, Priv.-Doz. Dr. Rainer Vogt, für die interessante Aufgabenstellung, das Interesse an der Arbeit und das entgegengebrachte Vertrauen. Ich danke für die kompetente Unterstützung bei wissenschaftlichen Fragestellungen und den offenen Umgang miteinander.

Bei Prof. Dr. Thorsten Benter möchte ich mich für die unkomplizierte akademische Betreuung seitens der Bergischen Universität Wuppertal bedanken.

Dr. Marcel Mathissen danke ich für die hilfreichen Diskussionen, Anregungen und kritischen Fragestellungen, die zum Erfolg dieser Arbeit beigetragen haben. In diesem Zusammenhang möcht ich ebenfalls Volker Scheer und Dr. Ulf Kirchner dankend erwähnen.

Bei Herbert Ernst und seinem Werkstatt-Team möchte ich mich für die vielen technischen Ratschläge bedanken.

Den Kollegen von Core-Brake, insbesondere Dr. Tomasz Grabiec und Dr. Jaroslaw Grochowicz, möchte ich für die Unterstützung meiner Arbeit am Entwicklungszentrum Köln-Merkenich danken. Für den professionellen technischen Support im Brake-Lab danke ich Christian Schmidt und seinem Team.

Ein großes Dankschön möchte ich den Kollegen von den Ford Lommel Proving Grounds, allen voran Filip De Corte, aussprechen, die durch Ihre Kreativität alle Änderungswünsche am Testauto umgesetzt und mich sicher auf die Testfahrten vorbereitet haben.

Der Ford Motor Company danke ich für die finanzielle Unterstützung.

Mein größter Dank gilt meiner Familie. Durch Euch habe erst gelernt meine Arbeit im richtigen Licht zu betrachten. Besonders möchte ich Dir, Johanna, danken für das Zuhören, die Geduld und die lieben Worte auch an weniger guten Tagen.

Darüber hinaus möchte ich mich herzlich bei meinen Eltern und Geschwistern bedanken. Ihr habt mir im Leben viel ermöglicht, mich unterstützt und wart stets für mich da. Dafür danke ich Euch sehr.

Ich bedanke mich bei allen Verwandten, Freunden und Bekannten, die für den nötigen Ausgleich neben der Arbeit sorgten und menschlich für mich da waren.

Herzlichen Dank!

„Suche nicht nach Fehlern,
suche nach Lösungen.“

Herny Ford

Kurzzusammenfassung

Partikelemissionen durch Bremsenabrieb tragen zur Luftverschmutzung bei und gelten neben Staub von Reifen- und Straßenabrieb sowie Resuspension als hauptsächlicher Verursacher von Nicht-Abgasemissionen im Straßenverkehr. Bremspartikelemissionen werden zwar wissenschaftlich untersucht, allerdings hat sich bislang noch kein standardisiertes Messverfahren etabliert, welches einen direkten Vergleich von Ergebnissen ermöglicht. Insbesondere sind die Kenntnisse von Partikelemissionen unter realistischen Fahrbedingungen sehr begrenzt.

Im Rahmen dieser Arbeit wurden zwei Prüfaufbauten zur Untersuchung von Bremspartikelemissionen entwickelt, umfangreich getestet und angewandt: Ein Aufbau wurde für Messungen unter Laborbedingungen am Bremsenprüfstand konzipiert und ein weiterer für Messungen am Fahrzeug im realen Fahrbetrieb. Für beide Aufbauten wurde ein identisches Messkonzept gewählt, welches vorsah, den gesamten luftgetragenen Bremsenabrieb zu erfassen. Der Bremsenabrieb wurde geschlossen zur Messstelle transportiert, wo er mit hoher Zeitauflösung mittels unterschiedlicher Geräte hinsichtlich der Partikelgröße und -masse analysiert wurde. Eine parallele Überwachung der Volumenströme ermöglichte es, die Emissionen zu quantifizieren und Emissionsfaktoren zu ermitteln, durch die eine hohe Vergleichbarkeit erzielt wird. Die Durchführung der Messreihen erfolgte primär mit realistischen Fahrzyklen, sodass die Ergebnisse als repräsentativ für reales Fahren erachtet werden können.

Für die Vorderradbremse eines Mittelklassewagens beliefen sich die Emissionsfaktoren für Partikelmasse (PM_{10}) auf 4.5 mg km^{-1} und für Partikelanzahl auf 1-9$\times 10^{10}$ km^{-1} pro Bremse. Das Emissionsverhalten der Bremse unter erhöhten Temperaturen wurde ebenfalls untersucht, welches maßgeblich die Entstehung von ultrafeinen Partikeln begünstigt. Die Realfahrtmessungen zeigten jedoch, dass für normales Fahren diese hohen Bremstemperaturen nicht erreicht werden und folglich die Bildung von ultrafeinen Partikeln als unwahrscheinlich zu bewerten ist. Darüber hinaus wurden die Ursachen von Emissionen während Beschleunigungsphasen und Konstantfahrten ermittelt.

Abstract

Brake wear particle emissions contribute to ambient air pollution. Besides tire wear, road wear, and dust from resuspension, brake wear has been identified as essential source of non-exhaust traffic related emissions. Although brake wear emissions are scientifically investigated, no standardized measurement method has yet been established, which allows a direct comparison of the results. In particular, the knowledge on wear emissions under realistic driving conditions is very limited.

Within the scope of the present thesis, two measurement setups were designed, extensively validated, and practically used: one measurement setup was designed for emission investigations on a brake dynamometer under laboratory conditions and the other one was adjusted for on-road investigations on a vehicle. For both measurement setups, the same measurement concept was used that yielded the aspiration of the entire airborne brake wear. The brake wear was routed as whole to the measuring point, where it was analyzed with high time resolution by means of different devices with regard to the particle size and mass. In parallel, the air flow inside the setup was monitored, which allowed emission quantification. An estimation of the emission factors provided a good comparability of the results. The measurements were primary performed with realistic drive cycles so that the results were considered as representative for normal driving.

The emission factors of the left front brake of a midsize passenger car were found to be about 4.5 mg km^{-1} $brake^{-1}$ and 1-9$\times 10^{10}$ km^{-1} $brake^{-1}$ for particle mass (PM_{10}) and particle number, respectively. In addition, the emission behavior of the brake under elevated brake temperatures was investigated, which mainly favors ultrafine particle formation. For normal driving, however, the on-road measurements revealed much lower brake temperatures such that ultrafine particles are not expected to be formed. Furthermore, the origin of emissions during acceleration and constant driving phases was determined.

Publications

The thesis comprises (*partially) the following publications:

Paper I* M. Mathissen, J. Grochowicz, C. Schmidt, R. Vogt, F. H. Farwick zum Hagen, T. Grabiec, H. Steven, and T. Grigoratos. *A novel real-world braking cycle for studying brake wear particle emissions.* Wear, 414-415, pp. 219-226, 2018.

Paper II F. H. Farwick zum Hagen, M. Mathissen, T. Grabiec, T. Hennicke, M. Rettig, J. Grochowicz, R. Vogt, and T. Benter. *Study of brake wear particle emissions: Impact of braking and cruising conditions.* Environmental Science and Technology, 53, 9, pp. 5143-5150, 2019.

Paper III F. H. Farwick zum Hagen, M. Mathissen, T. Grabiec, T. Hennicke, M. Rettig, J. Grochowicz, R. Vogt, and T. Benter. *On-road vehicle measurements of brake wear particle emissions.* Atmospheric Environment, 217, 2019.

Contents

List of Figures

List of Tables

Frequently Used Abbreviations and Symbols

APS	TSI aerodynamic particle sizer
c	gas mixing ratio or particle concentration
CFD	computational fluid dynamics
$\mathrm{d_p/d_{tube}}$	particle/tube diameter
DT	TSI Dusttrak
$\Delta E_{\mathrm{rot/kin}}$	dissipated rotational/kinetic energy upon braking
$\Delta m_{\mathrm{filter}}$	raw filter load
EEPS	TSI engine exhaust particle sizer
EF	emission factor
ELPI+	Dekati electrical low pressure impactor
$\eta_{\mathrm{asp/trans}}$	aspiration/transport efficiency
LACT	Los Angeles city traffic
LM	low-metallic (content brake pads)
$\bar{M}_{\mathrm{res}}$	residual torque of the brake system
μ_{f}	coefficient of friction
NAO	non-asbestos organic (content brake pads)
PM	particulate matter
$\mathrm{PM_{10/2.5}}$	particulate matter with diameter of 10 µm/2.5 µm or less
$Q_{\mathrm{setup/device}}$	air flow in setup tube/measurement device
$q_{\mathrm{NO/NO_x}}$	$\mathrm{NO/NO_x}$ gas flow
SM	semi-metallic (content brake pads)
$\bar{T}_{\mathrm{crit}}$	critical brake temperature at which ultrafine particle emission occurs
T_{i}	initial brake temperature
TC	thermocouple
TSP	total suspended particles
$\mathrm{U/U_0}$	air velocity in sampling tube/setup tube
WLTP	worldwide harmonized light-duty vehicles test procedure

CHAPTER 1

Introduction

Environmental awareness is becoming increasingly important in our society. An essential aspect here is the maintenance of atmospheric air quality through reduced pollutant emissions. Heavy air pollution affects ecosystems and leads to climate change, which mainly causes a global increase in temperature [1, 2]. But also serious health concerns are associated with polluted air. The director of the World Health Organization (WHO), Tedros Adhanom Ghebreyesus, identified air pollution as "one of the biggest threats to global health" and called on the world community to take action against it [3]. Reducing emissions is in everyone's interests and it will become one of the biggest challenges of the current century.

The ambient air quality varies geographically and it depends strongly on the pollutants present and the concentrations at which they occur. The most harmful substances that are linked to public health concerns are gases such as ozone (O_3), nitrogen dioxide (NO_2), and sulphur dioxide (SO_2) [4]. But also particulate matter (PM) is classified as harmful as it shows the most severe indications of public health [5]. The term PM includes all suspended substances either of solid or liquid phase. The particles are of different size covering a wide range from nanometer up to several micrometers in scale. Depending on the particle size, different classifications are made based on the aspiration and/or absorption by the human body. For example, PM_{10} describes the mass fraction of all particles with diameters smaller than or equal to 10 µm. At an aerodynamic diameter of 10 µm the cut-off efficiency is at 50 %. Since the particles pass the larynx, the fraction is called "thoracic frac-

tion" [6]. Similarly the "respirable fraction" is defined by $PM_{2.5}$ with a 50 % cut-off efficiency at 2.5 µm particle diameter. Particles smaller than 1 µm behave similar to gas molecules and they are expected to penetrate down to the alveoli. They can be integrated into cells and/or the circulation system, which may cause the heaviest damage [7, 5].

As a consequence of particulate air pollution and the exposure to it, various diseases are known. In particular, respiratory and cardiovascular health effects are reported [8, 9]. For long-term exposure, the diseases are accompanied by losses of lung functionality, stroke, or an increased risk of suffering cancer [10, 11]. Thus in general, the exposure to PM emissions leads to an increased mortality and a reduction of human life [9]. About 400,000 annual premature deaths that are linked to PM immissions are reported for the European region [12]. As protective measure, the European Union introduced PM_{10} air quality standards in 2005. The legislation foresees an annual mean limit of 40 µg/m^3. This includes 35 permitted exceedances of 50 µg/m^3 based on a daily average. From 2015 on, additionally a $PM_{2.5}$ exposure limit of 20 µg/m^3 is valid, which is based on a three year average value [13]. In contrast, the WHO recommends more restrictive annual limits of 20 µg/m^3 and 10 µg/m^3 for PM_{10} and $PM_{2.5}$, respectively [14].

Particulate air pollution arises through natural phenomena and anthropogenic processes. Natural emissions, for example, occur as sea spray from the oceans and smoke from forest fires or volcanic eruption. Most of these emissions are linked to unpredictable events, whereas the anthropogenic emissions, which arise mainly from combustion and agriculture, pollute nature much more continuously. This allows a precise source apportionment classification. In figure 1.1 the anthropogenic PM_{10} and $PM_{2.5}$ sources and their shares are shown for the European Union. The biggest emission share is reported for the group of "Commercial, institutional, and households", followed by "Industrial processes" and "Agriculture". A significant share of about 10 to 11 % is also reported for the category "Road transport". In case of PM_{10}, this group represented a total contribution of nearly 300 kt over the year 2016 [15]. This includes exhaust as well as non-exhaust emissions that is road abrasion, tire wear and the focus of the present study, *brake wear*. Note, particle resuspension is not considered, which leads to the assumption of even higher PM_{10} emissions related to road transport.

When considering the German road transport related emissions, a very clear

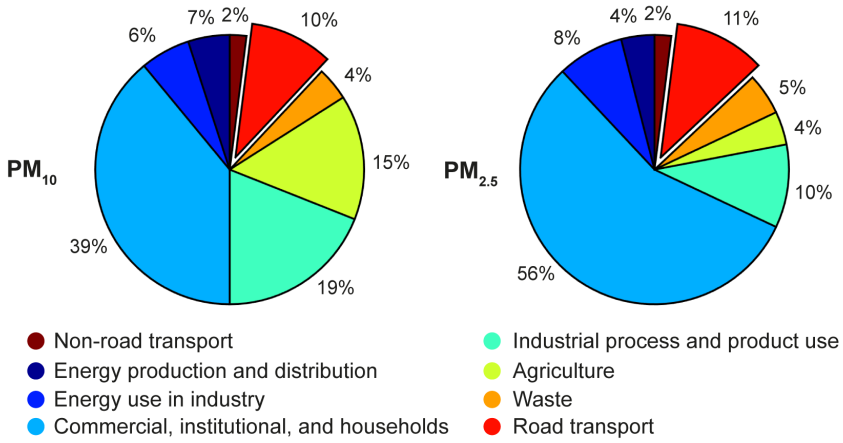

Figure 1.1 – Anthropogenic PM emissions in the European Union. PM_{10} (left) and $PM_{2.5}$ (right) emissions categorized by European Environment Agency (EEA) sector names in 2016. Based on data from EEA [15].

tendency can be seen that is in principle also representative for the EU. In figure 1.2 the annual PM_{10} emissions are plotted since the beginning of the century. Over the whole time series, the exhaust emissions were continuously falling. A reduction of more than 66 % was found for Germany. The reduction is attributed to the integration of novel exhaust filter technologies and aftertreatment systems into the vehicles as a consequence of policy regulations. Due to the continuous renewal of the vehicle fleet, a further reduction of exhaust emissions can be expected in the future (see figure 1.2 (b)). In contrast, the non-exhaust emissions remained unchanged. As the TREMOD model predicts, even an increase of non-exhaust emissions - especially for brake and tire wear - is expected. This emission trend can be explained by the fact that an increasing demand for mobility in combination with a growing fleet of vehicles is expected. Furthermore, non-exhaust emissions are not yet affected by regulations. Thus, a decreasing emission tendency cannot be expected in the near future.

As the diagrams (a) and (b) in figure 1.2 indicate, in the past, non-exhaust emissions were only roughly differentiated. The amount of brake wear on the traffic related PM or even the entire ambient PM remained unknown and is still highly uncertain [16]. Only a few studies addressed this issue and reported a brake wear fraction of 21 % to 55 % to the traffic related PM_{10} emissions [17, 18]. Measured by the ambient PM_{10} concentrations, brake wear emissions reflect smaller contribution

of only 5-10 % [19, 20]. Its absolute concentrations values were estimated and found to be in the range of 0.8 µg/m^3 to 4 µg/m^3. These estimations account for urban, traffic oriented areas, while for remote areas lower values are expected [16]. The observations are in agreement with the annual mean PM_{10} concentrations reported by the German Environmental Agency (see figure 1.2 (c)). Higher air pollution rates are also reported for the urban and especially the traffic-oriented areas. Since a large part of the population lives in urban areas, emissions should fall just there. Reducing further traffic related emissions may be one part of the solution.

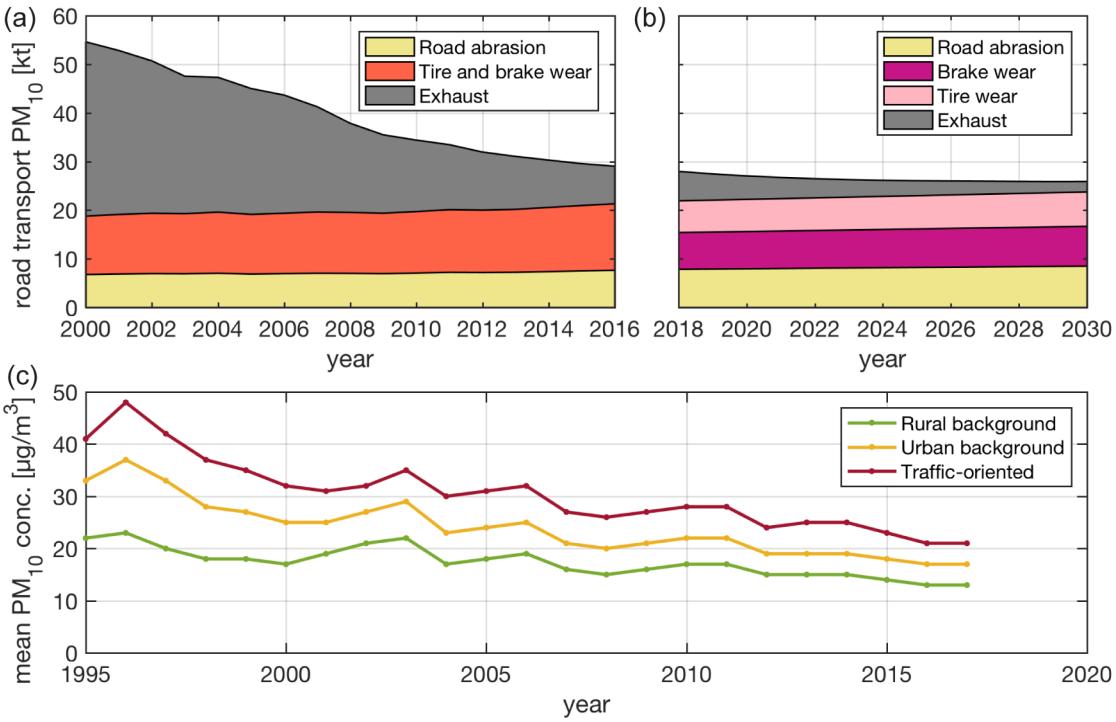

Figure 1.2 – PM_{10} in Germany. (a) Emission trend in the category "Road transport" from 2000 to 2016 [15]. (b) Expected emissions until 2030 using TREMOD-model. Data from the German Environment Agency [personal communication with J. Appelhans, 04-June-2019] (c) Mean annual PM_{10} concentrations categorized according to different measurement points. Data from the German Environment Agency [21].

The actual data of the German PM_{10} emission trend show a nearly equal share of brake wear and exhaust emissions. This ratio is actually not reached for all European countries and exhaust emissions are still predominating. However, the European Commission already established research programs that addressed the reduction of

brake wear emissions. One of the EU-funded projects was "LOWBRASYS" (Low Environmental Impact Brake System). The project aimed at the reduction of PM_{10} and particle number emissions of a conventional brake system by at least 50 %, respectively [22]. In order to achieve the goal, new brake materials, designs, and technologies for dust reduction were developed. This required a robust measuring procedure that allows to compare the emissions behavior of different brake materials and technologies. But a consistent and robust measurement method for brake wear emissions was not established. Even today there is no consensus on how to measure brake wear in a consistent and uniform way. Thus, this topic is under discussion within the framework of the UNECE-GREPE-PM program finding a standardized methodology for measuring brake wear [23].

Within the scope of the LOWBRASYS project, the present work was prepared. It proposes two solutions for measuring brake wear particles: one approach was performed on a brake dynamometer under laboratory conditions and the other one allowed brake wear investigations on a test vehicle under on-road driving conditions. For both approaches novel measurement concepts were developed. Particular attention was paid to emission investigation under realistic driving conditions, which clearly differentiated the work from previous emissions studies [24, 25, 26]. The setups were designed for highly sensitive measurements with low particles losses. A collective sampling of the entire brake dust through an enclosure around the brake enabled an emission quantification. As a result, emission factors (EF) in terms of particle number and particle mass were calculated. The laboratory investigations were verified through the on-road vehicle measurements, which completed the study. In general, both measurement approaches set novel aspects regarding brake wear investigation, which may serve as orientation for establishing standardized test methodologies in the near future.

CHAPTER 2

Aerosols, Brakes, and Brake Wear Particles

This chapter gives a brief insight into aerosol physics and describes methods for particle sampling. Furthermore, an introduction into common vehicle brake systems and their functionality is given. The particle generation process of friction brakes is discussed in a last section together with a review on brake wear measurement techniques and emission factors. All these topics are complex and cannot be covered in full detail. The chapter gives rather an overview of fundamental aspects that are related to the present work.

2.1 Aerosol Physics

2.1.1 Particles in the Atmosphere

An aerosol is described by Willeke and Baron as "an assembly of liquid or solid particles suspended in a gaseous medium (e.g., air) long enough to enable observation and measurement" [27]. The broad interpretation of the term aerosol already indicates the complexity of this topic, which refers to the different physical and chemical properties: aerosol particles cannot just be of different states of matter or be composed out of different elements, they are also of different size. The particle size is conventionally given in diameters (d_p) and an important quantity for describing aerosols. The influence of external forces and related interaction of the particles depend largely on the particle size. This establishes high dynamics within aerosols

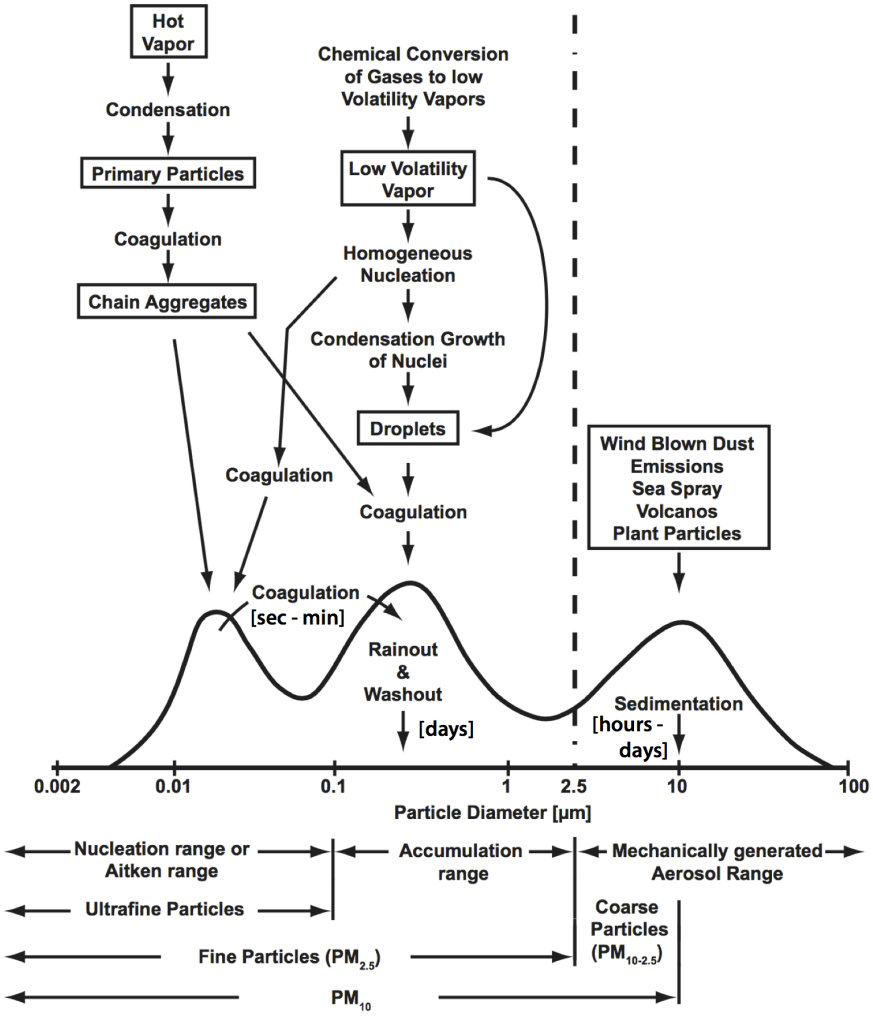

Figure 2.1 – **Typical aerosol modes**, their sources, sinks, and lifetime. Adapted from Baltensperger et al. [28] and Mathissen. [29].

leading to temporal changes of particle properties (i.e., size distribution, elemental composition, or electrical charge).

The atmospheric aerosols are differentiated according their sources in naturally and anthropogenic aerosols. While the former group includes aerosols such as sea spray from the oceans, mineral dust from dry regions, and smoke from volcanoes, the latter sources are dominated by agricultural and industrial emissions mainly resulting from combustion [28]. There is a further classification whether aerosols are directly emitted into the atmosphere, known as primary aerosols, or if they emerge from gaseous precursors (e.g., NO_x, SO_2, C_nH_{2n+2}) as secondary aerosols [28]. The

latter aerosol generation is also called gas-to-particle conversion and particles can either be formed from homogeneous or heterogeneous nucleation. In the former process, new nuclei are formed by self-nucleation from supersaturated vapor in the absence of impurities [28]. The heterogeneous process is based on particle growths on existing nuclei in less vapor saturated environments [30]. As already indicated, the dynamic processes of aerosols are versatile and a good overview is given by figure 2.1, which schematically shows the common sources, transformation processes and sinks of atmospheric aerosols. Furthermore, it contains the natural size distributions and the corresponding lifetimes [28, 31].

2.1.2 Aerosol Measurement

Aerosols are often analyzed by drawing partial aerosol samples, which are routed through appropriate tubing to the measurement devices, where the particles are detected. Although the concept seems to be rather simple, in practice certain aspects need to be considered that ensure a representative, unbiased aerosol measurement. In the following, two aspects, namely isokinetic sampling and particle loss mechanisms in sampling lines, are briefly introduced as they are of relevance for the present work. The used measurement devices are introduced in a last paragraph.

Isokinetic sampling. When aerosols are sampled in air streams of a certain air velocity (U_0) the probes are oriented in such way that the orifices are facing the incoming air flow. Once the probes are axially aligned with the air flow one refers to it as isoaxial sampling. In the case of isokinetic sampling, also the air velocity U_0 is equal to the air velocity inside the sampling tube (U). A combination of isoaxial and isokinetic sampling minimizes particle losses and reflects most representative measurement conditions. But due to varying U_0 of the ambient air, isokinetic sampling is often difficult to maintain. Three different flow conditions are distinguished:

1. Isokinetic sampling: $U = U_0$
2. Super-isokinetic sampling: $U > U_0$; PM is underestimated
3. Sub-isokinetic sampling: $U < U_0$; PM is overestimated

The different air velocity ratios between ambient air and the air inside the sampling tube influences the aspiration of larger sized particles. Due to the greater inertia of

these particles, they cannot follow the rapid change of the air flow direction near the probe as it is sketched in figure 2.2. For super-isokinetic sampling, the particles on the outer streamlines pass by the probe and the collected particle mass becomes underestimated. In case of sub-isokinetic sampling, it is vice versa and the results are overestimated. These effects can be described by empirical models, where the aspiration efficiency (η_{asp}) is a measure of how well aerosols are sampled.

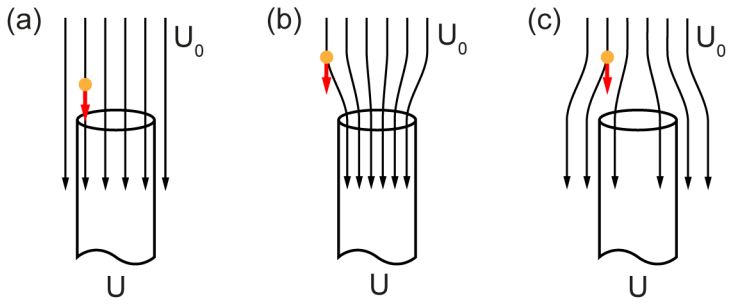

Figure 2.2 – Air flow pattern near probe for (a) isokinetic ($U = U_0$), (b) super-isokinetic ($U > U_0$), and (c) sub-isokinetic sampling ($U < U_0$). Adapted from Mathissen [29].

Particle losses in sampling lines. The aerosol samples need to be routed in sampling lines to the measurement devices before they can be analyzed. The aerosol transport leads to particle losses, which depend in particular on the air flow, sampling line geometry, temperature gradients, and the particle size [27]. In order to minimize particle losses, it is important to take into account the different loss mechanisms during the design phase of the setup. The underlying models give an estimation on the transport efficiency (η_{trans}) that can be used for setup evaluation.

One prominent effect is gravitational settling, which is the particle deposition attributed to gravitational forces in non-vertical sampling line sections [27]. This mechanism effects mainly particles of larger diameter and related losses can be reduced by increasing the air flow inside the sampling line, by decreasing the sampling line diameter or the length of horizontal sampling lines. Larger particles are also expected to be lost by inertial deposition. This effect comprises all losses based on particle impaction caused by either turbulent air flow or changes in the sampling line geometry. For example, inertial deposition occurs at tight bends or discontinuous junctions and thus losses can be minimized through bends with small curva-

ture, sampling lines with larger diameter, and a reduced sample flow. Smaller sized particles are not affected by these loss mechanisms as they are of a more gaseous character. These particles are more susceptible for diffusional deposition. Here the particles diffuse as a result of Brownian motion to the sampling line walls, where they become deposited. With increasing setup flow this effect can be avoided [27]. Furthermore, electric fields or temperature gradients cause particle deposition that is also known as electrostatic or thermophoretic deposition, receptively. While the former effect can be avoided by using conductive and grounded sampling lines, the latter effect might be obviated by placing all setup components in the same environment at a constant temperature. However, compared to gravitational settling or inertial deposition these effects are believed to be of minor relevance.

Measurement devices. The measurement devices used in this work are listed in table 2.1 together with an excerpt of their specifications: there were two devices used for particle mass measurements, namely the Dekati PM_{10} impactor and the TSI Dusttrak. Both devices collect the particle mass through filtering or impaction. Furthermore, the Dusttrak determines the particle mass concentration in continuous measurements over the whole measurement duration by light scattering.

For the particle number determination several other devices were used: the TSI optical particle sizer (OPS) and the TSI aerodynamic particle sizer (APS) analyze mainly fine and coarse particles. Their principle is based on either light scattering or time of flight analysis of particles [32]. The latter mechanism, which is used by the APS, allows very precise particle size classification. Following a different approach, the TSI engine exhaust particle sizer (EEPS) conducts an electromobility classification. This enables the observation of even smaller particles in a size range of 5.6-560 nm. Next to its high particle size resolution it has also a high sampling rate. A broader size range is covered by the Dekati electrical low pressure impactor (ELPI+). The device combines two detection mechanisms, namely the mechanical impaction and electrostatic discharge. Since it contains only 14 impactor stages, its resolution regarding particle size is rather rough.

In summary, the used devices cover a size range from about 5 nm to 20 µm and certain ranges were analyzed twice. Due to different measurement techniques applied a meaningful verification of the results was given.

Table 2.1 – **Particle measurement devices** that were used within the present work.

Device	Mechanism	Size range	Properties
Dekati PM_{10} Impactor [33]	gravimetric: impaction/ filtration	full	collection range: PM_{TSP-10}, $PM_{10-2.5}$, $PM_{2.5-1}$, and PM_1 (filter)
TSI Dusttrak 8533 [34]	optical: light scattering/ filtration	0.1-10 µm (impactor)	cal. with A1 dust; concentration range: 0.001 bis 400 mg/m^3; sampling rate: 1 Hz
TSI APS 3321 [32]	optical: time of flight/ light scattering	0.5-20 µm	classification into 52 size bins; sampling rate: 1 Hz; resolution: 0.02 µm at 1.0 µm
TSI OPS 3330 [35]	optical: light scattering	0.3-10 µm	classification into 16 size bins; sampling rate: 1 Hz
TSI EEPS 3090 [36, 37]	electromobility classification	5.6-560 nm	classification into 32 size bins; sampling rate: 10 Hz
Dekati ELPI+ [38, 39]	impaction/ electrostatic discharge	6 nm - 10 µm	classification into 14 size bins; sampling rate: 10 Hz

2.2 Vehicle Brake Systems

According to Breuer and Bill [40], vehicle brake systems have three fundamental functionalities: brake systems reduce the vehicle velocity, they are used in case of unintentional accelerations (e.g., down-hill driving), and they prevent vehicle movement at stand still (e.g., parking). Brake systems substantially ensure the safety of vehicle occupants and other traffic users. Therefore, they are classified as safety relevant units, which must meet strong regulatory requirements. The demands on brake systems are high and mainly related to functionality and robustness under various environmental conditions, fail-safety, and NVH issues (noise, vibration, harshness) [40]. At the same time, the components should be kept simple, easy to maintain, and to be able to manufacture at low costs. Thus, from the technical point of view, brake systems are rather complex.

Brake systems can be based on different technologies. In conventional vehicles the brake system is based on friction brakes. In hybrid or electric vehicles, friction brakes are supported by braking energy recuperation systems. In the present study, a hydraulic friction brake was used and its principle is described in the following. The brake is triggered by the driver through the brake pedal. The pedal is connected to the brake booster, which amplifies the signal and generates hydraulic pressure

[41]. The brake pressure is routed through brake hoses to the foundation brakes, the main components of the brake system. At the brake, friction materials are pressed against each other as a result of the applied brake pressure. Thereby, the kinetic energy of the vehicle is transformed into thermal energy. The resulting brake torque is acting on the wheel and transmitted to road, so that the vehicle is slowed down. The brake force of the vehicle is proportional to the brake pressure of the brake system [40]. Note, this description is reduced to the fundamental components of a brake system and there are a lot more components needed within a full system - especially when brake assistant systems are integrated, as for example ABS (anti-lock braking system) or ESC (electronic stability control). However, their description is beyond the scope of the present thesis and the inquiring reader is referred to Breuer and Bill's *Bremsenhandbuch* for more information [40].

There are two types of friction brakes on the market, namely drum and disc brakes. Drum brakes are composed of brake shoes that are connected to the vehicle knuckle and a drum that is attached to the rotating vehicle axis. During braking, the brake piston presses the brake shoe in radial direction against the friction surface at the inside of the drum and the rotating axis is slowed down. Due to the enclosed design, on the one hand, drum brakes are very resistant to environmental influences. On the other hand, the brake cooling is low, which leads to divergent brake characteristics. Furthermore, the mechanism tends to self-lock or the opposite [41]. As consequence, the brake behavior is of poor linearity and may lead to unpleasant brake feeling. However, drum brakes are most commonly used and can be preferably found in buses, trucks or at the rear axis of passenger cars. There is also high interest in drum brakes for electric or hybrid vehicles because of low corrosion impact, high brake life time and low dragging torque.

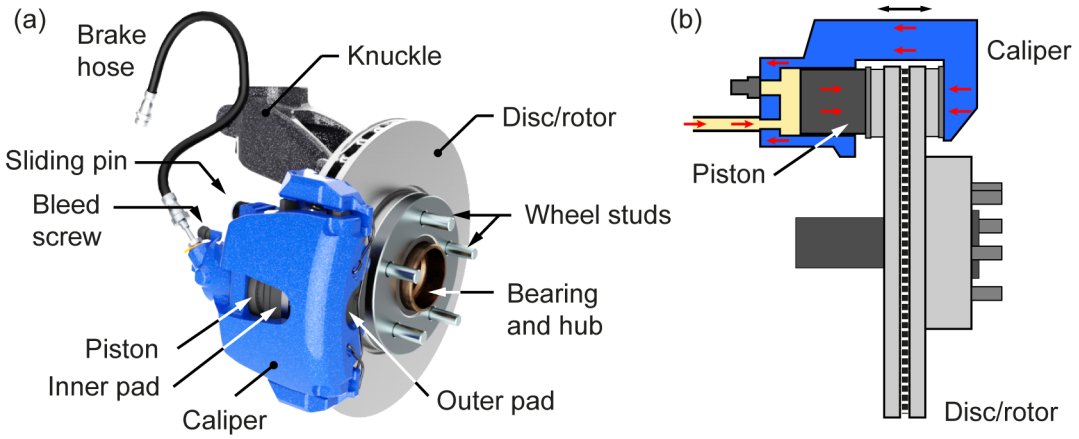

Figure 2.3 – **Disc brake** with floating caliper of the left front wheel. (a) Virtual image with labeling and (b) sketch with acting forces during braking indicated by red arrows.

For passenger and light duty vehicles the disc brake is also widely used. The disc brake is composed out of a rotating rotor that is connected to the vehicle axis and a brake caliper, which is the stationary component attached to the vehicle knuckle. The design of brake calipers varies: there are fixed calipers with pistons on each side of the brake disc, which are usually found in high performance cars, and there are floating calipers that get along with a single piston on vehicle side. Figure 2.3 shows the design and concept of a floating disc brake, which was also used for the present study. In contrast to drum brakes, the brake piston is acting in axial direction. In case of braking, the piston presses the inner brake pad against the rotor. Due to the floating design, the caliper slides along the sliding pins in the opposite direction and presses the outer pad against the outer surface of the brake rotor (see figure 2.3 (b)). Thereby a uniform wear between outer and inner pad is guaranteed and the brake dimension is kept compact. When the brake pressure is released, the piston is retracted mechanically away from the friction surface by the deformation of the sealing ring at the caliper. The piston comes back to the initial shape (roll back). Additionally, the brake pads are pushed apart by run-out of the brake rotor during acceleration of the vehicle. Thereby, the pads remain at a minimum distance to the brake disc (clearance), which ensures a fast reaction time when the brake is used again. Due to the exposed and mostly ventilated brake rotors, disc brakes are cooled down well and thus are suitable for high power consumption. The small reaction times of the brake and the nearly linear brake characteristic create a comfortable

driving experience.

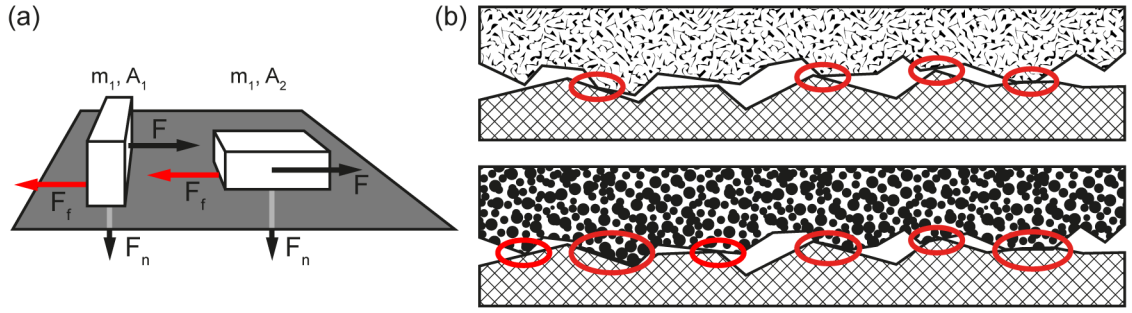

Figure 2.4 – Friction. (a) A block is dragged over a horizontal surface. The acting forces are sketched by arrows. The friction force F_f is highlighted in red. (b) Sketch of the microscopic contact interface of two materials. In the upper material either the contact pressure is lower or the material is harder. The contact areas are encircled. Adopted from Eriksson [41].

The braking performance of friction brakes is decisively determined by the material composition of the friction material, i.e., the pad lining and the rotor. The coefficient of friction (μ_f) is a measure of the friction behavior between the materials and an important quantity for material ranking. In order to understand μ_f and its dependencies, one can imagine the following experiment: a block with mass (m_1) is dragged over a horizontal plane, as it is shown in figure 2.4 (a). The contact area between the two materials is defined by A_1, the normal force by F_n, and the required drag force by F. The resulting friction force (F_f) acts in the opposite direction of F. The coefficient of friction is defined as the proportionality between F_n and F_f [41, 42]:

$$F_\mathrm{f} = \mu_\mathrm{f} F_\mathrm{n}. \tag{2.1}$$

When the same block is placed on a different side with area A_2, still the same drag force is needed for movement. Although the macroscopic contact area between the two materials has been changed, the microscopic area remains the same. Thus, the friction efficiency is only determined by μ_f and independent of the macroscopic contact area. The microscopic contact area between two materials can be changed by either increasing the contact pressure (*here:* brake pressure) or by using materials

of different hardness [41, 43]. The two cases are schematically shown in figure 2.4 (b), where in the second diagram either a higher pressure or a softer material is used.

Table 2.2 – Material composition of brake pads. Based on the ref. [44, 45, 46, 47].

Group	Proportion	Function	Materials
Reinforcing fibers	6-35 %	provide mechanical strength/ form contact plateaus	metallic, mineral, ceramic, organic (eg., copper, brass, glass)
Binders	20-40 %	preserve structural integrity under mechanical and thermal stress	modified phenol-formaldehyde resins
Fillers	15-70 %	improve manufacturability and heat resistance/ reduce brake noise properties/ cost reduction	mostly inorganic compounds (eg., barium and antimony sulfate, stone, metal powders)
Lubricants	5-29 %	stabilize μ_f during braking	inorganic, organic, metallic (eg., graphite, metal sulphides, cashew dust)
Abrasives	up to 9 %	increase friction/ maintain cleanliness of friction interface	hard metal oxides, silicates (eg., zirconium oxide)

Brake pads consists out of a back-plate, a shim, and the friction lining. The iron back-plate is the solid base of the pad, it keeps the position within the caliper and it distributes the piston pressure equally to the friction lining. On piston side, the shim is mounted, which is a composition of organic materials on a thin metal plate. It is mainly used for thermal insulation and noise reduction [48]. On the rotor side of the back-plate, the friction lining is deposited, which is a composition of up to 30 materials [49]. The detailed composition of the lining material is part of the manufacturing secret and therefore not known. However, a classification of the materials is often found according to functional groups, namely fibers, binders, fillers, lubricants and abrasives [45, 46, 47]. The material groups and its functionalities are listed in table 2.2. Through different material mixtures, the desired brake, noise, and wear behavior of the brake is tuned. Depending on the use case and local regulations, industry differentiates between three types of material compositions: non-asbestos organic (NAO), low-metallic (LM), and semi-metallic (SM) content brake pads [47, 48]. NAO pads are common for the US and Asian market, they stand out through low noise levels and wear rates. The coefficient of

friction ranges between 0.3-0.4 and is thus comparatively low - especially at high temperatures [50, 51]. In the past, these pads contained Asbestos, which was later banned due to serious health concerns [52, 53, 54, 55]. Nowadays these pads contain copper and Cu-alloys of up to 10 % but the legislation require to reduce the copper content to less than 5 % by 2021 and to less than 0.5 % by 2023. LM content brake pads are most common in Europe. They have high μ_f values in the range of 0.35-0.5, are stable at high vehicle velocities and brake temperatures but show higher wear rates [50]. The proportion of metallic components is in the range of 10-30 %. SM pads have the highest amount of metal content of 30-65 % [56]. They have a high durability and an excellent heat transfer, thus an overheating of the friction surface is prevented. Their disadvantage is the higher disc wear. These pads are meant to be used under extreme braking conditions in either sport or police cars.

The rotor material used in most brakes is gray cast iron. It possesses high mechanical strength, thermal conductivity, and causes low production costs [48]. Besides gray cast iron rotors, there are novel materials on the market, as for example carbon-silicon carbide-composite or silicon carbide-reinforced aluminum. Although their weight and performance properties are much better than gray cast iron, their commercial impact is rather low because of high acquisition costs [40]. The friction material used within this study was also a gray cast iron rotor in combination with LM brake pads.

Finally, technical terms around the topic vehicle brakes are presented in table 2.3 according to Breuer and Bill [40]:

Table 2.3 – Technical terms around brake testing. Based on Breuer and Bill [40].

Term	Description
Clearance	A small gap between disc and pad lining is called *clearance*. It ensures a free rotation of the brake disc, and thus improves the fuel consumption of the car. On the other hand, it increases the reaction time of the brake system.
Fading	*Fading* describes the reduction of μ_f at high brake temperatures caused by degassing of the friction material. It can be compensated through higher brake pressure.
Hot spots	*Hot spots* are local, point-like modifications at the rotor surface due to microstructural material changes or deposited wear. They increase noise (judder).
Roll back	Name for the mechanism that describes the mechanical retraction of the piston by the sealing ring between caliper and piston after braking. The deformed sealing ring goes back to its inoperative state.
Running-in	*Running-in* describes the process until stable test conditions are reached (e.g., constant μ_f) when testing newly manufactured material. Mostly the rotors are coated with a protecting layer that is removed during this process.
Run-out	*Run-out* are geometric tolerances in axial direction at the outer rotor surface during rotation. They occur from manufacturing and bearing clearances.

2.3 Brake Wear Particles and Measurement Techniques: a Review

2.3.1 Brake Wear Generation

Friction brakes reduce the vehicle velocity by dissipating kinetic energy into thermal energy. However, not all of the kinetic energy is transferred into thermal energy. Part of it is spend on deformation and destruction of the friction material [47]. This causes wear, which is known as *brake wear*.

The brake wear is generated through a complex process at the friction interface between disc and pad [57]. The wear mechanism is based on the formation of a third body layer, which is an intermediate friction layer between first and second layer, i.e., pad and disc [58, 59]. The layer accommodates the speed difference, the contact load, and further influences the actual friction behavior. Although the third body layer is also called mechanically mixed layer, it is not just a composition of pad and disc material. The third body layer is rather composed out of amorphous carbonaceous products and oxidative wear fragments, such as Fe_2O_3, Fe_3O_4, Cu_2O, or $CuFe_2$ [60, 61]. Not only the material composition is different from the disc and pad but also its texture, which is often described as nanocrystalline microstructure

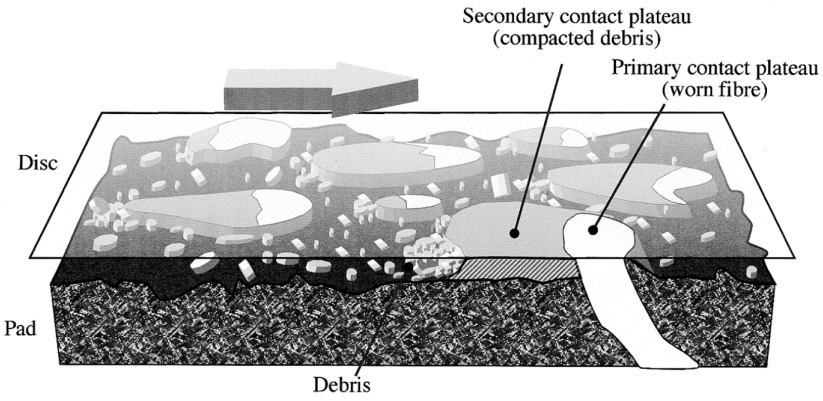

Figure 2.5 – Wear process at the friction interface. Fibers (light gray) touch the disc as primary contact plateaus and in front of them secondary plateaus are formed. The wear debris is pressed and sintered through the frictional energy. Reprinted with permission from Eriksson and Jacobson [65]. ©2000 Elsevier.

[62, 63, 64]. Eriksson and Jacobson [65] modeled the contact situation at microscopic scale and explained the wear process by means of figure 2.5. A transparent disc is sliding from left to right over the friction material. During friction, the soft pad material is continuously detached and the fibers protrude from its surrounding phenolic material matrix. As primary plateaus, the fibers touch the disc and generate ferrous debris. The worn debris of both materials accumulate in front of the plateaus, where it is compressed through the contact pressure and thus secondary plateaus are formed. Similar descriptions were made by Österle et al. [64], who used quartz crystals instead of metallic fibers as abrasives that raise to primary plateaus. They concluded that the continuous growth of the secondary plateaus and cracking of the underlying material lead to degradation of the plateaus and the release of debris from the friction surface [64, 66]. In addition to the mechanical wear process, thermal decomposition of the organic lining material may occur. Derived from theoretical models, it is reported that even at low friction velocities, flash temperatures of the order of 1500°C are expected at local asperities [67]. Thus, evaporation and local degradation of the pad lining material can be expected.

The mechanical wear process and the thermal decomposition of the pad material lead to wear generation of different sized particles [68]. As an example, Kukutschová et al. [69] measured particle number and particle mass size distributions in direct

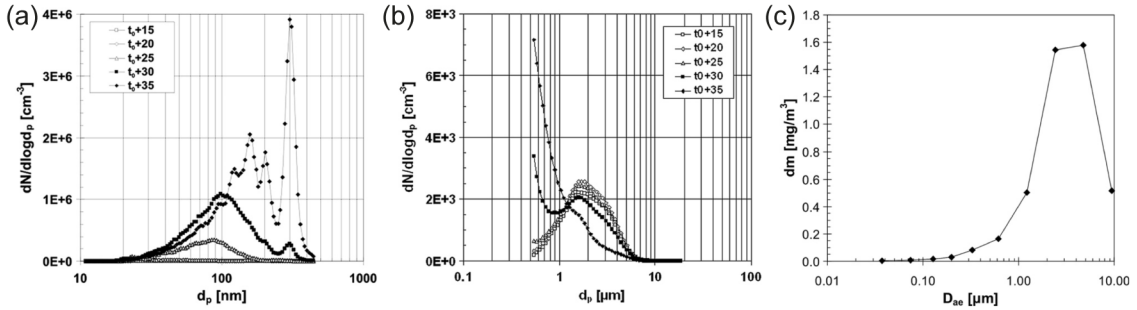

Figure 2.6 – **Particle size distributions** of airborne wear particles measured by (a) SMPS and (b) APS, where t_0+15,..t_0+35 represent time elapse from initiation of testing in minutes. (c) Particle mass distribution within the BLPI stages. Reprinted with permission from Kukutschová et al. [69]. ©2011 Elsevier.

vicinity of the brake on a dynamometer bench. Their results are shown in figure 2.6. In case of particle number, the distribution ranged from nanometers to tenth of micrometers with modal peaks at around 200 nm and 1.5 µm. In terms of particle mass, in contrast, a unimodal peak was found at around 2-4 µm. Obviously, the particle mass is dominated by bigger sized particles in the coarse ($PM_{10-2.5}$) and fine ($PM_{2.5-0.1}$) particle size range and the particle number distribution is accommodated over a wide, almost the full size range. This knowledge combined with the fact that particles settle or get lost during transport and sampling, challenge the way of proper brake wear particle measurements. There are a lot of studies on brake wear particles and how to measure them. Although their approaches differ widely and different priorities are in focus, they can be distinguished in measurements taking place in laboratory, on-road, and at ambient air with means of brake wear tracers. Within the framework of the UNECE-GRPE-PM program [23], brake wear is also under discussion and different methodologies are compared finding a standardized way for measuring. An overview of relevant studies is given in the following.

2.3.2 Measuring Techniques

Laboratory measurements. The majority of studies on brake wear particle measurements are performed in the laboratory. It is expected to be the most promising approach since it allows - by definition - investigations under confined test conditions. Test parameters, settings for vehicle simulation, and environment conditions can be easily constrained. Laboratory measurements are either performed with a

Table 2.4 – Brake wear emission measurements with pin-on-disc machines in chronological order. Modal peaks of particle mass and number size distributions are highlighted.

	Test specifications		Size distributions	
Reference	Material	Device	Particle mass	Particle number
Mosleh et al. 2004 [72]	SM	Light scattering analyzer	-	multimodal 0.35, 2, 15 µm
Olofsson et al. Wahlström et al. 2009/10 [73, 74]	LM, NAO	SMPS, OPC	-	multimodal 50-100, 280, 350, 550 nm 2 µm
Alemani et al. 2015 [75]	LM, NAO	FMPS, OPS	bimodal 0.025-0.1 µm 0.4-0.5, 10 µm	multimodal 11-34 nm 0.09, 0.19-0.29, 1.7 µm
Nosko et al. 2016/17 [76, 77]	LM, NAO	OPS, FMPS ELPI+, CPC	-	multimodal 4-10, 100-150 nm

pin-on-disc machine or on a brake dynamometer.

In a pin-on-disc machine a small pin drilled out of the brake pad is pressed on a rotating disc at constant pressure. The technique is mostly used when fundamental topics on friction behavior or wear characteristics are addressed [57, 70, 71]. Due to the simple setup it is also a good basis for modeling [49, 67]. The first particle measurements with a pin-on-disc machine were reported from Mosleh et al. [72], who used a light scattering analyzer. Later Olofsson et al. [73] and Wahlström et al. [74] gave further insight into the particle number size distributions on brake wear while using a scanning mobility particle sizer (SMPS) and an optical particle counter (OPC). Independent from the pad material, multimodal distributions were obtained in several investigations. Alemani et al. [75] built on the work and confirmed these findings while using a fast mobility particle sizer (FMPS) and an OPS. They calculated the corresponding particle mass size distributions and obtained a bimodal appearance. Nosko et al. [76] used additionally an electrical low pressure impactor (ELPI+) and a condensation particle counter (CPC). In focus of the investigation was the particle number size distribution on nanometer scale. Table 2.4 summarizes their main findings and it can be seen that there is agreement on the multimodal appearance of the particle number size distribution.

Table 2.5 – Brake wear emission measurements on brake dynamometers in chronological order. Certain test specifications are highlighted and modal peaks of particle mass and number size distributions are shown.

	Test specifications							Size distributions	
Reference	Chamber[a]	s. in duct[b]	Isokin. s.	Quantified[c]	Material	Brake cycle[d]	Device	Particle mass	Particle number
Cha et al. 1983 [78]					Asb.			unimod. 2-3.3 µm	-
Garg et al. [24] 2000	✓	✓		✓	LM NAO	✻	MOUDI ELPI	unimod. 1-10 µm	-
Sanders et al. 2002/03 [25, 79]		✓	✓	✓	all	✻ urban	MOUDI ELPI	unimod. 4-5 µm	unimod. 1 µm
von Uexküll et al. 2005 [80]					*unk.*	✻	OPC	unimod. 2-3 µm	unimod. 0.5-1 µm
Iijima et al. 2007/08 [81, 82]	✓				NAO	✻	APS	unimod. 2-6 µm	unimod. 0.8-2 µm
Riediker et al. 2008 [83]	✓				*unk.*	✻	SMPS	-	bimod. 27-83 nm 400 nm
Wahlström et al. 2009 [84, 85]	✓				LM NAO	✻	OPC DT PTrak	-	multimod. 280, 350 nm 1.8, 3 µm
Kukutschová et al. 2011 [69]	✓				LM	✻	SMPS BLPI APS	unimod. 2-4 µm	multimod. 0.1-0.3 µm 1.5 µm
Augsburg et al. 2011/12 [86, 87]					*unk.*	✻	SMPS CPC	-	unimod. 100-150 nm
Hagino et al. 2015/16 [88, 89]	✓	✓		✓	*unk.*	✻, JC08 JE05	ICP-MS DT	unimod. 0.7-3 µm	-
Perricone et al. 2015/16 [26, 90]	✓		✓	✓	LM NAO	✻, SAE J 2707	ELPI+ DT	unimod. 5-8 µm	bimod. 10 nm 0.5-2 µm
Farwick z. Hagen et al. 2017/19 [91, 92]	✓	✓	✓	✓	LM	LACT (3h) WLTP	ELPI+ DT, OPS EEPS	unimod. 2-4 µm	multimod. 10, ≈150 nm 2-3 µm
Augsburg et al. 2017 [93]	✓	✓	✓		LM NAO	NEDC WLTC	DMA	-	-
Gramstat et al. Lugovyy et al. 2017/18 [94, 95]	✓	✓			*unk.*	✻	SCPS EEPS ELPI	unimod. 1.5-2.5	bimod. 10-20 nm 150-200 nm
Agudelo et al. 2017 [96]	✓	✓	✓		LM NAO	div.	EEPS OPS	-	multimod. 10, 40 nm 80-200 nm
Plenne et al. 2018 [97]	✓	✓	✓		*unk.*	urban	DMS ELPI	-	bimod. 10, 250 nm

[a] Chamber with filtered inlet air, [b] sampling in full aerosol duct, [c] studies that reported quantified emissions in terms of emission factors, [d] real-world brake cycles; ✻ braking from set of speeds, transient/ full stop braking/ different artificial brake pattern

Compared to pin-on-disc machines, dynamometers reflect the reality much better since the brake is preserved as a full system and analyzed as it is mounted on the vehicle. The number of brake wear studies performed on dynamometers is large and the approaches are diverse (see table 2.5).

The first wear investigation was reported by Cha et al. in 1983, who studied asbestos brakes especially in view of health concerns. Later, when asbestos brake pads were already banned [98], Garg et al. [24] and Sanders et al. [25] published systematic approaches for brake wear measurements while using a multi orifice uniform deposition impactor (MOUDI) and an ELPI. Their works became groundbreaking since they used setup designs specialized for brake wear sampling. In their setups brake dust was routed at constant air flows through a ductwork, where it was sampled under defined conditions. While Garg et al. [24] enclosed the brake completely with a sealed chamber, Sanders et al. [25] used an open setup configuration. Furthermore, Sanders et al. paid attention to particle losses and conducted measurements under isokinetic sampling considerations. Later on, Iijima et al. [81], Riediker et al. [83], Wahlström [84], Kukutschová et al. [69, 99], and Augsburg et al. [87] performed brake wear measurements on dynamometers while using an enclosed chamber and different kinds of measurement devices (i.e., SPC, SMPS, APS, DT, Berner Low Pressure Impactor (BLPI)). Their approaches, however, were based on sampling in close vicinity to the brake, in fact it took place within the chamber. On one hand, this approach may be suitable for the analysis of particle size distributions and elemental compositions of the brake wear. On the other hand, this technique might not allow a proper emission quantification because particle concentrations may vary at different locations inside the chamber. Hence, the idea of sampling inside the ductwork was picked up again: Hagino et al. [88] adopted the setup concept similar to Garg et al. [24], where filtered air entered the brake chamber on one side and the brake dust was routed out of the chamber on the other side for measuring. Although it was not reported whether probes were sampled under isokinetic conditions, the principle enabled quantification as the air flow was kept constant and the particle background concentration was reduced due to filtering. Hagino et al. [89] focused on particles mass analysis and investigated elemental compositions with an inductivity coupled plasma-mass spectrometer (ICP-MS). Besides Sanders et al. [79], tests with realistic drive cycles were conducted for the first time. Until that time, drive cycles were artificially chosen and brake stops were performed from certain set of speeds

at constant decelerations. Around the same time, Periccone et al. [26] proposed another sampling setup that was optimized for low particle losses including isokinetic sampling. For efficient brake cooling, the measurements were performed at high air flows and instead of routing the full dust exhaust to the sampling point, a partial flow was used for sampling. Since the main exhaust was bypassed, the signal strength was reduced, which allowed potential improvements when sampling low concentrations. Periccone et al. [90] investigated particle size distributions with an ELPI+ and developed concepts for material ranking regarding wear characteristics. The applied drive cycles contained static brake pattern and were still artificial. But parameters like initial velocities and decelerations were inspired by real driving. In recent years, brake wear gained more and more attention and also train brakes were investigated [100, 101]. In total, the measurement setups have developed to more and more complex designs that nearly all considered an enclosed brake, low particle losses, and isokinetic sampling in the exhaust ductwork. However, the way of archiving these requirements is still varying and Augsburg et al. [93], Agudelo et al. [96], and Gramstat et al. [94] and Lugovyy et al. [95] are continuously developing their setups. According to the current state and the best knowledge, some distinctive setup features are listed in table 2.5.

The measurement setup that was developed for the present study also considered the requirements mentioned above. Further attention was paid on quantification of the measured emission data through a constant setup air flow. The air flow was set close to the conditions found at the vehicle and thus much lower than that of research colleagues [26, 94]. Although this led to weaker brake cooling, it increased the sampling sensitivity. A high signal sensitivity was required since drive cycles representative for real driving were performed and emissions were expected to be lower than during harsh braking maneuvers. Thus, the present setup was optimized for measuring emissions during normal driving simulations with the intention to determine realistic emission factors (EFs).

On-road vehicle measurements. Measuring brake wear particles on-road is much more challenging and thus, the number of reported studies is much lower compared to laboratory investigations. Sanders et al. [79] reported on-road measurements with a test car for the first time. In their approach, brake wear was sampled at different points: at the brake, the wheel, and within the wheel house.

Later on, Mathissen et al. [102], Kwak et al. [103, 104], and Wahlström and Olofsson [105] equipped test cars with measurement instrumentation and draw samples in close vicinity to the brake. Their sampling points were positioned directly behind the friction interface of the brake. Hence, they confirmed a correlation of obtained emissions with the corresponding brake events. In case of harsh brake events at high brake temperatures, also ultrafine particle emissions were reported. However, due to the partial sampling of brake dust, a quantification of emissions was not possible and EFs remained unclear.

For the present study a novel setup design was developed that addressed precisely this issue. The setup concept was inspired by dynamometer studies: it aims at monitoring the entire brake dust through a cone shaped collector at the outside of the wheel rim. From there the dust was transported as a whole to the sampling point in the trunk of the car, where particle samples were drawn and analyzed. The air flow inside the setup was driven by a blower independently from the measurement devices. The setup design was suitable for real-world EF determination and enabled direct comparisons to dynamometer studies.

Ambient air measurements and receptor modeling. As a final remark - although it is beyond the scope of the present thesis - it is mentioned that brake wear was also identified during ambient air measurement campaigns. Finding the contributors to traffic related particulate matter emissions, ambient air was analyzed in the surroundings of streets, traffic junctions, or tunnels [106, 107, 18]. Several studies used receptor modeling techniques for source apportionment as for example the chemical mass balance model. The advantage of these measurements over investigations directly at the source (i.e., the brake), is the emission record of the entire vehicle fleet and not only of a single type of brake. On the other hand, the techniques are based on precise knowledge of the source material compositions, which is often limited [56, 108]. Common key tracers related to brake wear are the elements Fe, Cu, Sb, Sn, Mo, Zn, Zr, and Ba [18, 109, 19, 17, 110]. Some studies also report the ratio of Copper to Antimony to be characteristic for brake wear generated particulate matter [68, 111, 112].

In conclusion, receptor modeling is a powerful technique for estimating the contribution of brake wear to the total traffic related particulate matter and the determination of EFs. For further information, the reader is referred to the review articles

on traffic related particulate matter emissions by Thorpe and Harrison [46], Pant and Harrison [113], and reports from Boulter et al. [56] and Grigoratos and Giorgio [108].

2.3.3 Size Distribution and Emission Factors

As already mentioned, the particle number distribution of brake wear shows different modal appearances. As summarized in the tables 2.4 and 2.5, the distributions vary and unimodal, bimodal, and multimodal peaks were reported. Unimodal peaks in the fine size range were obtained during the initial stage of brake wear measurements on dynamometers or during on-road measurements. Here only measurement devices for the coarse and fine particle size range were used [79, 114, 103]. But the appearance of ultrafine particles at high temperatures was recognized early [24] and the following dynamometer studies also included measurement devices capable for detecting smaller particles. Since then mostly bimodal and multimodal peaks were reported. Also on-road measurements that simulated harsh braking conditions at high temperatures reported additional modes in the ultrafine size range [102, 104]. In case of the pin-on-disc studies, only multimodal distributions were reported. Obviously, the particle number distributions have different modes, but there is no final agreement on whether these modes are bimodal or multimodal. In addition, the results are difficult to compare due to different devices, materials, or measurement conditions. In summary, there are modes reported to be in the fine size range related to abrasion. And the nucleation modes in the ultrafine size range were observed at high brake temperatures due to evaporating material.

Coarse and fine particles are formed as a result of the mechanical wear process. These particles dominate the particle mass distribution. The distributions are of unimodal appearance and most studies reported peaks in the range of 2-4 µm. Although some studies also obtained peaks at larger particle sizes and individual modes were obtained at smaller sizes, the reported findings can be considered as consistent.

When talking about particle mass distributions it is important to note, that these results refer to the airborne particles. But not all brake wear particles become airborne. In some studies an airborne fraction is reported, which describes the weight ratio of airborne particles to the mass loss of the brake material. Garg et al. [24] found 86 % and 63 % of airborne particle mass to be PM_{10} and $PM_{2.5}$, respectively.

From that about 33 % were found to be smaller than 0.1 µm. Sanders et al. [79] reported PM_{10} airborne fractions of about 63-85 % depending the tested brake lining. Additionally, Sanders et al. [25] increased the particle loss probability through tests with a fully mounted wheel. And still airborne fractions in the range of 50-70 % were found. Iijima et al. [82] measured directly underneath the brake and found even higher values: they reported 95-98 % and 56-70 % for PM_{10} and $PM_{2.5}$, respectively. Whereas Hagino et al. [89] reported smaller fractions of 9-22 % for PM_{10}. Apparently, the airborne fraction is influenced by the sampling position and the setup designs.

The reported EFs are typically ranging from 10-20 mg km^{-1} veh^{-1} and 50-80 mg km^{-1} veh^{-1} for light duty vehicles and heavy duty vehicles, respectively [56]. They can be distinguished by measurements taking place directly at the source or through ambient air monitoring with receptor modeling. The results obtained on the dynamometer differ greatly, which can be attributed to different brake materials and drive cycles. Garg et al. [24] found EFs in the range of 2.9-7.5 mg km^{-1} veh^{-1} . Sanders et al. [79] reported a range of 1.5-8.1 mg km^{-1} veh^{-1}, whereas NAO brake pads were found to be less emissive than LM content pads. Iijima et al. [82] obtained 5.8 mg km^{-1} veh^{-1} for NAO pads, which fits to previous observations. Perricone et al. [90] confirmed the observation of less emissive NAO pads but their absolute values were remarkably high: EFs of 13.7-35.2 mg $stop^{-1}$ $brake^{-1}$ and 9.2 mg $stop^{-1}$ $brake^{-1}$ were found for LM and NAO pads, respectively. Note, these values were reported for a single brake and need to be projected to vehicle EFs for proper comparison[1]. In contrast, Hagino et al. obtained just 0.04-1.4 mg km^{-1} veh^{-1} for presumably NAO material [89]. In case of reported EFs from receptor modeling, the values strongly depend on the measurement site. Rauterberg-Wulff [115] and Bukowiecki et al. [107] found small values of around 1-1.7 mg km^{-1} veh^{-1} near highways. EFs obtained in urban street canyons or at traffic junctions were higher and values of 6.9-10.7 mg km^{-1} veh^{-1} were reported [68, 107, 116]. Abu-Allaban et al. [106] even found different EFs from 0 to 80 mg km^{-1} veh^{-1} depending on the location.

In conclusion, the variation of reported particle mass EFs is large and is highly influenced by several factors. The reported EFs that were derived from direct mea-

[1]The brake power distribution between front and rear axis is about 70:30 and thus a factor of 3 is a reasonable choice for projection.

surements at the brake were mostly not reflecting realistic driving conditions. Furthermore, there is a lack of knowledge on particle number emission factors. Although there are individual studies that reported maximal values of the order of 7×10^{10} to $4.6\times10^{12}\,\mathrm{stop}^{-1}$ brake^{-1} (Garg et al. [24], Perricone et al. [90]), a verification on whether these values are representative for realistic driving remains unclear. The determination of EFs representative for real-world driving and a verification of these values through on-road measurements is the scope of the present thesis.

CHAPTER 3

Laboratory Measurements of Brake Wear Particles

3.1 Measurement Setup

3.1.1 Description

The laboratory measurements were performed on a Link 3900 brake dynamometer. The modern dynamometer enabled precise vehicle simulations through the adjustment of flywheel masses, software settings (e.g., recuperation and parasitic drag), and drive cycles. It was used in hard-fix configuration, meaning that the brake was mounted on a locally fixed vehicle knuckle. In contrast to the vehicle, the brake was accelerated through a drive shaft that was mounted at the outside of the brake, where usually the wheel rim is installed (see figure 2.3). Since the wheel was not mounted, this setup arrangement allowed an investigation of the isolated, nearly free-standing brake. Furthermore, the knuckle could be connected to a measuring flange that recorded inertia whenever forces were acting on the brake. The entire brake system, including knuckle, hard-fix, and drive shaft, was located inside an approximately 10 m^2-sized test room. The air conditioning of the test room provided prefiltered air and stable environmental conditions (50 % relative humidity, 30 °C temperature). Inside the test room, the entire particle measurement setup was installed as visualized in figure 3.1.

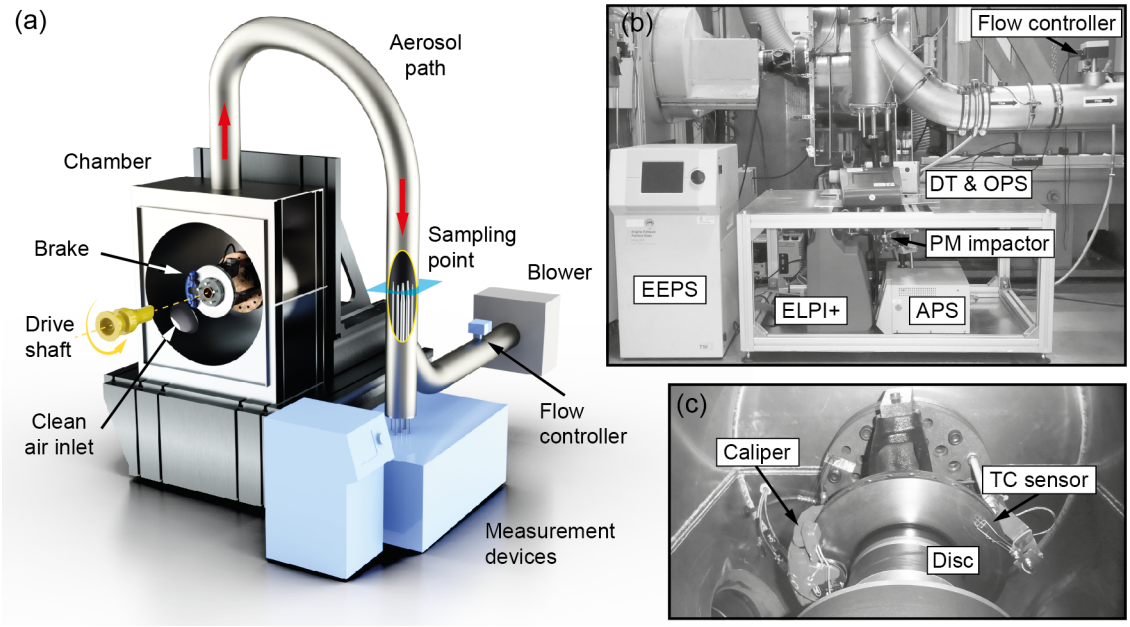

Figure 3.1 – Dynamometer setup. (a) Rendered image of the setup. The blue cut through at the sampling point shows the measurement plane of the air velocity profiles. (b) Picture of the particle measurement devices and the flow controller. (c) Picture of the chamber interior. Adapted with permission from Farwick zum Hagen et al. [92]. ©2019 American Chemical Society.

The measurement principle was based on a constant volume system, meaning that clean air was routed to the brake, where it mixed with the brake dust to an aerosol, and further routed to the sampling point. The air flow was kept constant at all times, independent of the braking maneuver. To realize these measurement considerations, the following basic setup components were needed: an enclosing chamber, where the brake was located inside, a tubing system, air filters, and a blower. The detailed arrangement of these components is schematically shown in figure 3.2.

As a starting point, the following assumption was made: the air flow through a wheel rim of a driving vehicle at 70 km/h was estimated to be ≈264 m^3/h by computational fluid dynamics (CFD) calculations. Using this value as orientation, a setup flow of Q_{setup} = 250 m^3/h was defined for testing. The blower at the end of the aerosol transport line created the desired air flow with a minor tolerance of ±10 m^3/h. The blower was feedback controlled by an air flow meter (Vortex ultrasonic sensor, Höntzsch VA40) that was installed directly in front of the blower in combination with a honeycomb flow straightener. The air flow meter was also

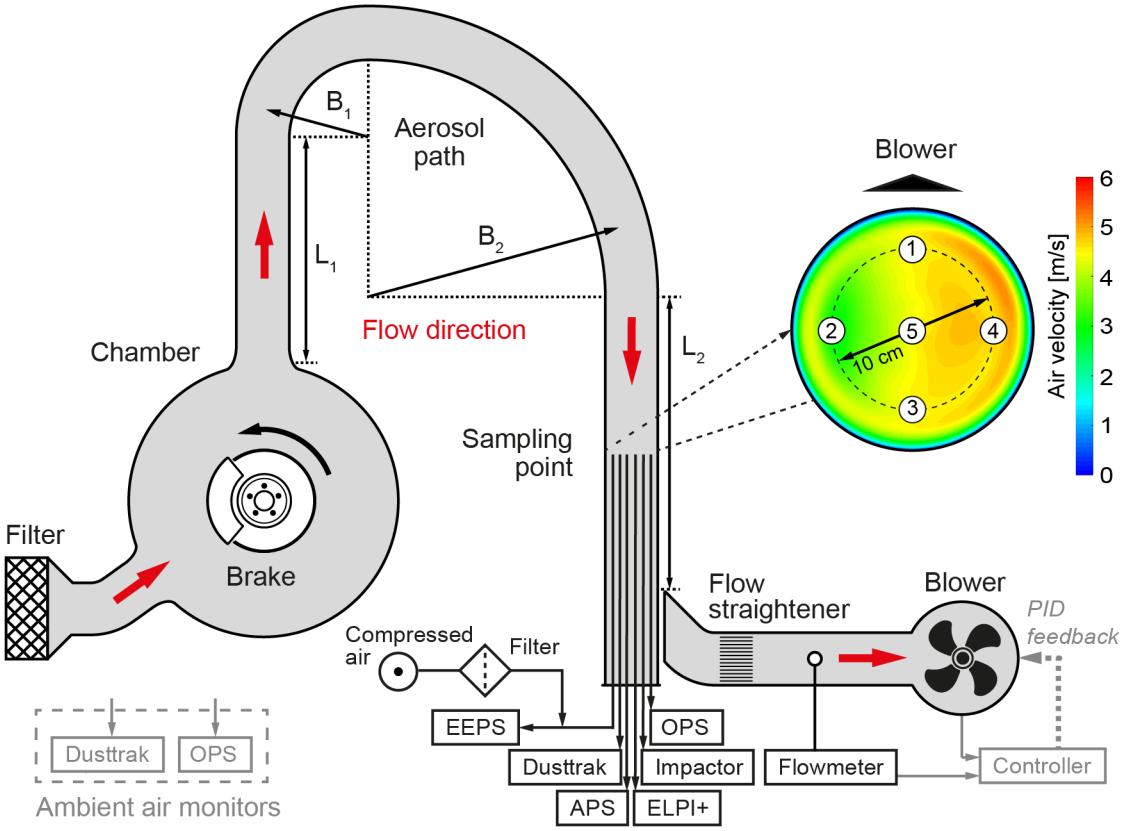

Figure 3.2 – Measurement principle of dynamometer setup. The chamber and tubing is colored in grey and the measurement devices and their tubing are sketched similarly to the experimental arrangement. The air flow direction is indicated by red arrows. At the sampling point the experimentally determined air velocity profile is shown. Measurement devices are arranged as follows: APS (1), OPS (2), ELPI+ (3), DT (4), PM impactor (5). Adapted with permission from Farwick zum Hagen et al. [92]. ©2019 American Chemical Society.

used as control instrument allowing a continuous monitoring of the measurements. At the air inlet of the setup, an additional HEPA H13 filter was installed. The incoming air was routed with a metallic tubing (tube diameter, $d_{tube} = 150\,mm$) into a circular chamber that fully enclosed the entire brake assembly. The chamber consisted of two metallic semi-monocoques installed on top of each other. The chamber walls near the drive shaft were removable for easy maintenance. All gaps between the individual components, particularly the gap between the drive shaft and the chamber walls, were sealed. The circular chamber geometry had a small volume of about $0.2\,m^3$, and thus a volume exchange time of less than three seconds

for $Q_{setup} = 250\,m^3/h$. Viewing from the engine into the direction of the brake, the air inlet was positioned at the lower left hand side of the chamber. The air outlet was located at the top of the chamber in centered position. This arrangement of the air inlet and outlet positions revealed optimal air flow conditions inside the chamber. The corresponding CFD simulations indicated turbulent air flows, from which a well intermixing between particles and clean air was expected. At the same time, dead air spaces were mostly avoided. Further CFD results will be discussed in the next paragraph. At the air outlet, the tube was routed vertically upwards, followed by an inverted U-bend with two 90° bends with radii $r_1 = 2\,d_{tube}$ and $r_2 = 5\,d_{tube}$. On one hand, the U-shaped aerosol path reflected an ideal configuration regarding particle losses (will be discussed later) and further mixed the aerosols. On the other hand, this geometry manipulated the air flow inside the tube resulting in locally varying air velocities. Looking at the cross-sectional air velocity profile at the sampling point in figure 3.2, higher air velocities were observed towards the edge of the tubing.

Isoaxial sampling took place inside the straight tube section between the bend B_2 and the branch by several measurement devices. Each device was connected with a separate sampling line and the probes were oriented side by side as it is shown in figure 3.2. On sampling side, the probes consisted out of nozzles that were designed for isokinetic sampling. Due to the straight and direct routing of the tubes to the measurement devices additional bends were avoided, which further would have reduced particle losses. Further setup details are described by Farwick zum Hagen et al. [92].

3.1.2 Air Flow and CFD Calculation

The air flow inside the chamber and the aerosol path was analyzed in two steps. Initially, CFD calculations were performed, which pointed out the optimal arrangement of all setup components. In a second step, the CFD calculated air flows were experimentally validated.

The air velocity profile proposed by CFD calculation is shown in figure 3.3 (a) for the longitudinal section of the setup. The incoming air at the lower left hand side directly faced the friction interface underneath the brake caliper. This ensured an efficient brake cooling at all times during the measurements. Furthermore, particle image velocimetry (PIV) studies of disc brakes obtained the largest particle release

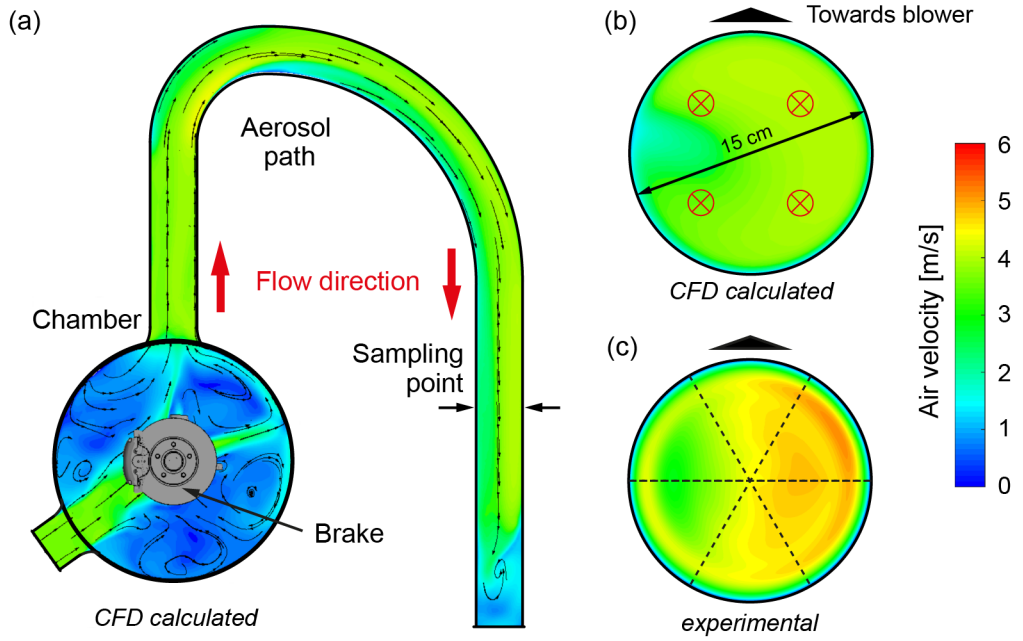

Figure 3.3 – **Air velocity profiles** of the experimental setup (red, high air velocity; blue, low air velocity). (a) CFD calculated air velocity profile along the transverse section of the chamber and the aerosol path. Red arrows indicate flow direction. Small black arrows indicate local flow directions. Cross sections of the CFD calculated and experimentally determined air velocity profiles at the sampling point are shown in (b) and (c), respectively in top view perspective. Experimental air velocity measurements were performed along the dashed lines and the data was interpolated. Adapted with permission from Farwick zum Hagen et al. [92]. © 2019 American Chemical Society.

directly at the friction interface, just shortly behind the brake caliper in the rotational direction [87]. In the present setup, the brake rotation was counterclockwise and thus, the particles were released exactly within the air stream. In consequence, a complete mixing of the brake dust with the incoming air was assumed.

The air velocity within the setup tubing was in the range of 2.5-4.5 m/s. Especially in the curvature section, it dropped down to about 1.5 m/s at the inside of the bend. However, due to the second bend B_2, which had a slighter curvature compared to B_1, the air velocity calmed down. Thus, at the sampling point, the cross-sectional air velocity profile showed only small variations. The CFD results were experimentally validated by air velocity measurements using a hot-wire anemometer (air velocity transducer, TSI 8455) at different points along three axes inside the tubing. A subsequent interpolation of the data points created a comparable air velocity profile,

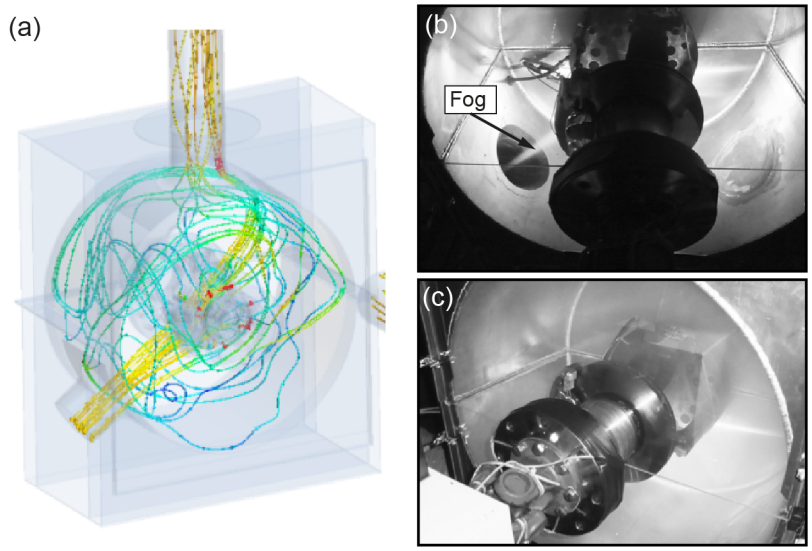

Figure 3.4 – Air Flow inside the chamber. (a) CFD calculated air velocity lines. Pictures of the air flow inside the chamber visualized with a smoke plume is shown in (b) and (c).

which is shown in figure 3.3 (c). The absolute values of the experimental profile were slightly higher than that of the CFD calculated one. However, the patterns are identical: a slightly higher air velocity was observed on the right-hand side of the tube. This corresponds to the different air velocities inside the bent tube section and confirms the findings of the CFD model.

As already mentioned, one quality feature of the setup was the well mixing of the dust with the incoming air. In the CFD model, most of the incoming air spread within the chamber and dead air spaces were prevented. Only a narrow short cut was formed between air inlet and outlet of the chamber. Proving the turbulent air flow inside the chamber, experiments with a fog generator were performed. In order to view inside the chamber, the metallic chamber walls were exchanged with transparent acrylic glass windows. A smoke gun was positioned in the center of the air inlet and the smoke was dosed in successive bursts as shown in figure 3.4 (b) and (c). Initially, a narrow smoke plume was entering the chamber as it is shown in the first picture. Shortly thereafter, the entire chamber was misted (second picture) and when the fog dosing had stopped the chamber cleared out immediately. This confirmed the turbulent air flow and dust mixing inside the chamber and predicted an immediate mixing of dust with incoming air.

3.1.3 Particle Loss Calculation

The aerosol path of the setup was designed for minimal particle losses. Nevertheless, particle losses were still present and estimated through empirical models [27]. The aerosol path was subdivided into four segments: the straight tube section above the chamber ($l_1 = 500\,\text{mm}$), the bends B_1 and B_2, and the straight tube section at the sampling point ($l_2 = 500\,\text{mm}$). For each segment, the transport efficiency (η_{trans}) was calculated considering models for turbulent inertial deposition (Liu and Agarwal, 1974 [117]), diffusional losses (Friedlander, 1977 [118]), gravitational settling (Yamano and Brockmann, 1989 [119]), and inertial losses in bends. For the latter loss mechanism, different models were applied (Pui et al., 1987 [120]; McFarland et al., 1997 [121], and Crane and Evans, 1977 [122]). Any other loss mechanisms were not considered because their influence on η_{trans} would have been marginally small. The total transport efficiency of the setup was determined through the product sum over the η_{trans} of each loss mechanism and flow segment [27],

$$\eta_{\underset{\text{trans}}{\text{total}}} = \prod_{\substack{\text{flow}\\ \text{segments}}} \prod_{\substack{\text{mecha-}\\ \text{nism}}} \eta_{\substack{\text{tube,}\\ \text{turb. inert.}}} \cdot \eta_{\substack{\text{bend,}\\ \text{inert.}}} \cdot \eta_{\substack{\text{tube,}\\ \text{diff.}}} \cdot \eta_{\substack{\text{tube,}\\ \text{grav.}}}. \tag{3.1}$$

The resulting $\eta_{\text{total,trans}}$ of the aerosol pathway depending on d_p is shown in figure 3.5 (a). Over a wide size range from $d_p = 10\,\text{nm}$ to about $3\,\mu\text{m}$, $\eta_{\text{total,trans}}$ was nearly 1 meaning that all particles in this range were expected to be transported loss-free. There was only a small decrease for particles of around 10 nm size, which resulted from diffusional losses. Larger sized particles in the coarse size range were more effected by impaction and gravitational settling. Starting at about 3 µm sized particles, the mean $\eta_{\text{total,trans}}$ decreased to about 0.8 for 20 µm large particles. Depending on the model, losses of up to 28 % were possible for large particles. But for PM_{10}, the mean $\eta_{\text{total,trans}}$ values were still found to be greater than 0.95. Overall, the transport efficiency was assumed to be excellent since significant losses only for particles greater than 10 µm were expected.

Note, that some models were only defined for a limited parameter range, which is usually given in terms of Stokes number. Therefore, this estimation was only used for setup validation and not for data correction during the analysis phase. As an example for potential setup optimization, figure 3.5 (b) shows the mean $\eta_{\text{total,trans}}$ values for different setup flows and tube dimensions. For smaller d_{tube} or higher

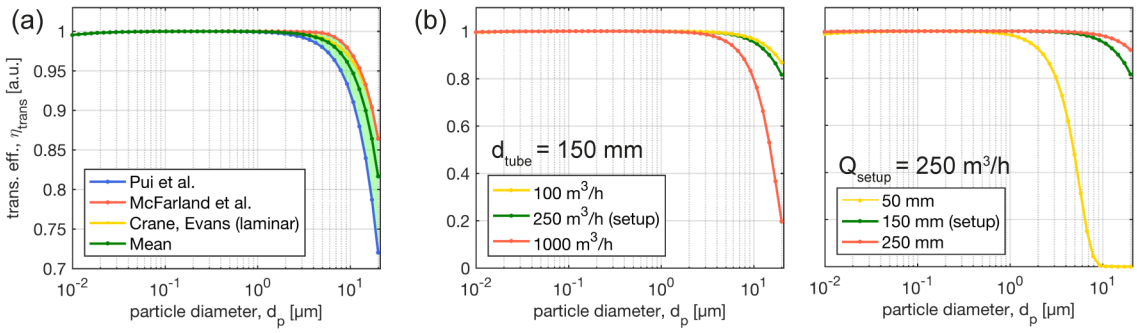

Figure 3.5 – **Transport efficiency** of different sized particles within the setup tubing. (a) Consideration of different particle loss models using setup parameters (Q_{setup} = 250 m^3/h and d_{tube} = 150 mm). (b) Comparison of mean values with different setup flows (Q_{setup}, left) and tube diameters (d_{tube}, right).

air flows, $\eta_{total,trans}$ became lower. While for lower air flows and larger d_{tube}, the efficiencies were improved marginally. Although potential improvements regarding particle losses were possible, they would have led to a weaker brake cooling and a poor signal strength. Therefore, the chosen parameters of d_{tube} = 150 mm and Q_{setup} = 250 m^3/h reflected optimal test conditions.

As a final remark, the sampling nozzles of the probes may also cause particle losses. It is proposed that isoaxial and isokinetic sampling with "thin-walled" nozzles results in 100 % aspiration [27]. However, the sampling nozzles used within the present work were not fulfilling Belyaev and Levin's [123] condition for "thin-walled" nozzles because of manufactural and practical reasons. But since the geometries of the sampling nozzles were close to "thin-walled" conditions, the resulting particle losses were assumed to be small [29].

3.1.4 Verification of Aerosol Sampling

Sampling position. The measurement setup described in section 3.1.1 was designed in a compact configuration because the available space at the dynamometer was restricted by the test room dimensions. This meant that the location of the measuring plane did not meet standardized recommendations for particulate matter measurements in ductworks. For example, the ISO 9096:2017 norm defines the position of the sampling plane to be in straight tube sections with a length of at least 5 d_{tube} in upstream and in downstream direction [124]. Similarly, air flow measure-

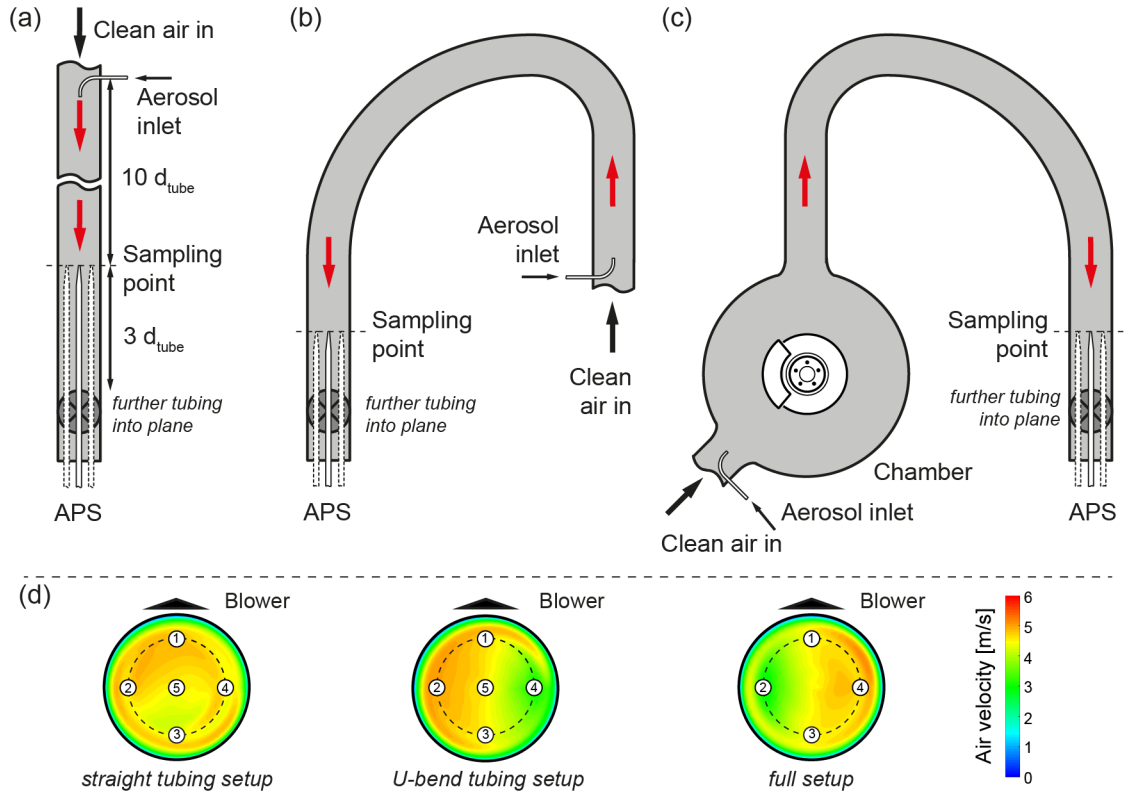

Figure 3.6 – Setups for premeasurements. (a) Straight tubing arrangement in the area of the sampling point. (b) U-bend tubing section and (c) full setup arrangement with chamber and brake. The air flow direction is indicated by red arrows. In (d) the corresponding air velocity profiles are shown.

ments should take place in straight tube sections. For high accuracies, straight tubes of about $7\,d_{tube}$ length upstream and $3\,d_{tube}$ length downstream from the sampling plane are recommended [125]. In order to address this issue, several measurements with different setup configurations were performed. Furthermore, the intermixture of test aerosols inside the aerosol path as well as the potential influence of measuring at different sampling positions was analyzed.

For the investigation three different pre-measurement setups were created, which are shown in figure 3.6. The main part of the first setup was composed out of a vertically oriented straight tubing. The sampling plane was located at $10\,d_{tube}$ distance from the last bend downstream and $3\,d_{tube}$ from the branch in upstream direction. As this was close to the recommended measurement conditions mentioned above, this setup served as reference. In a second setup, the tube routing was changed

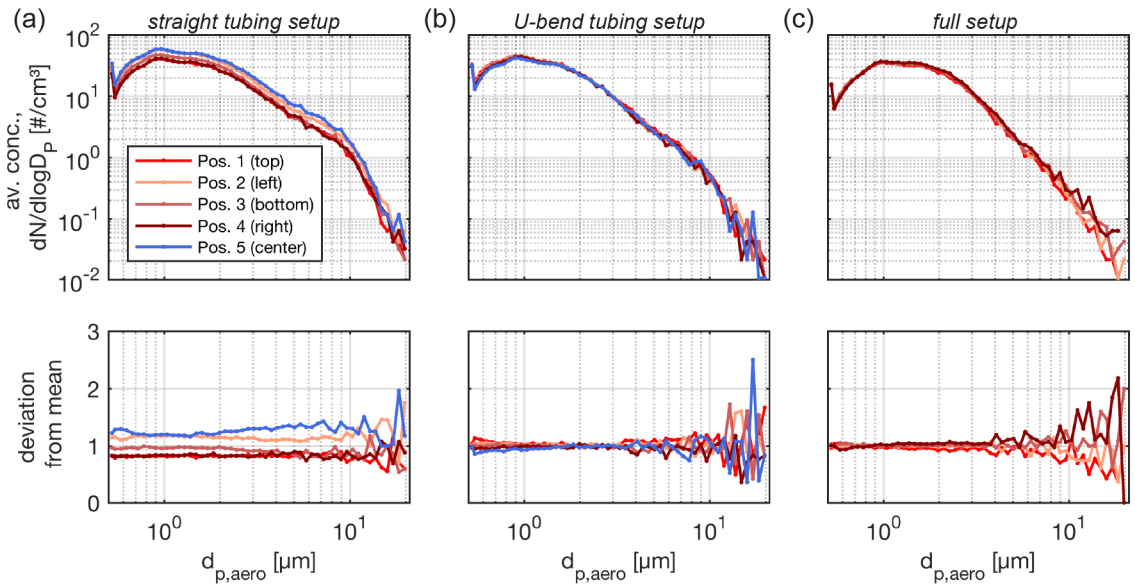

Figure 3.7 – Validation of sampling positions. (a) Straight tubing setup, (b) U-bend tubing setup and (c) full setup arrangement with chamber and brake. Diagram order from top to bottom: averaged particle size distribution measured by TSI APS and deviation from mean value.

similar to the final dynamometer setup but the tube was bent in opposite direction. The third pre-measurement setup was designed similar to the final setup as it included the brake and the enclosing chamber. For all three setup configurations, the air velocity profiles were determined for a constant setup flow of 250 m^3/h (compare figure 3.6 (d)). Although the first setup represented optimal measurement conditions, the air velocity profile still showed some irregularities. However, in the center of the tubing the air velocity was still in the range of 4.3-4.8 m/s and thus the deviations were expected to be of minor relevance. In case of the setups with bent aerosol paths, the air velocity profiles showed higher flows on the respective opposite sides of the bends. Again, the velocity pattern resulted from the bend that was located directly upstream of the sampling plane. The air velocity varied from about 3-5.3 m/s, which may influence the aerosol sampling when probes are drawn at different position within the tube cross section.

The potential influence of sampling at different positions in the tube cross section was investigated through measurements with test aerosols. At the aerosol inlet positions, which are marked in the sketches of figure 3.6 (a) to (c), a rotating brush

generator (Palas RGB1000) released A1-dust (Arizona road dust, PTI 12103) at a constant flow rate. On the sampling side, the APS was connected successively to different probe sites within the tube cross section. For each probe position the particle number distribution was determined by averaging over an interval of three minutes. The resulting size distributions are shown in figure 3.7. For each setup, the average particle size distributions were close together and differences were hard to find. But the deviation from the mean values, showed even more precise results: small differences of about 20-30 % in particle number concentrations were found for the measurements using the first setup. In contrast, nearly identical results were found for measurements within a setup that contained the U-shaped tubing. Only deviations for larger particles with a random characteristic were observed during these tests. Since the measured signal was rather small in this range, the deviations were attributed to the instrument noise. Apparently, the test aerosol was much better diluted and intermixed inside the bent aerosol path than in the straight tube section. The weaker aerosol mixing inside the straight tube may resulted from the release spot in the center of the tubing. An aerosol source that releases the particles on a broader area might have improved the results. However, the investigations clearly showed that there was no difference in particle concentration to be expected when sampling at different positions inside the tubing.

Isokinetic sampling. In section 2.1.2 the importance of proper aerosol sampling was introduced. Whenever samples are drawn from a stream of air, the probes should be isoaxially aligned and isokinetic sampling conditions should be fulfilled. In order to evaluate the setup robustness regarding isokinetic sampling, a separate investigation has been performed: while the nozzle inlet was kept constant, the particle number size distributions of the test aerosol were analyzed by the APS for different air flows. The averaged concentrations are shown in figure 3.8. As shown in the diagram, with increasing air flow the artificial aerosol was more diluted and as a consequence the concentration decreased. When comparing the size distributions to the data that was obtained with the appropriate sampling nozzle (4.8 mm at 250 m^3/h), no significant deviation was found. This was also confirmed by the theoretically calculated aspiration efficiencies (η_{asp}) considering the model from Belyaev and Levin [126].

When nozzles with different inlet diameters were analyzed during experiments

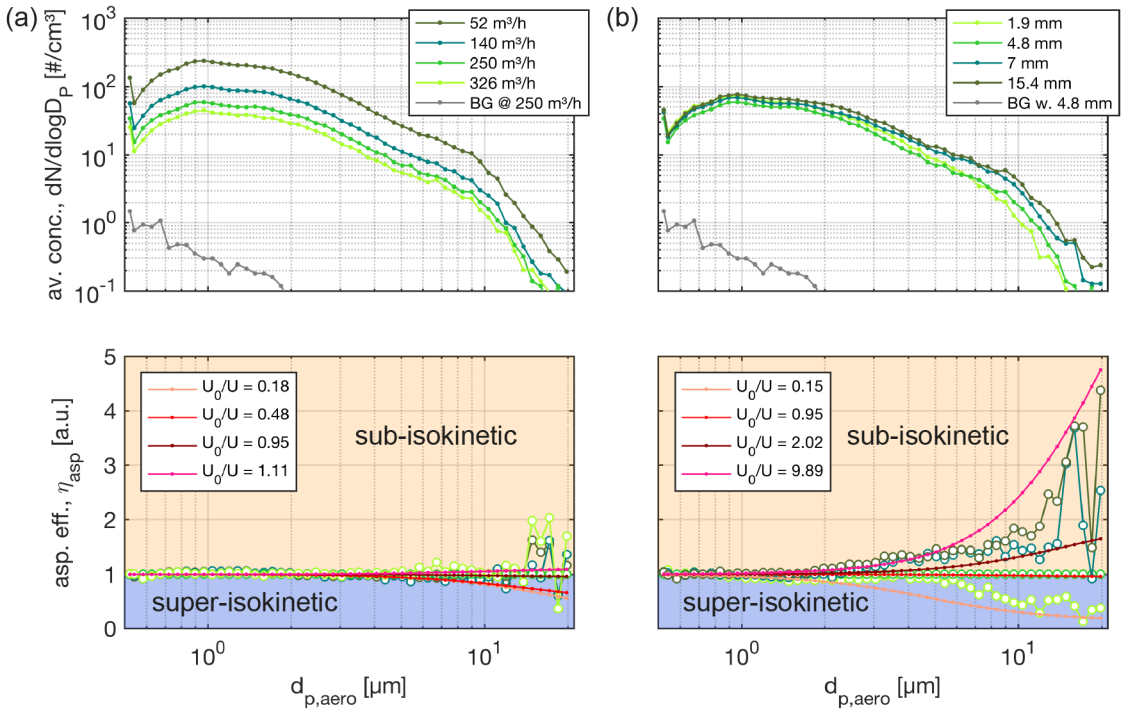

Figure 3.8 – Simulation of the isokinetic effect. The tests are performed with the straight tubing setup with the TSI APS at center position. In (a) the nozzle inlet size is kept constant (4.8 mm) and the setup flow is varied and while in (b) the flow is constrained at 250 m^3/h and different nozzle diameters are tested. Diagram order from top to bottom: Averaged particle number size distribution and the corresponding aspiration efficiency (η_{asp}). The experimental values are normalized to the averaged values of size classes 0.5-1 µm. Theoretical expectations are shown according to the model by Belyaev and Levin [126] in reddish colors.

with a constant setup flow of 250 m^3/h, more significant results were obtained (figure 3.8 (b)): the particle number size distributions for fine particles with around 1 µm diameter were nearly identical for all tested nozzles. But the deviation was more pronounced for larger particles. Especially when looking at η_{asp}, larger particles were sampled with different yields. As the theoretical model predicted, for sub-isokinetic and super-isokinetic sampling the results were over- and underestimated, respectively. As a conclusion, the results underlined the necessity of sampling isokinetically with appropriate nozzles - especially when PM_{10} is investigated. For $PM_{2.5}$ and particle number measurements the geometry of the sampling nozzle is less critical. Thereby, variations of the setup air flow were found to be small and deviations of up to 10% can be tolerated.

3.2 Drive Cycles

In focus of the present work were emission investigations under realistic driving conditions. Here the applied driving profile was of significant relevance since it should also be representative for normal driving behavior. Two test cycles were developed for the present investigation.

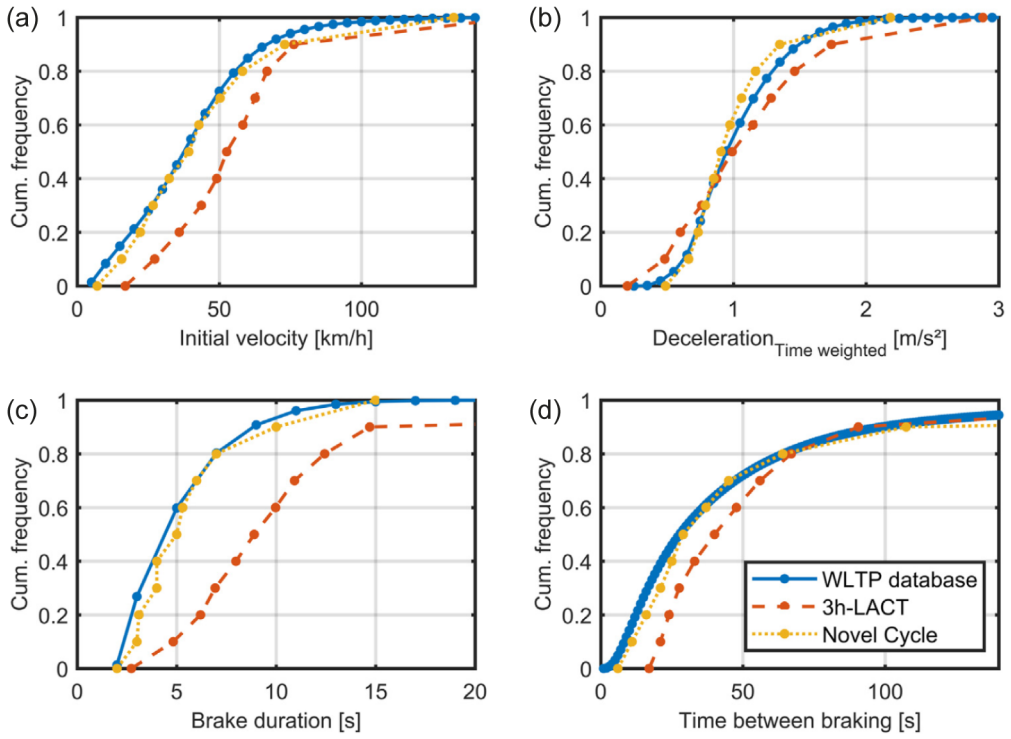

Figure 3.9 – Drive cycles. Cumulative frequency distributions of the WLTP database (blue), the 3h-LACT (orange) and the WLTP cycle (yellow) with regards to (a) initial velocity, (b) deceleration, (c) brake duration, and (d) time between braking. Reprinted with permission from Mathissen et al. [127]. ©2018 Elsevier.

The first one is based on the five day long Los Angeles city traffic (LACT) cycle. The cycle was developed from real driving journeys in Los Angeles. Since the cycle length was too long for repeating wear investigations, a three-hour long subsection was used (3h-LACT). The subsection was chosen in such way that characteristic parameters, e.g., initial velocities, deceleration, or brake duration, were most similar to that of the entire cycle. The final cycle contained 217 brake stops with initial

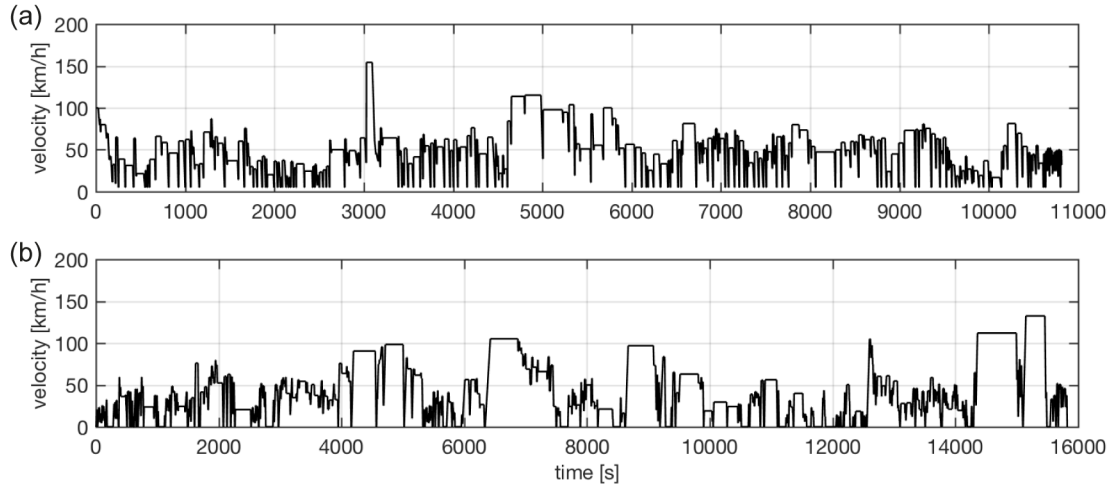

Figure 3.10 – Velocity profiles of drive cycles (a) 3h-LACT and (b) WLTP. Based on ref. [128, 129].

velocities in the range of 16.9 km/h to 154.3 km/h and decelerations ranging from 0.3 m/s^2 to 2.88 m/s^2 [127, 128].

The second cycle was composed out of the worldwide harmonized light-duty vehicles test procedure (WLTP) database. The WLTP database contains 743,694 km of real-world driving data collected in five regions (EU, USA, India, Korea, and Japan). Using this data as a basis, an artificial drive profile was developed while also characteristic parameters were considered [127]. The cycle consisted out of 303 brake stops with an average velocity of 46.5 km/h and a maximum velocity of 132.5 km/h. The decelerations varied between 0.49 m/s^2 and 2.18 m/s^2 [127]. A further characterization regarding certain parameters is shown in figure 3.9. Here, also a comparison to the 3h-LACT cycle is given. The final velocity profiles of the two cycles are shown in figure 3.10.

3.3 Test Procedure

A conventional 15” disc brake with floating caliper, grey cast iron brake disc, and LM brake pads of a midsize passenger car was used as test specimen. In order to investigate the bulk material of the pad lining, the friction surface was machined down by 2 mm. Three temperature sensors were installed at the brake: the first thermocouple sensor was embedded inside the disc at a depth of 0.5 mm in the

middle of the friction surface, another one was embedded inside the outer pad lining (1.5 mm depth), and the third one was used as a sliding thermocouple sensor (GA4089, Universal Thermosensors LTD) that was pressed against the rotor surface with a contact force of 1 N (see figure 3.1 (c)).

The tests were performed with a moment of inertia of 50.4 $\mathrm{kg\,m^2}$, which corresponds to the vehicle curb weight plus one passenger. This included a brake power distribution between front and rear brakes of 71.6 % and 28.4 %, respectively. This assumption was based on the different sized friction surfaces of the front and rear brakes. The following drive cycles were performed in successive order:

1. **3h-LACT cycle.** The 3h-LACT cycle was used in temperature- instead of time-controlled mode. Originally, the cycle was used in time-controlled mode, which means that the brake stops were performed after certain time periods. In the temperature-controlled mode, the brake stops were triggered when the brake cooled down to a certain initial temperature (T_i). This method allowed standardized investigations independently from the brake cooling. Thus, the comparability to measurements with competing setups was given, which may stand out through better brake cooling.
   In a first session, five successive runs of the 3h-LACT were performed with initial temperatures obtained from usual dynamometer measurements with the full LACT cycle ($T_\mathrm{i,lab}$). Before and after each run, the brake was rotating at a vehicle velocity of 100 km/h. For material cleaning and tempering of the brake, five static brake stops were performed before each test (coefficient of friction (COF) check) [128]. After the session, the weight loss of the brake material was analyzed.

2. **Rotation only.** Due to the weight loss analysis of the previous session a brake maintenance was needed. This allowed a very specific way of testing: "Rotating only" maneuvers were driven in order to investigate brake drag emissions, which is the release of brake wear particles during cruising [89, 92]. At the same time, potential particle resuspension inside the setup could be analyzed. For certain setup configurations, i.e., with or without brake caliper mounted or clean and impure chamber environments, the brake was rotating at certain constant velocities.

3. **3h-LACT cycle with advance vehicle simulations.** As described by Farwick zum Hagen et al. [92], another investigation with a different T_{i} data set was performed. Approaching more realistic test conditions, the sixth 3h-LACT run was conducted with initial temperatures obtained from the vehicle ($T_{\mathrm{i,veh}}$). During this run, additionally parasitic drag simulations were applied according to Mathissen et al. [127].

4. **WLTP cycle with advance vehicle simulations.** The WLTP cycle was found to be more representative for realistic driving than the 3h-LACT cycle [127]. Therefore, a final investigation with the WLTP cycle was performed, which also included parasitic drag simulations. The WLTP cycle was driven in time-controlled mode. Each of the ten cycle sections started when the brake was cooled down to ambient temperatures (30°C). Thus, the entire WLTP cycle simulated ten single test drives.

3.4 Brake Wear Emissions

One side effect of temperature-controlled testing is the potential variation of test duration and driving distance. Once the variations are high, they may impede direct comparisons between tests. Thus, it is important to judge, whether or not tests were conducted in a repeatable manner. In table 3.1 the test parameters for each 3h-LACT cycle are listed. For all five tests of the first session, very similar driving distances in the range of 165.4-170.56 km and test durations of 195.1-200.9 min were found. Therefore, a high test-to-test repeatability was assumed. In case of the sixth run, which was performed with advanced vehicle simulations, both the cycle duration and driving distance were found to be much larger than during the former tests. This was due to the initial brake temperatures, which were found to be lower on the vehicle than in the laboratory. It led to longer cool-down phases that were accompanied by disc rotations at certain initial velocities. Thus, also the absolute driving distance became longer.

Table 3.1 – Test parameters for each cycle.

Run number	Driving distance [km]	Cycle duration [min]
1st run	170.56	200.9
2nd run	165.40	195.1
3rd run	168.60	198.7
4th run	167.38	197.5
5th run	169.96	200.0
6th run [a]	*280.81*	*307.9*

[a] Test with vehicle brake temperatures and parasitic drag (advanced vehicle simulations).

3.4.1 Time Resolved Emissions

3h-LACT cycle. For all tests a temporal overview was prepared, which allowed an easy evaluation of the results. As an example, the fifth run of the 3h-LACT cycle is shown in figure 3.11. In the first diagram, the driving profile is shown along with the actual brake temperatures. In parallel, the current PM_{10} concentrations and the particle number size distributions are plotted underneath. Certain sections of the diagram are presented in figure 3.12 in more detail. Here the COF check can be seen clearly, which included the background recording, running-in, and cleaning phases. Furthermore, the brake events and their corresponding emission peaks are clearly identifiable.

Inspecting the brake temperature signal over the entire test, it was found that all three temperatures were closely matching. The pad temperature was found to be slightly lower, which arose most likely from the lower heat conductivity of the pad lining compared to the disc material [130]. The good agreement of the brake temperatures indicated a robust measurement.

Farwick zum Hagen et al. [92] reported the following emission observations: the PM_{10} concentration correlated exactly with the brake events and concentrations were found in the range of 0.01 mg/m^3 to ≈20 mg/m^3. In terms of particle number, the emission peaks were also assigned to the brake events and multimodal particle number distributions were found. During braking, initial modes in the coarse and fine particle size range were observed (compare figure 3.12 (b)). The modes appeared to be bimodal with peaks at around 2-3 µm and 100-200 nm. In case of a high brake temperature increase beyond ≈170°C, a further mode appeared in the nucleation range at around 5-40 nm. The nucleation mode occurred, after the fine

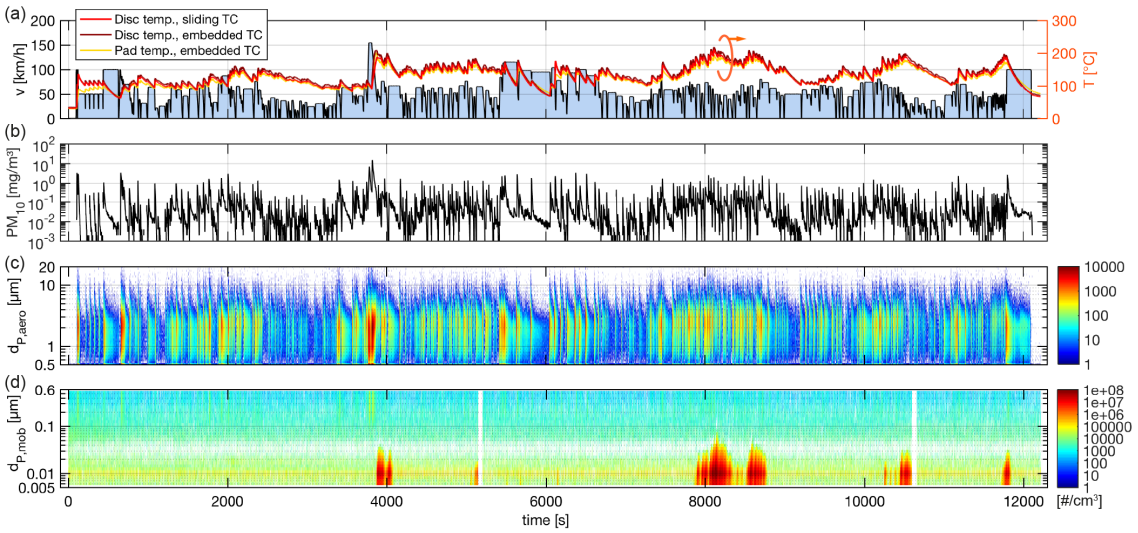

Figure 3.11 – Temporal overview plot of 3h-LACT cycle of the fifth run. (a) Velocity profile (black, left axis; blue area, driving distance, here: 170 km), disc temperatures (right axis; dark red, embedded TC; red, sliding TC) and pad temperature (yellow, embedded TC) curves. (b) PM_{10} concentration of TSI Dusttrak. For clarity, only raw data are shown. (c) Particle number concentration ($dN/dlogd_p$) of TSI APS depending on aerodynamic diameter, $d_{p,aero}$. (d) Particle number concentration ($dN/dlogd_p$) of TSI EEPS depending on electric mobility diameter, $d_{p,mob}$. The raw data are multiplied with a dilution factor of 8.05. Adapted with permission from Farwick zum Hagen et al. [92].

mode nearly disappeared. The different size distributions during the mode shift are shown in figure 3.13. At the end of the brake event, when the brake remained at high temperatures, the ultrafine mode dominated the particle size distribution.

The independent appearance of the two modes suggests different particle generation processes: fine particles were generated by mechanical abrasion [68] and ultrafine particles were formed through condensated vapor followed by coagulation and agglomeration [69, 100]. Furthermore, it is believed that the majority of ultrafine particles were generated at hot-spots or local asperities. Here, local brake temperatures were expected to be higher than the macroscopic recorded brake temperature [92]. Thus, it is assumed that the ultrafine particles are of volatile nature. This assumption found agreement in a recent measurement by Mamakos et al. [131]. Also Perricone et al. [132] reported similar observations.

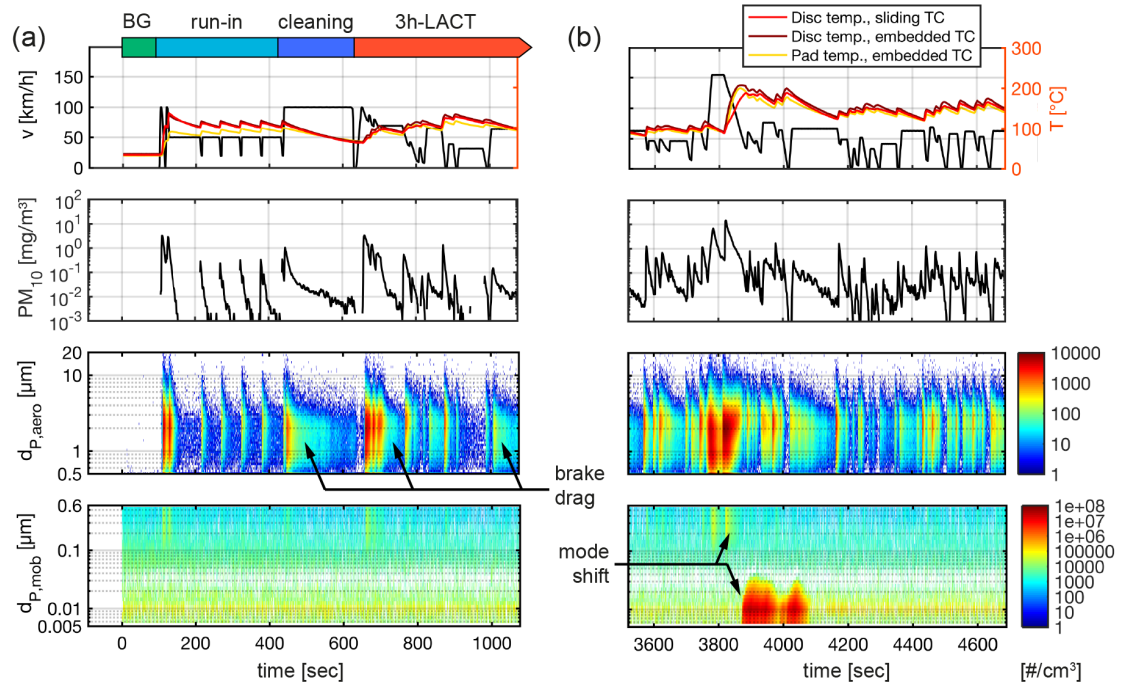

Figure 3.12 – Temporal overview plot of certain sections within the 3h-LACT cycle, fifth run: (a) Background, run-in, and cleaning phases are shown. During constant driving phases emissions are observed resulting from brake drag. (b) Mode shift during brake event at high brake temperatures. Reprinted with permission from Farwick zum Hagen et al. [92]. ©2019 American Chemical Society.

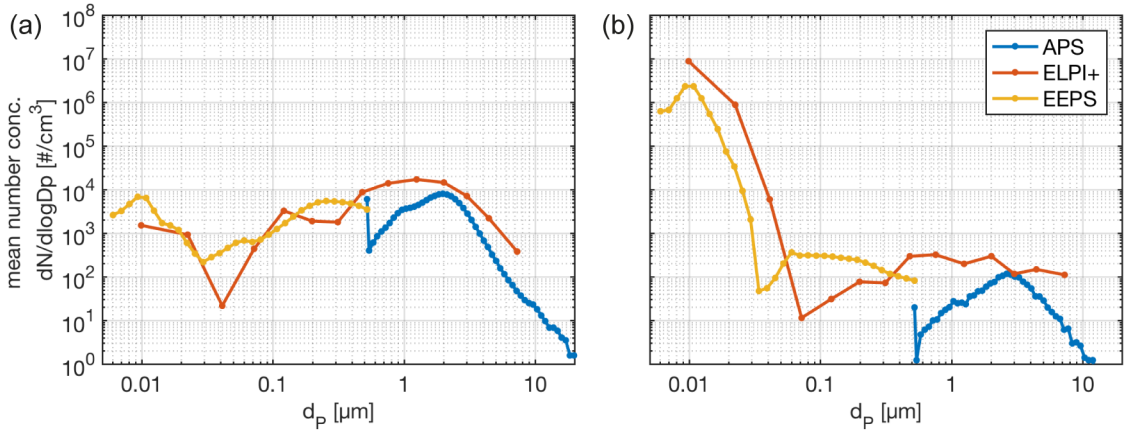

Figure 3.13 – Particle number size distributions during braking. The particle number concentrations are averaged over ten seconds. (a) At the beginning of the high speed brake stop (highlighted in figure 3.12 (b)) and (b) after 60 s (at the end of the brake stop).

WLTP cycle. The temporal overview of the WLTP cycle is shown in figure 3.14. Each of the driving sections was separated by the extended cool down phases leading to an even longer test duration. All brake temperature sensors showed similar values, which indicated a robust measurement. Similar to the 3h-LACT also the PM_{10} concentrations were found to be in the same range. Apparently, compared to the 3h-LACT, the softer brake characteristic of the WLTP showed no influence on the particle mass emissions. In contrast, the particle number emissions were significantly reduced. Over the entire cycle length not a single emission peak in the ultrafine particle size range was found. All the brake emissions were generated in the coarse and fine particle size range. These observations are consistent with previously mentioned assumption that ultrafine particles are only emitted during high temperature phases. During the WLTP cycle, the maximal brake temperatures were around 170°C. Obviously, ultrafine particles are expected to be generated at even higher temperatures. The particle emission behavior depending on the brake temperature will be discussed in more detail later.

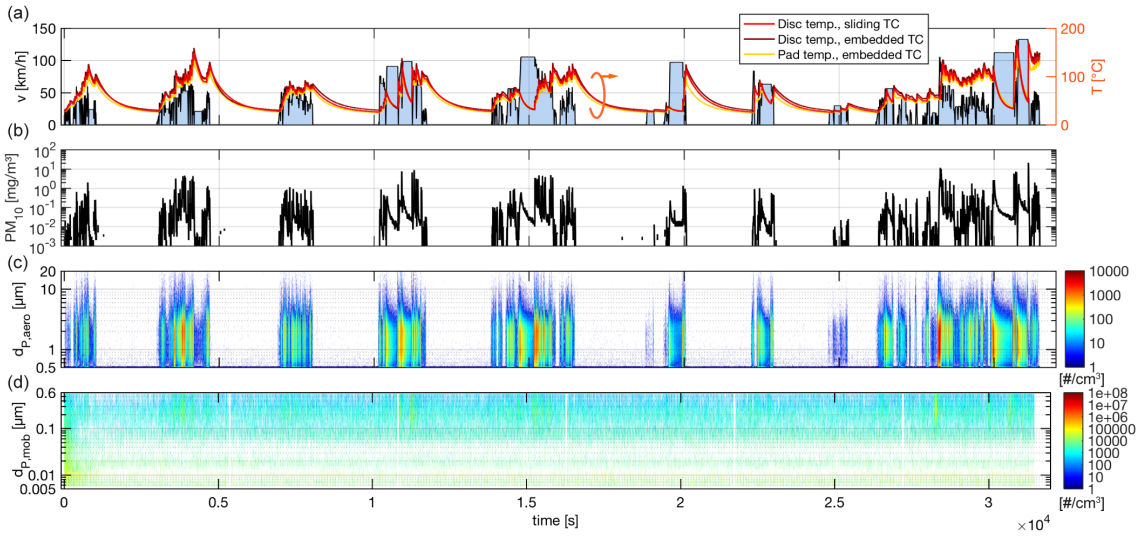

Figure 3.14 – Temporal overview plot of WLTP cycle after the sixth run of the 3h-LACT. (a) Velocity profile (black, left axis; blue area, driving distance, here: 193 km), disc temperatures (right axis; dark red, embedded TC; red, sliding TC) and pad temperature (yellow, embedded TC) curves. (b) PM_{10} concentration of TSI Dusttrak. For clarity, only raw data are shown. (c) Particle number concentration ($dN/dlogd_p$) of TSI APS depending on aerodynamic diameter, $d_{p,aero}$. (d) Particle number concentration ($dN/dlogd_p$) of TSI EEPS depending on electric mobility diameter, $d_{p,mob}$. The raw data are multiplied with a dilution factor of 7.71.

3.4.2 Cumulative Analysis and Emission Factors

Filter Analysis. The total airborne PM_{10} emissions were obtained by filter analysis with the cascade impactor and the Dusttrak. The first stage of the impactor (PM_{TSP-10}) and a PM_{10} impactor installed at the Dusttrak served as PM_{10} separators. Since both devices sampled with different flows ($Q_{Dusttrak} = 2 \pm 0.04\,l/min$ and $Q_{impactor} = 10 \pm 0.5\,l/min$ [33, 34]), the resulting cumulative filter load deviated. Compensating this, the raw filter load (Δm_{filter}) was extrapolated as follows:

$$\Delta m_{extrapol} = \frac{Q_{setup}}{Q_{device}} \Delta m_{filter}. \tag{3.2}$$

For each cycle a separate set of filters was used. The results are presented in figure 3.15. For the first 3h-LACT run, the highest emission values were obtained. The PM_{10} emissions were in the range of 1.6-1.9 g. For the following cycle repetitions, the emissions stabilized at constant values of around 0.7-1 g. The higher values at the beginning of the test were attributed to the running-in process of the brake material. In order to protect the disc friction surface from rust, brake discs are usually coated. During the running-in phase the disc coating was worn down and the brake pad and disc were grind into stacked groves, which resulted in higher wear.

In case of testing with advanced vehicle simulations (sixth run), again higher emission values of around 1.2 g were found. The sixth run followed directly after maintenance, when the disc and pad were build out for weight analysis. In order to avoid another running-in phase, the same material was used for further tests. However, the emissions were still higher, which led to the assumption of another running-in phase of the material. Another possibility might be increased emissions through brake drag. The latter origin seems highly possible because the constant driving distances, where brake drag usually occurs, were longer during this run (compare table 3.1). The effect will be discussed in more detail later.

For the WLTP cycle, the emissions decreased, although during this cycle more brake stops were performed. Since here no longer constant driving phases were performed during the cycle, it is another indication that the higher emissions during the sixth 3h-LACT resulted from brake drag.

Independently from the test cycle, the highest PM emissions were always found in the particle size range of 2.5-10 µm. The mass fraction of all other size classes

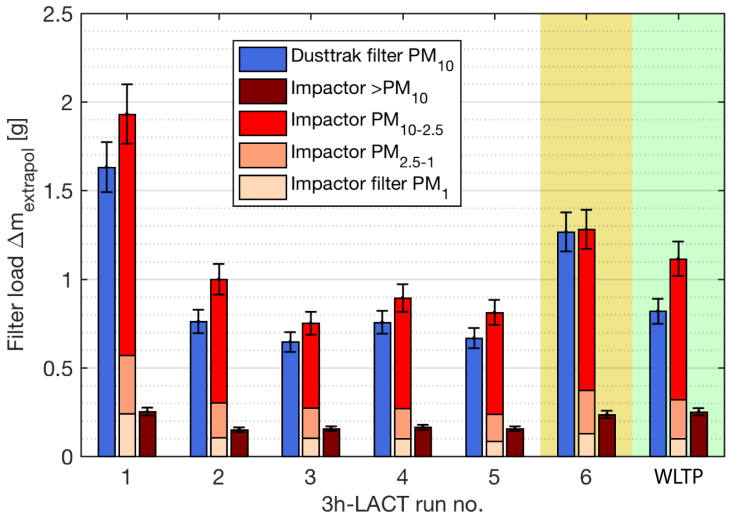

Figure 3.15 – Extrapolated filter load shown for each 3h-LACT run, the 3h-LACT run with advanced vehicle simulations (yellow background), and the WLTP cycle (green background). The first two bins show PM_{10} values and allow direct comparison of TSI Dusttrak and Dekati impactor devices. Error bars result from measurement uncertainty and refer to each bin.

was found to be much smaller. Their share made up approximately 1/3 of the total mass.

The PM_{10} filter load in figure 3.15 was used to determine the airborne fraction of brake wear. Therefore the cumulative filter load of the first five 3h-LACT cycles was compared with weight loss of the brake material during this run. As table 3.2 shows, an airborne fraction in the range of 40.3 % to 48.6 % were found for the Dusttrak and impactor, respectively. These results are in reasonable agreement with the findings of brake wear investigations at competing measurement setups [25, 26]. Similar estimations were also made in receptor modeling studies [18, 107].

Table 3.2 – **Airborne fraction of brake wear** determined by the extrapolated filter load of the TSI Dusttrak and the Dekati PM_{10} impactor. The error values represent the estimated measurement uncertainty. Adapted with permission from Farwick zum Hagen et al. [92]. ©2019 American Chemical Society.

Run number	PM_{10} impactor $\Delta m_{\text{extrapol}}$ [g]	PM_{10} DT filter $\Delta m_{\text{extrapol}}$ [g]	Brake weight loss Δm_{total} [g]
1^{st} run	1.93 ± 0.17	1.63 ± 0.14	na
2^{nd} run	1.00 ± 0.09	0.76 ± 0.07	na
3^{rd} run	0.75 ± 0.06	0.65 ± 0.06	na
4^{th} run	0.89 ± 0.08	0.76 ± 0.06	na
5^{th} run	0.81 ± 0.07	0.67 ± 0.06	na
$\sum_{\text{run no.}1-5}$	5.38 ± 0.47	4.47 ± 0.39	11.08 ± 0.15
airborne fraction	48.60 ± 4.86 %	40.26 ± 4.03 %	

Emission Factors. The particle mass EFs per driving distance are presented in figure 3.16 (a). Due to the nearly constant driving distances for the first runs, in general, their trend is similar to the filter-load data. But surprisingly, also for the sixth 3h-LACT run, the EFs were similar to the previous runs. During this run, the higher filter-load data were compensated through the higher driving distance. When comparing the EFs of the normal 3h-LACT cycle and the WLTP cycle, no big difference was found. However, for the WLTP cycle the EFs were found to be slightly higher. The particle mass EFs were strongly dependent on the measurement technique applied: when considering the filter-based EFs, absolute values in the range of 3.8-5.4 $\text{mg km}^{-1}\,\text{brake}^{-1}$ were found after running-in. But the results obtained by the ELPI+ were about twice as high. This most likely resulted from the conversion from particle number to particle mass, which included assumptions like spherical particle sizes and a uniform particles density of $1\,\text{g/cm}^3$. In contrast, the sensor based Dusttrak results were much lower and in the range of 0.5-2 $\text{mg km}^{-1}\,\text{brake}^{-1}$. Here the device was calibrated by a different aerosol (Arizona Road Dust, SAE J726) that contained a different composition and different light scattering characteristics. When calibrating the sensor based data with the respective filter load, a calibration factor of 6.4 ± 0.7 was determined. This is in very good agreement with the values found in literature [88]. In conclusion, the EFs obtained from filtering are assumed to be the most reliable because the technique itself is considered to be the most robust one.

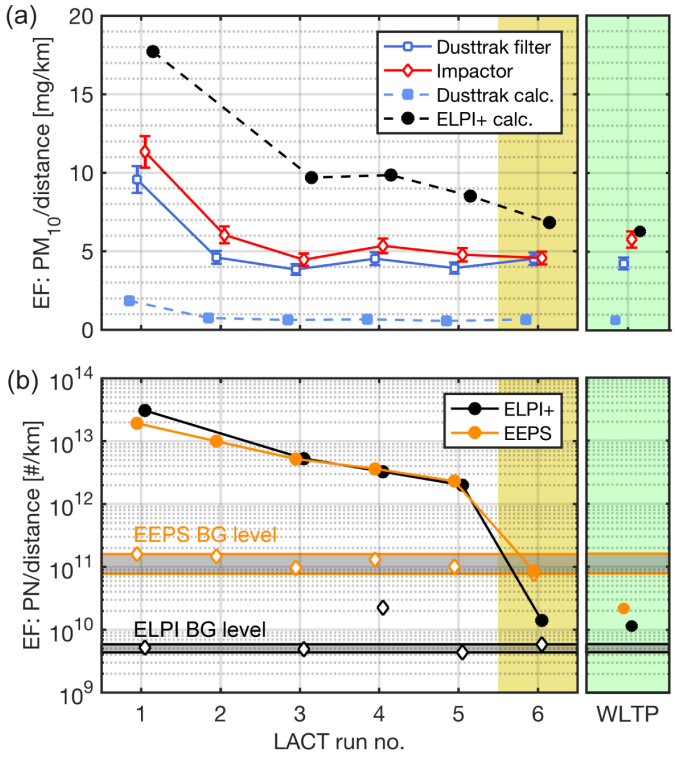

Figure 3.16 – **Emission factors** in terms of (a) PM_{10} and (b) particle number (including volatile particles) per driven distance. The sixth run (yellow background) has been performed with advanced vehicle simulations and is believed to be most representative of real braking. The data points on the green background represent EFs from the WLTP cycle. Error bars refer to measurement uncertainty and the background span indicates the expected background levels (outlier at ELPI+ during the fourth run due to electrode drifting). Adapted with permission from Farwick zum Hagen et al. [92]. ©2019 American Chemical Society.

The particle number EFs are shown in figure 3.16 (b). Starting at 2-3×10^{13} km^{-1} $brake^{-1}$, the EFs decreased with every cycle repetitions to 2×10^{12} km^{-1} $brake^{-1}$ for the fifth run of the 3h-LACT. Thereby, the EFs were significantly higher than the background range, which reflected in case of the ELPI+ also the lower detection limit of the instrument. For the EEPS the background level was even higher as it was influenced by the poor air quality provided to the diluter just in front of it. However, the data were still of reasonable quality so that during the sixth 3h-LACT and the WLTP cycle - both tests with advanced vehicle simulations - EFs at significantly lower values were found. Here the EFs were in the range of 1-9×10^{10} km^{-1} $brake^{-1}$.

For the WLTP, the EFs were similarly around 1-2×10^{10} km^{-1} $brake^{-1}$. Obviously, the EFs were significantly reduced for testing under realistic driving conditions.

3.4.3 Emissions per Brake Stop

In order to investigate the decreasing tendency of particle number EFs, the emissions for each brake stop were analyzed. For analysis, the data sets of the 3h-LACT cycles were used. Each cycle was divided into braking and non-braking intervals. The braking intervals were defined by "brake-ON" signals recorded from the brake dynamometer that lasted for the duration of the braking maneuver. An additional period of four seconds was added to each interval in order to compensate the particle residence time in the aerosol path. The total number of particles was determined as follows [92]:

$$N_{\mathrm{tot},i} = \sum_{j=\mathrm{brakeON}_i}^{\mathrm{brakeOFF}_i+4\mathrm{s}} \sum_{k=1}^{\#\mathrm{Bins}} N_{i,j,k} \cdot Q_{\mathrm{setup}}, \tag{3.3}$$

where $N_{\mathrm{tot},i}$ was the total number of particles for the i^{th}-brake stop. $N_{i,j,k}$ was given as the number of particles of the j^{th}-sample with the k^{th}-bin. Due to the wide particle size range, the data sets obtained by the ELPI+ were used.

As already supposed earlier, the particle number emissions correlate strongly with the brake temperature. Thus, the $N_{\mathrm{tot},i}$ for each brake stop were plotted against the mean brake disc temperature ($\bar{T}_{\mathrm{disc,slidingTC},i}$) during the respective brake stop. In figure 3.17 (a), the results are shown for the first, third, and fifth 3h-LACT cycle run. The most values were in the order of magnitude of 1×10^{9} $stop^{-1}$ $brake^{-1}$ and found in a point cloud until a certain brake temperature, also called critical temperature ($\bar{T}_{\mathrm{crit}}$). The values laying in this range mainly represented the background contribution. But at $\bar{T}_{\mathrm{crit}}$ the particle number emissions increased sharply. For even higher brake temperatures, the particle number emission were about 1×10^{14} $stop^{-1}$ $brake^{-1}$, which was about four orders of magnitude higher than the background level. A similar effect was also reported recently in a pin-on-disc study by Alemani et al. [133]. Interestingly, in the present work, the $\bar{T}_{\mathrm{crit}}$ was found at 140°C, 160°C, and 170°C for the first, third, and fifth run, respectively. The shifting $\bar{T}_{\mathrm{crit}}$ to higher temperatures during each cycle repetition suggests different volatilization-onset temperatures of different organic compounds in the pad lining [92]. It can be

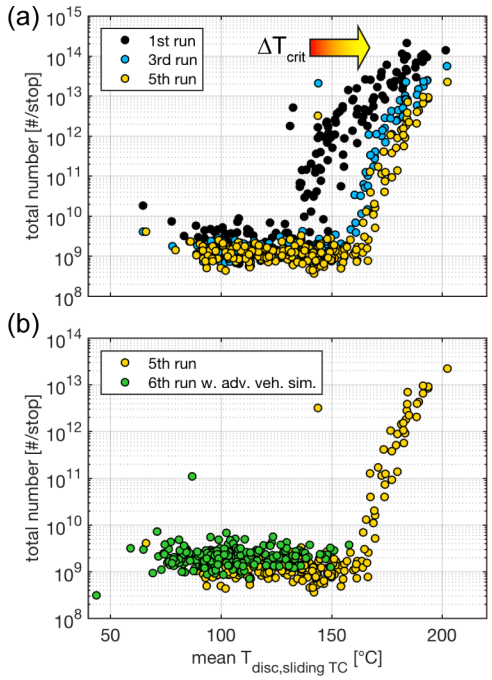

Figure 3.17 – Total PN emission values for each brake event obtained by the Dekati ELPI+. Total number dependency upon $T_{\mathrm{disc,slidingTC}}$. (a) For the first, third, and fifth cycle run. (b) Comparison of laboratory data and data obtained with advanced vehicle simulations. Adapted with permission from Farwick zum Hagen et al. [92]. ©2019 American Chemical Society.

understood as part of the running-in process of the brake material. But it should be noted that stable emission characteristics were not reached after the fifth 3h-LACT cycle. Due to the shift of $\bar{T}_{\mathrm{crit}}$ with every repetition, the number of high emissive brake stops decreased steadily. This also explained the decreasing trend of the EFs in section 3.4.2.

In case of the sixth cycle, the entire particle number emissions were found below the $\bar{T}_{\mathrm{crit}}$ of the previous run. In consequence, the emissions were all below $1{\times}10^{10}\,\mathrm{stop}^{-1}\,\mathrm{brake}^{-1}$ (except one outlier), which was close to the background level. The lower brake temperatures were achieved by using the realistic $T_{\mathrm{i,veh}}$ values. Thus, for the conventional and run-in brake material, ultrafine particle generation is not expected at operating temperatures below 170°C.

The strong particle number dependency upon brake temperature is a very unique characteristic for brake emissions, which is only valid for the particle number. As it is shown in figure 3.18 (b), when considering particle mass concentrations, the data

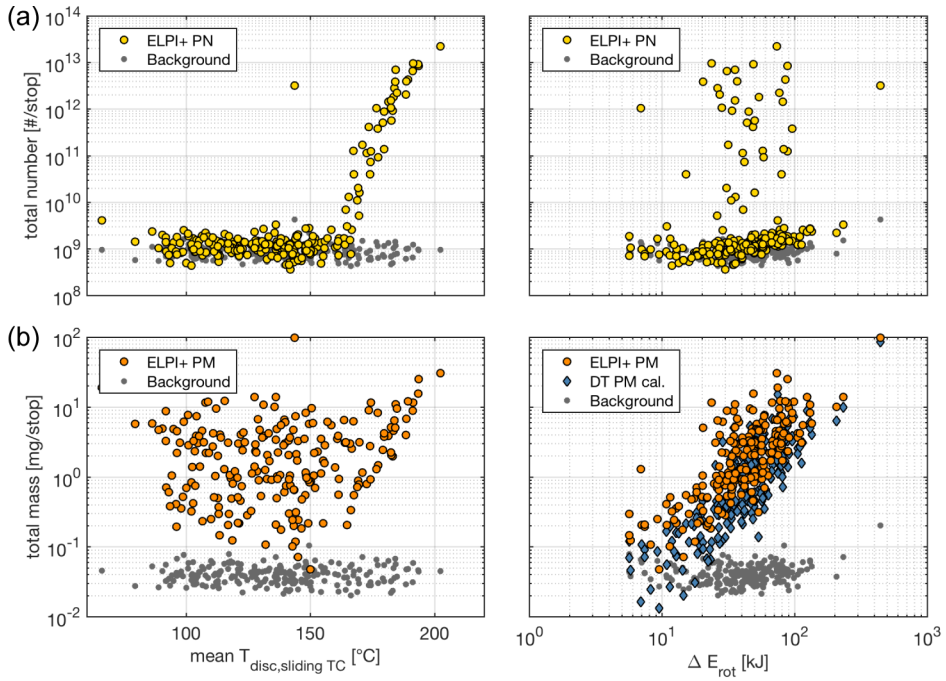

Figure 3.18 – Camparison of PN and PM emission values for each brake event obtained by ELPI+. (a) Total number and (b) total mass dependency upon $T_{\mathrm{disc,slidingTC}}$ (left) and ΔE_{rot} (right). Calibrated Dusttrak values of the corresponding measurement are shown in the lower right panel. Adapted with permission from Farwick zum Hagen et al. [92]. ©2019 American Chemical Society.

points were entirely scattered. Interestingly, the parameter dependency behaves vice versa when plotting the total particle number and particle mass values against the dissipated energy upon braking (ΔE_{rot}). Here, the particle number values were scattered and the particle mass was increasing with increasing ΔE_{rot}. The particle mass dependency was increasing with nearly the square of ΔE_{rot}. The average value was found at $0.064\,\mathrm{mg\,kJ^{-1}\,brake^{-1}}$. For the Dusttrak the mean value was smaller with $0.026\,\mathrm{mg\,kJ^{-1}\,brake^{-1}}$, which can be attributed to the different measurement techniques.

3.4.4 Brake Drag

As already mentioned, brake wear particles were also observed during driving sections when the brake was in a fully released state. Although the effect has been reported already [89], its origin was still unclear. The question remained: are the

particles generated through resuspension or by a continuous wear process of the brake itself? Addressing this, the fully run-in brake system was analyzed under "rotation only" maneuvers for different setup configurations. The test parameter can be found in table 3.3. Each velocity was hold for 180 s. Before each test was started, a static brake pressure of 10 bar was applied to the brake in order to set the brake system into same initial conditions.

Since the particle emissions were found to be mainly in the coarse and fine size

Table 3.3 – Test conditions for brake drag investigation. Rotation only procedure. Adapted with permission from Farwick zum Hagen et al. [92]. ©2019 American Chemical Society.

Order	Chamber	Caliper	Velocity [km/h]	$\bar{M}_{\mathrm{res}}$ [N m]	ΔT [K]
1	impure	w/	30, 50, 80, 100, 130, 130, 100, 80, 50, 30	7.56	5.8
2	impure	w/o	*see above*	1.76	2.3
3	clean	w/o	*see above*	1.70	5.5
4	clean	w/	*see above*	7.80	9.2

range, the APS signal was used for analysis because of its high resolution in this size range. The raw data results are presented in figure 3.19. During all tests, increasing particle number concentrations were observed for increasing rotational speeds. Obviously, the emissions of test run #1 and #4 were higher than that of run #2 and #3, which means that tests with mounted caliper led to higher emissions. However, when the caliper was not mounted, there were still particles detectable. The fact that these emissions were very similar and seemingly independent from the chamber condition (clean or impure) lead to the assumption that particle resuspension from chamber walls can be excluded. It is more likely, that these particles originated from either secondary contact plateaus, which came off the friction surface. Alternatively, they were generated by the sliding thermocouple sensor at the disc surface or the drive shaft sealing. Furthermore, small emission peaks were observed just after the acceleration phases. But the peaks were not found during deceleration. This supports the assumption of detaching particles from secondary contact plateaus.

Getting a more comparable presentation of the obtained results, the APS data were averaged over the constant velocity phases. Thereby both phases were considered, i.e., from the acceleration and deceleration ramp. The averaged total number concentration is shown in figure 3.20. Again, the continuous increase of particle number with increasing velocity can be seen. The experiments without caliper mounted

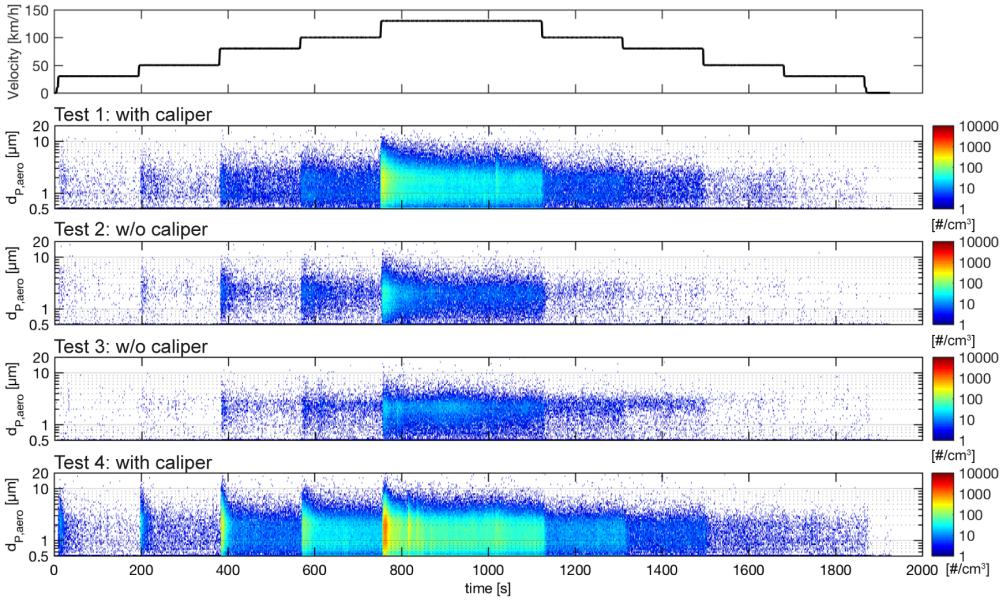

Figure 3.19 – Particle number emissions during drag investigation. Diagram order from top to bottom: Velocity profile and particle number concentration ($dN/dlogd_p$) of TSI APS depending on $d_{p,aero}$. Test order according to table 3.3.

showed the smallest concentrations. Compared with the results from the experiments with caliper mounted, their contribution was negligibly small. The increasing emissions with mounted caliper evidence the wear generation during cruising [92]. Another proof is given by the higher mean residual torque ($\bar{M}_{res}$) of the brake system. Whenever the caliper was mounted, $\bar{M}_{res}$ was found to be around 6 N m larger compared to neutral. In other words, when the caliper was mounted the brake pads dragged more on the brake disc, which also led to higher emissions. The brake drag was also accompanied by an increasing temperature difference during the tests (compare table 3.3). Interestingly, after remounting the caliper, the drag emissions were higher compared to the first run, where also the caliper was mounted. But $\bar{M}_{res}$ was only 0.3 N m larger, which is negligible from the technical point of view. Apparently, small changes of the system that can be caused by installation of the brake components influence the drag emission characteristic.

When comparing the results from the "rotation-only" maneuvers with the emissions from the acceleration and constant driving phases during the 3h-LACT cycle, the particle number concentrations during the cycle were found to be much higher as shown in figure 3.20. There were two potential reasons for this: the first one was

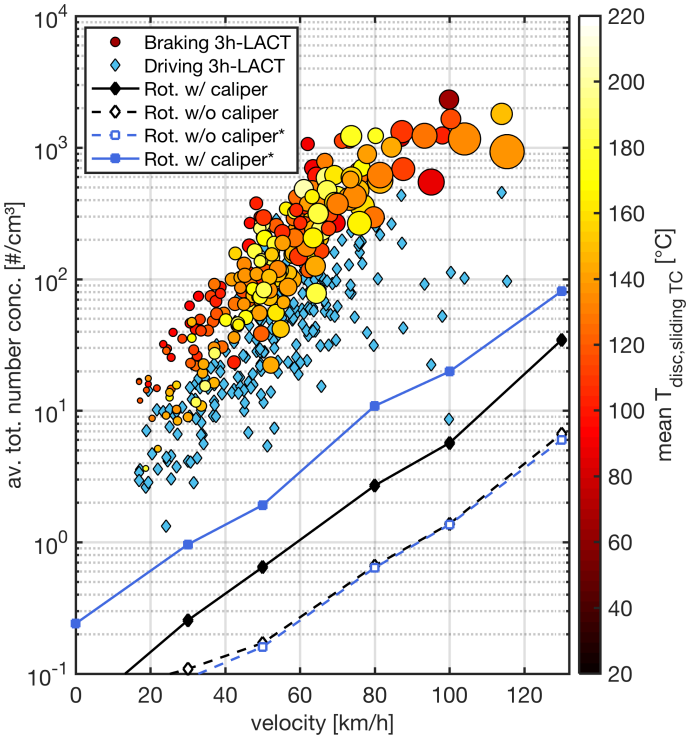

Figure 3.20 – Particle number emissions under braking and cruising conditions. Average total particle number concentration as measured with TSI APS from rotation-only cycle are plotted as lines for different configurations (*after chamber cleaning and reassembling of brake material). The averaged total particle number concentrations during the 3h-LACT cycle are shown as circles and diamonds for braking and driving events, respectively. Data are plotted against the initial velocity. The marker area size is a measure of ΔE_{rot}. Reprinted with permission from Farwick zum Hagen et al. [92]. ©2019 American Chemical Society.

the different interval lengths that were used for averaging. During the 3h-LACT cycle, the intervals were much shorter. Another reason was the preconditioning of the brake system. During the cycle, the brake also performed brake stops before each acceleration and driving phase. Thus, the pads remained closer to the disc surface as they were only retracted by the roll back mechanism of the caliper. But due to the run-out of the disc, the pads were probably further pushed apart. This may have caused additional dragging and wear. However, the particle number emissions during active braking were even higher than during cruising.

In order to estimate the emission ratio between cruising and braking events, the particle mass signal of the Dusttrak device was used: a fraction of 33.9 % of the total PM_{10} emission resulted from brake drag during a 3h-LACT cycle. Applying

the same analysis to the total particle number data led to non-meaningful results. Here, the high particle number emission peaks extended over several brake events and an appropriate separation in braking and cruising phases was not possible.

3.5 Summary

A novel setup for brake wear particle measurements on brake dynamometer was developed. The setup was designed for sensitive and loss-reduced particle emission investigations. The constant air flow of 250 m^3/h was representative for realistic driving conditions. Since the entire flow was routed to the sampling point, a high particle yield was achieved and emission quantification became possible. The setup was characterized by CFD simulations and later validated by experimental investigation. The pre-measurements fully characterized the setup regarding setup flow, sampling position and isokinetic sampling.

The focus was on investigating brake wear emissions under realistic driving conditions. Therefore, two measurement cycles were developed, namely the 3h-LACT and the WLTP cycle. Both cycles were representative for realistic driving but in direct comparison the WLTP reflected the reality better. The investigations were carried out with a 15" left front brake of a midsize passenger car. In a successive test sequence six runs of the 3h-LACT cycle were performed, whereas the last run was conducted with advanced vehicle simulations. This test included parasitic drag simulations and realistic brake temperatures. Using the same conditions, the emissions during the WLTP cycle were investigated in a final test.

The new brake material required a running-in phase until constant emission values were reached. The particle mass emissions stabilized already after the first run. For the run-in brake system, constant PM_{10} EFs in the range of 3.8-5.4 $mg\,km^{-1}\,brake^{-1}$ were obtained through gravimetric filter measurements. Deviating results were found for sensor based data, which were believed to be less representative. These results were based on either simple assumptions made for calculation or the corresponding instruments were calibrated with different aerosols. The particle mass EF of the WLTP cycle was slightly higher and values of 4.2 $mg\,km^{-1}\,brake^{-1}$ and 5.6 $mg\,km^{-1}\,brake^{-1}$ were calculated for the Dusttrak and the cascade impactor, respectively. Furthermore, separate measurements clearly evidenced the wear gen-

eration during cruising conditions, i.e., brake drag. These emissions were mainly dominated by coarse and fine particles and their contribution to the total particle mass was about 34 % for a single 3h-LACT cycle. The airborne PM_{10} fraction of brake wear was estimated to be about 40 % to 48 % of the weight loss of the brake material.

The running-in process regarding particle number emissions was seemingly not completed with the fifth run of the 3h-LACT cycle. For each cycle run, the particle number EFs were decreasing. Thus, for the fifth run an EF of about $2\times10^{12}\,\mathrm{km}^{-1}$ brake^{-1} was found. For the tests with advanced vehicle simulations, significantly lower EFs were found in range of 1-9$\times10^{10}\,\mathrm{km}^{-1}$ brake^{-1}. The high particle number emissions during the five 3h-LACT runs were mainly caused by ultrafine particle formation from vapor condensation followed by subsequent coagulation and agglomeration. Furthermore, it was believed that these particles were of volatile nature. The particles in the nucleation range were obtained only during sections with high brake temperatures. Thereby, the critical temperature was shifting from 140°C during the first run to 170°C in the fifth cycle run. This suggested an evaporation of different organic compounds in the brake lining at different onset temperatures. In case of the test with advanced vehicle simulations, all brake stops were performed below the critical temperature and consequently the obtained particle number emissions did not exceed a total number of $1\times10^{10}\,\mathrm{stop}^{-1}$ brake^{-1}.

CHAPTER 4

Brake Wear Measurements under On-Road Vehicle Operation

4.1 Measurement Setup

Measuring brake wear particles on a vehicle during on-road driving was particularly challenging since several aspects needed to be considered: the sampling apparatus including measuring instruments had to be integrated into the vehicle while preserving the entire vehicle functionality. The limited space and power capacity resulted in compromises in the setup design. Especially safety-relevant aspects were an issue. Nevertheless, the requirements for the measurement setups were high. Similarly to the dynamometer setup, the entire airborne brake wear should be aspirated and routed to the sampling point and - if possible - with minimal losses. Thus, the obtained emissions would be quantifiable. Furthermore, the car geometry near the brake and the natural air flow should be preserved as far as possible.

4.1.1 Particle Measurement Setup

Motivated by the dynamometer measurement concept, the vehicle setup was based on a constant volume system. A sampling apparatus collected the brake dust and thereupon the wear aerosol was routed to the measurement instruments for analysis. The developed system was customized for measurements at the left front brake of a midsize passenger car.

Taking into account the natural air flow at the brake, which streamed from vehicle side to outside, the brake dust was collected at the outside of the wheel. A cone-shaped collector was installed at the wheel, as it is shown in figure 4.1. Preventing any particle losses on vehicle side, additional dust shields were attached to the wheel rim and around the caliper. In this configuration the wheel itself served as original enclosure and only brake wear that escaped the wheel was collected. Since the setup collected the brake wear as a mixture with ambient air, it was categorized as semi-enclosed setup design [134, 135].

A blower at the end of the setup generated a stable air flow along the aerosol tubing. The blower capacity (stand-alone specification: 1100 Pa at 250 m^3/h) was estimated generously in order to compensate the pressure drop along the setup. Due to the negative pressure inside the setup, ambient air was sucked into the wheel rim cavity where it intermixed with the brake wear particles. The aerosol streamed through the wheel rim openings into the capturing cone. The inlay inside the capturing cone bundled the air flow and avoided dead air spaces that may have favored turbulences. The aerosol was further routed through a swivel joint. The swivel joint compensated the rotational movement of the capturing cone on one side and linked it with a stationary hose on the other side. The hose ($d_{hose,1} = 38\,mm$, $l_{hose,1} = 1.4\,m$, conductive and grounded) was routed in a soft bend ($r = 300\,mm$) onto the engine hood. In order to minimize particle losses, the tube was expanded onto a larger diameter hose ($d_{hose,2} = 100\,mm$, $l_{hose,2} = 5\,m$). The hose was routed along the vehicle diagonal in front of the windshield. It was further routed along the right A-pillar onto the vehicle roof and entered the cabin through the right rear window. In the trunk of the car, the hose was connected to a metallic sampling tubing ($d_{tube} = 100\,mm$, $l_{tube} = 0.6\,m$) that was positioned upstream of the blower. Inside the sampling tube, aerosol samples were drawn and the air velocity was measured (air velocity transducer, TSI 8455). The sampling probe was located in the center of the tube and isoaxially oriented. It was adapted for isokinetic sampling considering an estimated setup flow of about 90 m^3/h [27]. Three particle measurement devices (i.e., TSI APS, TSI EEPS, and TSI Dusttrak) were connected to the sampling probe via a flow splitter. The surplus aerosol that was not used for sampling was routed the outside of the cabin. The ambient PM_{10} concentration was monitored by a second Dusttrak device located at the left rear window.

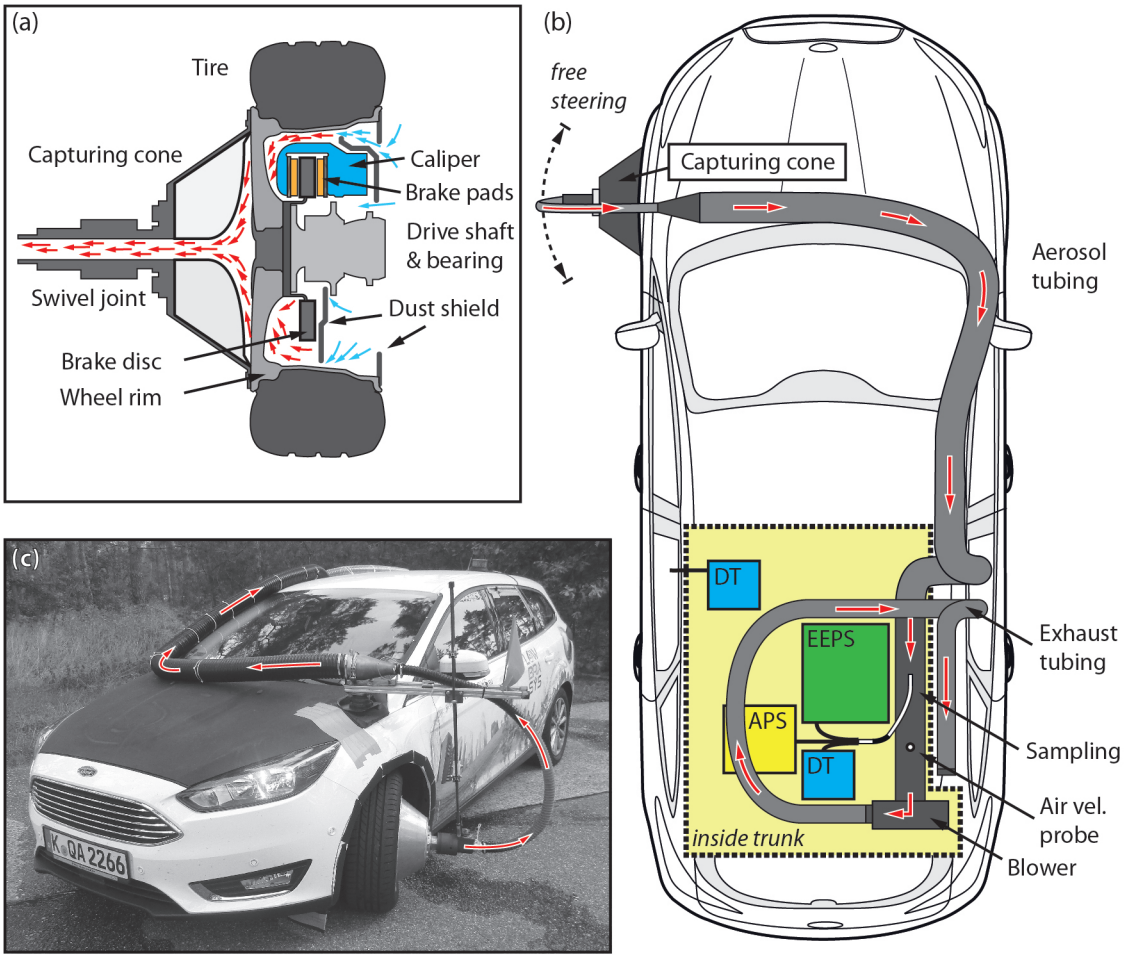

Figure 4.1 – Real-world measurement setup. (a) Dust capturing cone at left front wheel (top view). The air flow, indicated by blue (ambient) and red arrows (dust contaminated air), is forced to flow from the inside to the outside of the rim. (b) Test car with measuring setup. The yellow background area shows components that are located inside the car. The brake dust is routed from the left front wheel to the trunk (red arrows), where the measuring equipment is located. A fraction of the total aerosol is analyzed by the TSI EEPS, TSI Dusttrak, and TSI APS. The air flow is monitored by a TSI air velocity transducer. The ambient air is monitored by a second TSI Dusttrak. (c) Image of the test car. The aerosol flow is indicated by red arrows. Adapted with permission from Farwick zum Hagen et al. [134]. ©2019 Elsevier.

4.1.2 Tracer Gas Measurement Setup

Since the brake wear measurement concept was of novelty in the field of on-road driving emission measurement, its operational functionality was initially unknown. In order to gain more information about the setup characteristics - especially regarding the aspiration efficiency of the brake wear and the potential signal contamination through ambient aerosols - pre-measurements with tracer gas according to the method of Mathissen et al. [102, 136] were performed. Its principle is based on assuming similar penetration and interaction properties for particles and tracer gas. Despite the limitations of this assumption, the following advantages over investigations with artificial aerosols were identified [134]: the tracer gas i) allowed mass conservation calculations, ii) was not lost during transport, iii) could be sampled with a high sensitivity and fast response times, and iv) was not affected by contamination. In particular, the latter point was an important issue for the semi-closed setup design operating with ambient air.

The experiments were performed with a pressurized gas mixture of NO in N_2 with 10 % volume concentration. As shown in figure 4.2, the previously presented measurement setup was marginally changed. A rack mounted on the trailer hitch carried the gas cylinder. The cylinder was connected to a flow controller (MKS mass flow controller, 200 sccm/min) that regulated the flow to 100 sccm/min. In a stepwise sequence, it was programmed to switch the gas flow on and off every 20 s. The gas was routed through a Teflon hose from the back of the car to the front. There it was released at three different spots:

1. For reference, the tracer gas mixture was released directly into the aerosol tubing of the setup at position #1. The entire gas mixture was expected to be transported to the sampling point.

2. At the brake (position #2) the tracer gas was released at two different spots. Therefore, the Teflon hose was split into two lines of equal length. As it is shown on the picture in figure 4.2, the tube outlets were positioned directly at the inner and outer friction surface.

3. The release spot #3 was directly in front of the tire at the intersection to the street. This enabled an estimation of the background contribution including

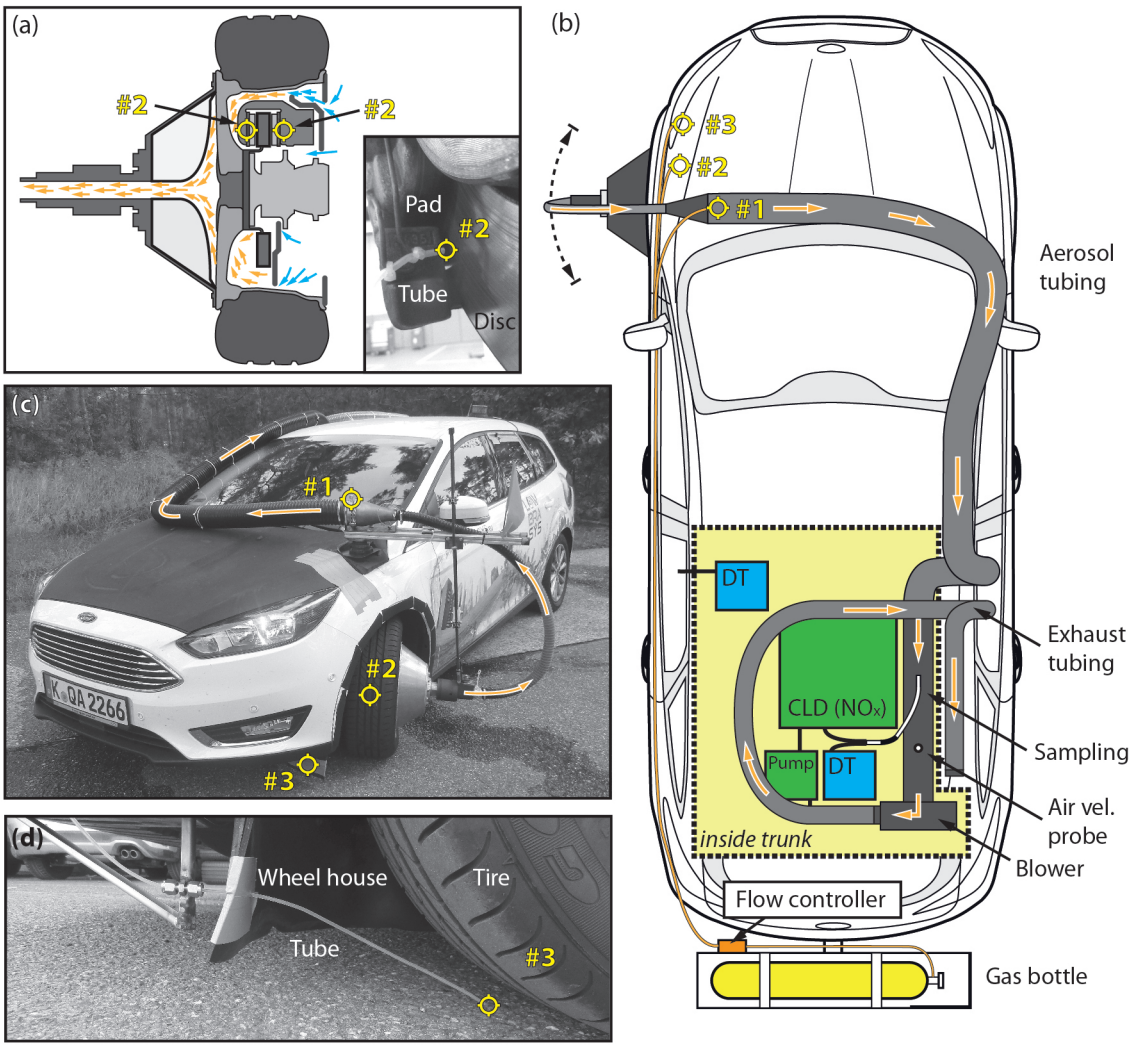

Figure 4.2 – Tracer gas setup. The NO-release spots are marked by yellow crosses, the air flow is indicated by yellow arrows. (a) Dust capturing cone at left front wheel (top view) with release spots at the brake. The image shows the outer disc side. (b) Test car with NO-bottle on trailer bar. The routing of the tracer gas hose is indicated in orange. Particle measurement devices are replaced by a NO_x-detector (ECO Physics CLD66) (c) Image of the test car. (d) Image of NO-hose located in front of the wheel for background estimation.

potential particle resuspension from the road. The tracer gas flow was set to 200 sccm/min.

The sampled tracer gas was detected by a NO/NO_2 analyzer (ECO Physics CLD 66) at the sampling point in the trunk of the car. The instrument was operated in NO_x-mode, which also considered potential reactions of the tracer gas NO to NO_2 [137]. Due to limited power capacities inside the car, it was only possible to operate either the particle measurement devices or the instruments needed for the tracer gas experiments. Thus, the tracer gas experiments were performed as separate measurements before the wear investigations were carried out.

4.2 Setup Characterization

4.2.1 Coast Down Behavior

In the real-world, cars are not only decelerated through active braking but also by naturally occurring parasitic drag, which for example includes aerodynamic or rolling resistances. These circumstances are essential for on-road vehicle measurements. However, it should be noted that in the present case the measurement setup also influenced the normal driving conditions of the car. In order to estimate its influence, the coast down behaviors of the normal vehicle and the vehicle with setup and loaded instrumentation were determined. Three test runs with two passengers were performed for each vehicle configuration, respectively.

In figure 4.3 the coast down curves are presented. The decelerations were determined for constant intervals of 10 km/h and expressed as averaged values. As one can see, both deceleration curves followed a non-linear trend and with increasing driving velocity the influence of the parasitic drag increased as well. For the normal test vehicle (i.e., without setup), Mathissen et al. [127] reported a braking energy dissipation by drag of about 15 % on average. This value was reported for the WLTP cycle. But since the WLTP is not significantly different from the 3h-LACT cycle, a similar value could be expected for the 3h-LACT cycle. In case of the fully equipped test vehicle, the decelerations caused by parasitic drag were higher. Assuming the initial velocities of the 3h-LACT cycle, an increase of 14.7±1.1 % on average was found. In other words, the particle measurement setup enhanced the parasitic drag

behavior of the test car. In conclusion, a reduction of active braking was expected because of parasitic drag, which may have led to less emissions. The effect was slightly intensified by the measurement setup.

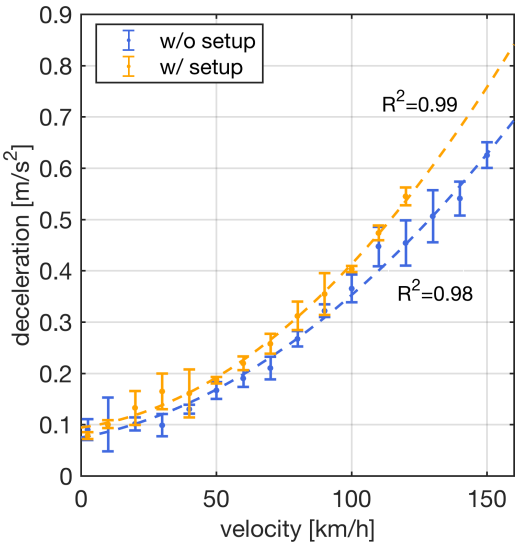

Figure 4.3 – **Coast down curves** of the test car during test drives with (yellow) and without (blue) particle measurement setup. The averaged data points were fitted with a second order polynomial fit (dashed line). The error bars refer to the standard deviation of the binned measurement data. Adapted with permission from Mathissen et al. [127].

4.2.2 Setup Air Flow and CFD Calculation

The air flow of the setup was determined during several measurements when the car was at standstill. An average value of $Q_{\text{setup}} = 76.3\,\text{m}^3/\text{h}$ was determined. This value was confirmed by a random sample survey along the entire aerosol tubing. Obviously, the blower flow capacity was reduced significantly through a pressure drop along the sampling setup.

For the moving vehicle, the air velocity decreased even further with increasing vehicle speed. The decreasing Q_{setup} trend is shown in figure 4.4. Without going into detail, two curves are shown for comparison; one was determined by the air velocity transducer and the other curve resulted from mass conservation calculations of the tracer gas measurements. Both curves were in very good agreement. They showed a nearly linear decrease of the setup flow with increasing vehicle velocity. For 50 km/h

a setup flow of around $Q_{\mathrm{setup}} = 50\,\mathrm{m}^3/\mathrm{h}$ was found. For a further increase of the vehicle velocity, the flow decreased less fast. At a vehicle speed of 100 km/h, the air flow was about 50 % of its maximal value at standstill. The air flow measurements during the dynamic 3h-LACT cycle were found to be more fluctuating. Nevertheless, on average the data was reasonably represented by the air flow curves of the initial flow measurements at constant velocities.

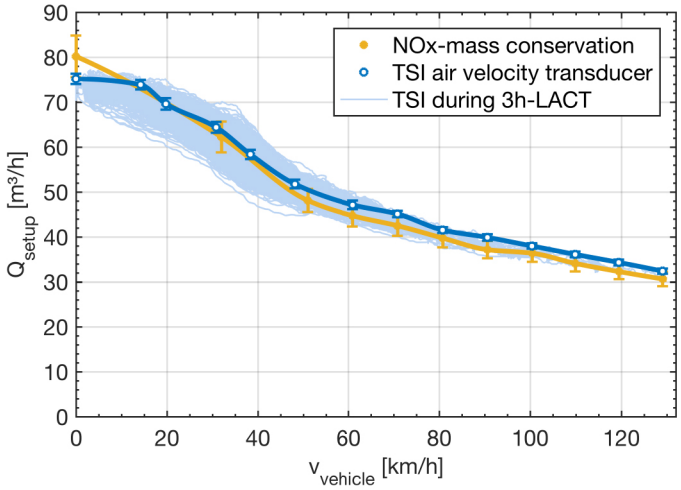

Figure 4.4 – **Setup air flow** depending on the vehicle velocity estimated through NO_x-mass conservation (yellow, data from direct NO-dosing) and air velocity transducer (blue) during constant velocity sections. Error bars refer to measurement uncertainty and the connecting lines result from interpolation using Matlab's "Piecewise Cubic Hermite Interpolating Polynomial" (pchip). The air flow during the 3h-LACT cycle is shown in light blue. Adapted with permission from Farwick zum Hagen et al. [134]. ©2019 Elsevier.

The decreasing setup flow was related to an increased pressure drop along the sampling system. Using the decreasing air flow values of the setup, CFD calculations of the air flow around the capturing cone were performed for different vehicle velocities. The resulting air velocity profiles are shown in figure 4.5. Yellow and red areas indicate air flows going from the outside in direction to the vehicle underbody. The opposite flow direction is marked by blue areas. At vehicle standstill, the air flow was predicted to be drawn homogeneously through the wheel rim. Turbulent air flows were not detectable. Thus, the resulting net flow was in the direction of the capturing cone and the entire volume was expected to be sampled. For increasing vehicle speeds, a small area inside of the wheel rim opened at the front where the

air flow penetrates into the direction of the vehicle underbody. This effect resulted most likely from air turbulences and was apparently also speed-dependent. The turbulences increased the pressure drop inside the wheel house leading to a reduced suction capacity along the entire setup. For the moving vehicle, the air flow fraction that was sucked into the capturing cone was mainly drawn from the center of the wheel rim.

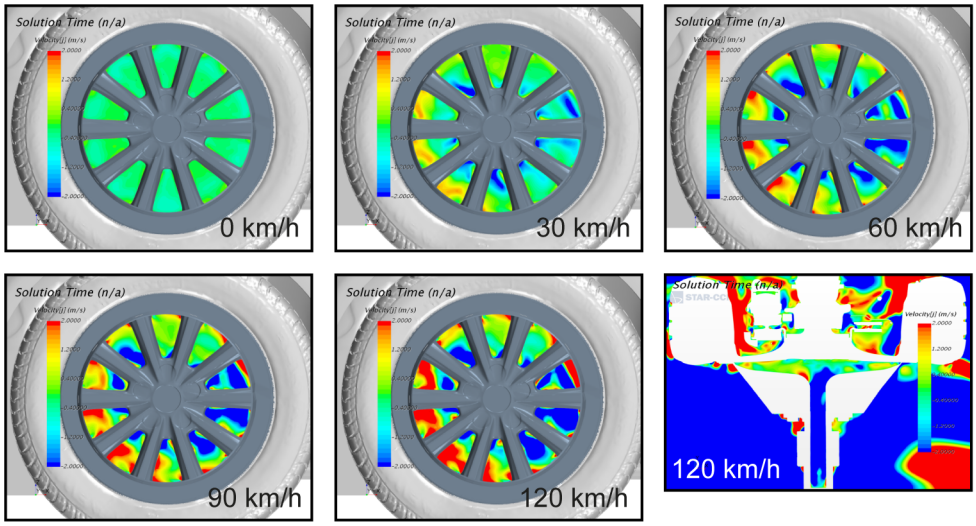

Figure 4.5 – **CFD calculation** of the left front wheel at different vehicle velocities. The air flow direction is indicated by color. Blue: air flow in the direction outside the car; red: air flow in the direction to the vehicle underbody. Side view perspective from panel 1 to 5 (for clarity the capturing cone is not shown) and top view perspective in panel 6.

In the sixth panel of figure 4.5, a longitudinal section of the air velocity profile is shown. Here the calculation indicated a rather high fraction of air volume escaping to the vehicle underbody. Note, the CFD calculations did not simulate the dust shields on the inside of the wheel rim for technical reasons. The calculations were primarily intended to reveal the origin of the decreasing setup flow. To improve the air flow behavior, dust shields were attached to the inside of the wheel rim.

4.2.3 Particle Loss Calculation

Similar to the dynamometer setup, the particle transport efficiency was estimated. For simplicity, the aerosol tubing was considered only. Using equation 3.1 under

consideration of two models for particle losses in bends (i.e., Pui et al., 1987 [120] and McFarland et al., 1997 [121]), the entire tubing was separated into sections: straight and horizontally routed tubing with $d_{tube} = 100\,mm$ and a total length of 3 m, three 90°-bends of the same tube size with radius $r = 300\,mm$, and two 90°-bends also with $r = 300\,mm$ and a tube diameter of $d_{tube} = 38\,mm$. The transport efficiency was calculated for an average setup flow of $Q_{setup} = 54\,m^3/h$ during the 3h-LACT cycle.

The $\eta_{total,trans}$ values for different particle diameters are shown in figure 4.6 together with the efficiencies dissolved for each loss mechanism. As expected from the previous calculation, the losses were size-dependent and larger sized particle were found to be lost more likely. The $\eta_{total,trans}$ values found for particles with $d_p < 1\,\mu m$ were nearly 1 and significant losses were not expected. For larger particles, $\eta_{total,trans}$ decreased sharply and its 50 % cut-off point was found at a particle size of 7-8 µm. For even larger particles it was approaching zero.

In summary, the loss calculation predicted accurate particle measurements for all the particles represented by $PM_{2.5}$. Particles in the range of $PM_{10-2.5}$ were strongly affected by particle losses and results were expected to underestimate the real particle emissions. As a final remark, losses were also caused by particle deposition on original components of the car as reported by Sanders et. al. [79]. They estimated that about 15-25 % of the PM remain on the wheel rim. Thus, losses of larger sized particles result from both, the "naturally" deposition and the "artificially" enhanced deposition inside the measurement setup.

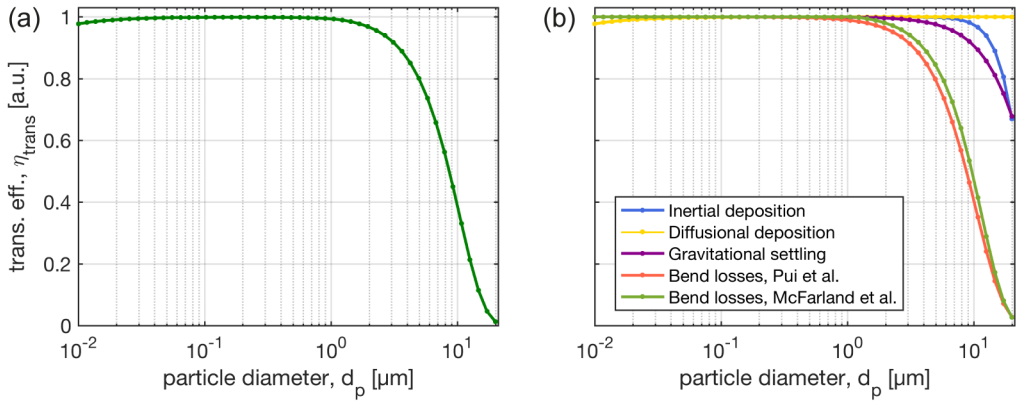

Figure 4.6 – **Estimated transport efficiency** of different sized particles within the vehicle measurement setup. In (a) the $\eta_{\text{total,trans}}$ (considering mean values between the models of losses in bends from Pui et al. [120] and McFarland et al. [121]) and in (b) the losses attributed per mechanism are shown.

4.2.4 Aspiration Efficiency

In order to investigate the aspiration efficiency, tracer gas experiments were performed. At constant driving velocities, the tracer was dosed in a sequence of 20 seconds gas release followed by a ten second pause. For each dosing position and for each velocity at least four sequences were carried out. Since cross-winds could have influenced the measurements, the order of constant velocity drives was chosen randomly. Furthermore, the measurements were repeated on different test days, where no difference in the obtained data was found.

In figure 4.7 the averaged NO_x mixing rations are plotted for the respective vehicle velocity. For the reference measurement (dosing at position #1), the ratio was almost linearly increasing with increasing driving speed. This increase could only be explained by a decreasing setup air flow, which is consistent with the previously described air flow behavior inside the setup. Since the tracer gas was assumed to be entirely sampled, the measurement was appropriate to calculate the system air flow (q_{NO_x}) by mass-conservation calculations:

$$q_{NO_x} = \frac{(c_0[NO] - c[NO_x])q_{NO}}{c[NO_x]}, \tag{4.1}$$

where $c_0[NO]$ is the tracer gas mixing ratio, $c[NO_x]$ is the measured mixing ratio, and q_{NO} is the released gas flow. As already mentioned, the results of this calculation

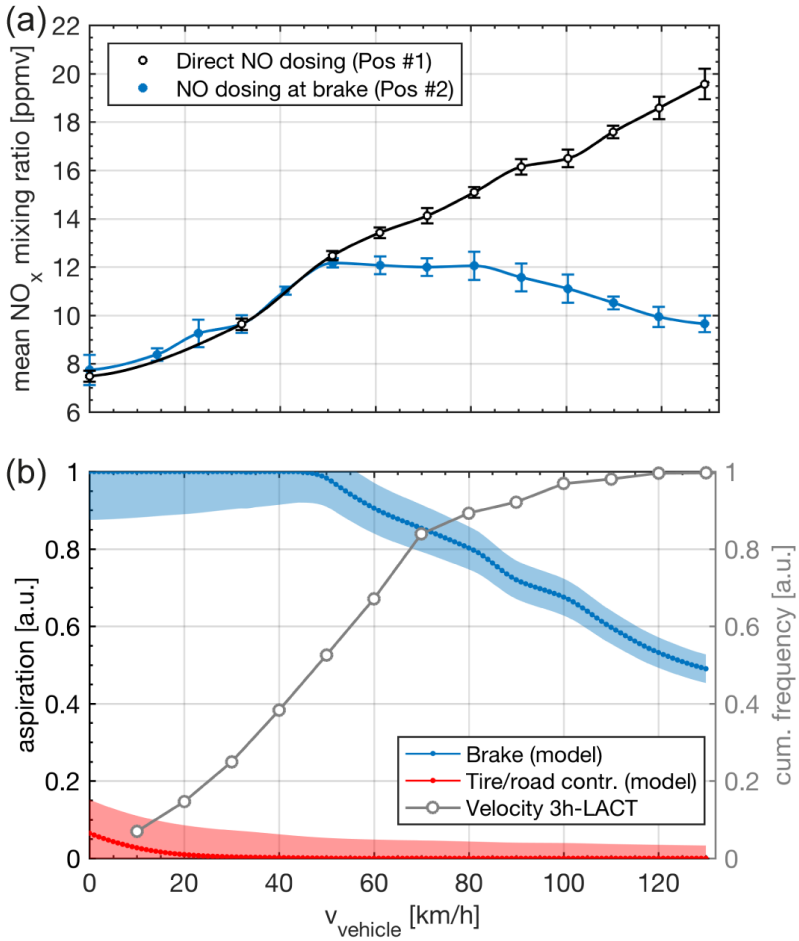

Figure 4.7 – Aspiration characteristics. (a) NO_x mixing ratios measured during NO dosing at brake (blue, pos. #2) and direct dosing (black, pos. #1). Each data point is showing the averaged mixing ratios at each constant velocity section. The error bars indicate standard deviation of the binned measured data. The line represents the data interpolation (Matlab pchip-method). (b) Calculated aspiration efficiency (blue) and tire/road contribution (red) from tracer gas experiment. The estimated error area is based on the highest error during the NO_x-measurement. For comparison, the cumulated frequencies of velocities during the 3h-LACT cycle are presented. Reprinted with permission from Farwick zum Hagen et al. [134]. ©2019 Elsevier.

were in good agreement with the air flow obtained with the air velocity transducer.

The mixing ratios obtained during the measurements where the tracer gas was released at position #2 were nearly identical for vehicle velocities of up to 50 km/h. Beyond that speed, the ratio was almost constant around 12 ppmv. For vehicle velocities of more than 80 km/h, the obtained mixing ratio decreased to absolute values of around 10 ppmv.

The deviating results from the two measurements series indicated an attenuation of the aspiration efficiency of the setup. A more precise model was obtained through data interpolation (Matlab pchip) and a subsequent division of the two measurement curves. The ratio of the two curves, i.e., the aspiration efficiency, is shown in figure 4.7 (b). For vehicle velocities up to 50 km/h the aspiration was found to be 1. In this velocity range all the airborne brake dust was expected to be collected by the setup. For higher velocities, the aspiration decreased linearly. And at vehicle speeds of 130 km/h only 50 % of airborne brake wear was expected to be sampled. However, about 90 % of the vehicle velocities in the 3h-LACT cycle were covered by an aspiration efficiency better than 0.8 and the average aspiration efficiency was found to be 0.93. Although the sampling efficiency was varying depending on the vehicle velocity, in conclusion, it was still sufficient for a realistic drive cycle such as the 3h-LACT.

Similar to the aspiration efficiency, the background contribution from the tire/road interface was analyzed. Only a small contribution of around 8 % was found for low vehicle velocities. The contribution vanished for higher vehicle speeds and thus its overall contribution was considered to be of minor relevance. This estimation was verified by additional measures on tire/road contributions, which is described in the next paragraph.

4.2.5 Tire/Road Dust Contribution

In a counter measurement, the aspiration of tire and road wear was excluded. Therefore, the setup was slightly modified with a novel dust collector behind the wheel. The opening slid of the collector faced directly the tire/road interface and its length covered the whole tire width. The aerosol tubing was disconnected from the capturing cone and attached to the novel collector. Pictures of the collector are presented in figure 4.8.

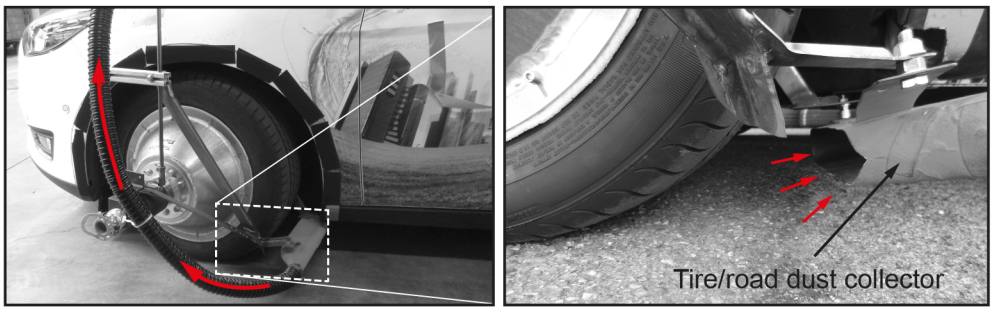

Figure 4.8 – The tire/road sampling setup with a dust collection across the full width of the tire. The red arrows indicate the flow direction.

According to Mathissen [29], ultrafine particle emissions from tire and road abrasion were expected for driving under "Extreme Cornering" maneuvers. "Extreme Cornering" was defined as curve driving with lateral accelerations of greater than $6.5\,\mathrm{m/s^2}$. In order to generate tire/road particles constantly, test drives on a circle with 18 m diameter were performed at a constant vehicle speed. At vehicle speeds of approximately 28 km/h the automatic ESP stabilized the vehicle through iterative braking. At this limit, the lateral acceleration the driving maneuver was approximately $6\,\mathrm{m/s^2}$ and close to the "Extreme Cornering" condition. As it is shown in figure 4.9, the acceleration was already sufficient for generating tire/road wear in the ultrafine size range. When using the tire/road dust collector, the development of the nucleation mode could be seen nicely. But when using the brake wear collector under the same driving conditions, there was not a single nucleation mode detected.

Although the signal contamination by tire/road dust through the brake wear sampler was never excluded completely because of the semi-open setup design, this experiment gave another indication that such contributions were of minor relevance. The results are consistent with the findings in the previous section.

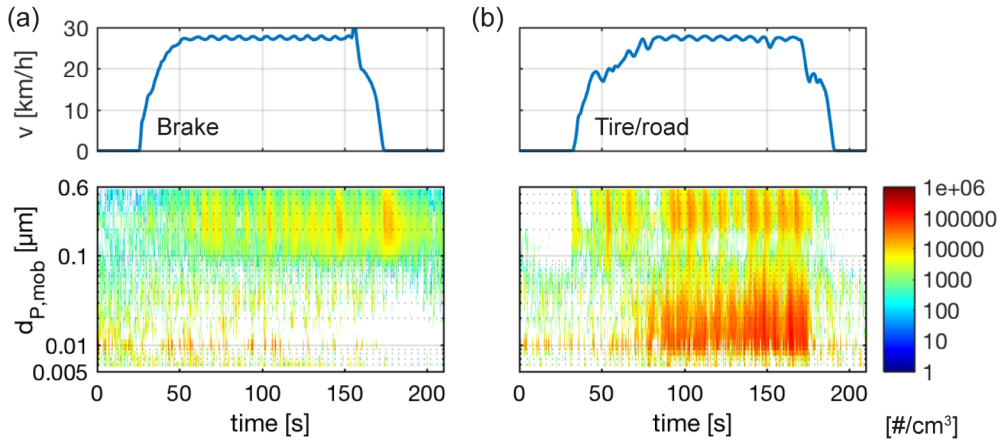

Figure 4.9 – **Cornering maneuver** at constant vehicle velocity with different sampling setups: (a) Dust sampling at brake wear collector and (b) with tire/road dust collector. Diagram order from top to bottom: vehicle velocity and TSI EEPS size distribution plots (data background subtracted).

4.3 Test Procedure

The brake wear investigations were performed with the left front brake of a midsize passenger car. The same brake system as already described in section 3.3 was used in order to generate a high comparability with the dynamometer measurements. In total, two brake materials were used: the conventional cast-iron rotor with LM brake pads and a novel friction pair. The brake rotor of the novel material was coated by an approximately 70 µm thin WC-CoCr layer. The coating was spread onto the disc by high-velocity oxygen fuel (HVOF) techniques, which gave the disc surface a very hard texture [70, 138]. The novel friction lining was composed out of geopolymers, which were based on alkaline-activated blast furnace slag [139]. Both friction linings were machined down by 2 mm and the friction pairs were run-in by five successive 3h-LACT cycles [128]. The running-in was performed on the dynamometer, which allowed a very controlled preconditioning of the material.

On both front brakes the prepared friction materials were mounted. The brake material set on the left side was used for the wear investigation and the other set on the right side of the car served as reference. For both brakes the temperatures were monitored using sliding thermocouple sensors (GA4089, Universal Therosensors LTD) with 1 N contact force. In addition to the particle and temperature

measurements, the vehicle velocity, the brake pedal use, and the brake pressure signals were recorded. The fully loaded test car including two passengers weighted 1719 kg, which corresponded to a moment of inertia of 60.9 kg m^2 for each front brake.

The test drives should reflect realistic driving behavior that could only be simulated by realistic drive cycles. But when using drive cycles, the driving profile must be reproduced accurately. Otherwise, comparisons between two tests were prevented. In order to reproduce the cycles correctly, the test car was equipped with a second set of pedals on co-driver side and a driver assistance system. The test drives were performed on an endless test track (high speed oval, Ford Lommel Proving Grounds) by two drivers. One driver was steering the car and the other one took care about the accelerations and decelerations according to the driver assistance system [134]. According to Mathissen et al. [127] the drive cycles could be reproduced in a very accurate manner. The following tests were performed:

1. **Repeatability.** In order to investigate the repeatability of the obtained emission data, a 20 minutes long subsection of the 3h-LACT was chosen as a test cycle. The cycle contained critical sections with high brake temperatures and a wide range of decelerations. Due to its short duration, several repetitions could be performed, while it was still long enough to obtain sufficient brake wear.
   Altogether eight test drives were carried out in four test sessions, whereby in each session two test drives were driven successively. The tests were performed on two test days. All tests were performed with conventional brake material that was used during real-world driving for two years. During that time, a total mileage of more than 6,000 km was accumulated.

2. **3h-LACT cycle with conventional material.** Using the prepared and run-in conventional brake material, two test drives of the 3h-LACT were made. Before each test started the brakes were tempered to around 100°C through initial braking. The emissions recorded during these brake stops were excluded from the data analysis. Note, the speed limit of the test car with mounted setup was set to 135 km/h. Thus, a single brake stop from 154 km/h was not reproduced according to the 3h-LACT cycle.

3. **3h-LACT cycle with novel material.** Similar to the previous test, also two test drives with the novel brake material were performed.

For all test drives, constant weather conditions were required. The ambient temperatures were in the range of 15-30°C and the weather was dry and windless.

4.4 Brake Wear Emissions

4.4.1 Repeatability

The driving profile of the 20 minutes repeatability cycle is shown in figure 4.10. For a better orientation, the same section is also marked in the temporal overview plot of entire 3h-LACT cycle in figure 4.11. Although the tests were supposed to start between 90°C and 100°C, for practical reasons the second test drive of each session started at slightly higher brake temperatures. This led to a temperature difference over the entire test duration. However, the temperature profiles were of similar appearance, which already indicated a robust and repeatable test procedure.

In order to evaluate the repeatability regarding wear emissions, the PM_{10}-EFs for each run were calculated. In a first step, the entire sensor based Dusttrak signals were calibrated with the corresponding mass values that were obtained by filter analysis. In a second step, the calibrated signals were extrapolated according to the actual setup flow within the measurement tube ($Q_{\text{setup},i}$). Additionally, a correction according to the actual aspiration efficiency ($\eta_{\text{asp},i}$) was performed based on the model in section 4.2.4. Thereby, absolute mass concentrations were obtained. In a final step, the concentrations were integrated over the entire test period. Initial brake events that were needed to temper the brake were excluded from the analysis. The EF-calculation can be expressed mathematically as follows:

$$\text{EF} = \sum_{i=\#\text{Samples}} c_i \cdot Q_{\text{setup},i} \cdot \eta_{\text{asp},i}^{-1} \cdot s^{-1}, \tag{4.2}$$

where c_i is the calibrated mass concentration of the i^{th}-data point and s is the driven distance. Note, the EF-calculation was based on assuming c_i, $\eta_{\text{asp},i}$, and $Q_{\text{setup},i}$ to be simultaneous. However, in practice, their signals were not time aligned because of varying particle residence times inside the setup that impede a precise correction

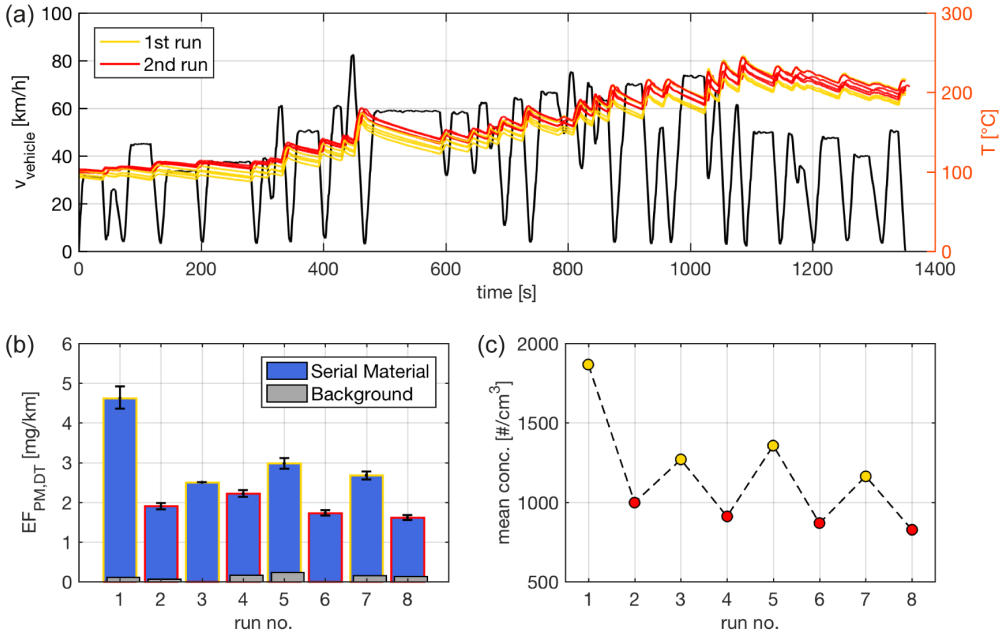

Figure 4.10 – **Repeatability measurements** during 20 min-section of the LACT cycle. (a) Velocity and temperature profiles of the eight test drives. Two runs were carried out in succession (yellow, first run; red, second run). (b) PM_{10}-EFs based on the calibrated Dusttrak signal under consideration of the actual setup flow (third data point is based on the average setup flow). The background estimation is shown in grey and the error bars refer to worst case assumptions when applying corrections regarding aspiration and setup flow. (c) The mean total particle number concentration obtained with TSI APS.

of the measured signal. Compensating this, the emission data were quantified and corrected by time-shifted $Q_{\mathrm{setup},i}$ and $\eta_{\mathrm{asp},i}$, respectively. Estimating the worst case, the maximal deviations from the calculated EFs were expressed as error bars.

The resulting PM_{10}-EFs are presented in figure 4.10 (b). With exception of the first run, the PM_{10}-EFs were found to be in the range of 1.8-2.9 mg km^{-1} brake^{-1}. The higher value during the first run was mainly related to the run-in phase of the brake after the test car was unused for several weeks. It seems possible that surface rust had formed on the disc, possibly increasing the emissions during reuse. For every following repetition of the test, the EFs were smaller and an alternating behavior between the runs was found. The same behavior was also observed for the particle number concentrations (compare the mean particle concentration of the APS in figure 4.10 (c)). So when comparing the first and second test drives for each of the four test sessions, less emissions were found during the second runs. Since

both device, i.e., Dusttrak and APS, obtained the same effect independently from each other, it was most likely that the emission characteristic was influenced by the experimental design. Either a heating up of the setup or the devices during the test or the higher brake temperatures during each of the second runs led to different emissions. Thus, it was of crucial importance to start the wear investigations under defined start conditions in order to obtain reproducible results. Brake temperatures of 100 ± 5°C with a setup assembly at ambient temperature were specified.

During the repeatability tests, the maximum brake temperatures were approaching 250°C, which was much higher than $\bar{T}_{\mathrm{crit}} = 170$°C obtained during the dynamometer measurements (compare section 3.4.3). But surprisingly, emissions in the ultrafine size range were not observed. Since the brake material was in use for more than 6,000 km, a strong history-dependency of the brake material regarding the particle number emissions is suggested.

4.4.2 Time Resolved Emissions during the 3h-LACT Cycle

The 3h-LACT cycles were reproduced in a very precise manner. The average driving distance for all four test drives was with 145.6 ± 0.8 km only marginally smaller than the ideal length of 146.2 km (compare table 4.1). The smaller driving distances were acceptable because they potentially originated from softer accelerations of the test car, which were negligible for brake wear investigations, or the omitted high speed brake stop.

In figure 4.11 a temporal overview of all particle measurement signals is given for the second test drive with the conventional brake material. The first diagram panel shows again the velocity profile and the brake temperatures. At the beginning of the test, both temperatures, i.e., on reference and on sampling side, were matching. But with continuous testing, the signals were diverging. The brake temperature on sampling side was clearly above that of the reference side. In the worst case, a maximum difference of $\Delta T = 63$ K was found. Since the brake temperature was found to be the most influential variable for the generation of ultrafine wear particles [92, 100, 133] and realistic testing was in focus of the present work, an indicator for realistic brake temperatures was designed. The indicator was placed next to the EEPS signal and it marked test sections where the brake temperature on sampling side was beyond the maximum brake temperature on reference side ($T_{\mathrm{setup}} > T_{\mathrm{ref,max}}$). For the pre-

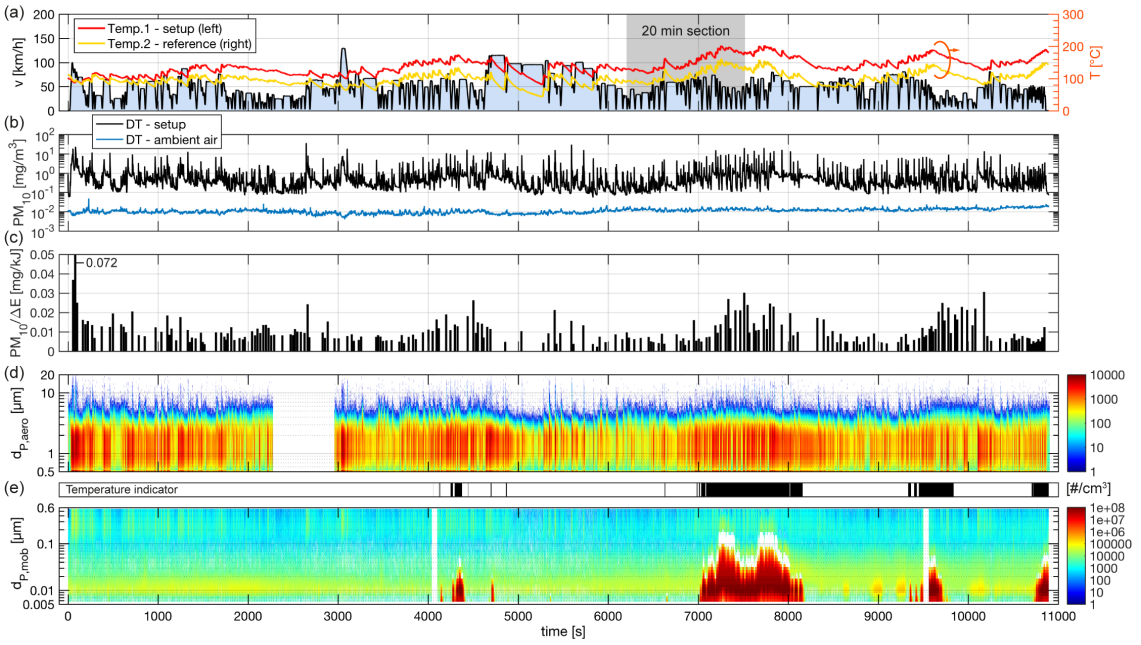

Figure 4.11 – Temporal overview plot of 3h-LACT cycle; second on-road vehicle test with conventional material. (a) Velocity profile (black, left axis; blue area, driving distance, here: 146.1 km), disc temperatures curves (right axis; red, TC at setup side; yellow, TC on reference side). (b) PM_{10} concentration of TSI Dusttrak. For reasons of clarity the raw data signal is shown only. (c) PM_{10} per dissipated energy ΔE_{kin} per brake stop. (d) Particle number concentration ($dN/dlogd_p$) of TSI APS depending on aerodynamic diameter, $d_{p,aero}$. (e) Indicator for $T_{setup} > T_{ref,max}$ (black) and particle number concentration ($dN/dlogd_p$) of TSI EEPS depending on electric mobility diameter, $d_{p,mob}$. Adapted with permission from Farwick zum Hagen et al. [134]. ©2019 Elsevier.

sented data, on reference side $T_{ref,max}$ was 162°C. The indication bar allowed a simple judgment on realistic test conditions. During all sections where T_{setup} was beyond $T_{ref,max}$, high particle concentrations in the ultrafine size range were found. A very pronounced nucleation mode was also found during the 20 min-section, at which no contribution was observed during the repeatability tests. Note, the 3h-LACT tests were performed with rather new brake materials, which were only run-in for approximately 873 km (6× 3h-LACT). Obviously, inside the friction linings were still organic compounds that evaporated at these temperatures. The facts that ultrafine emissions decreased with every cycle repetition [92] and no emissions were found for the well-used material (compare section 4.4.1) supports the assumption that ultrafine particle generation is characteristic for new material as a part of a run-in

Table 4.1 – Test parameters for each 3h-LACT cycle during the on-road vehicle measurements. The extrapolated filter load is calculated under consideration of the average setup flow. The percentages show the reduction compared to the conventional material (serial). Adapted with permission from Farwick zum Hagen et al. [134]. ©2019 Elsevier.

Material	Run no.	Driving distance [km]	PM_{10} DT filter $\Delta m_{extrapol}$ [mg]	DT drag ratio [a]	DT cal. factor	av. $PM_{10}/\Delta E_{kin}$ [$mg\,kJ^{-1}$] [a,b]
Serial	1st run	146.1	316.9	55 %	2.14	0.012 ± 0.008
Serial	2nd run	146.1	276.2	51 %	2.16	0.011 ± 0.007
Novel	1st run	145.8	249.9 (78.8 %)	38 %	2.64	0.016 ± 0.010
Novel	2nd run	144.5	210.5 (76.2 %)	41 %	2.45	0.010 ± 0.010

[a] Considering the actual setup flow and aspiration corrections.

[b] Considering DT calibration factor.

processes.

In case of fine and coarse particles, very distinct emissions modes were observed. The modes were aligned with the brake events and not linked to the nucleation modes of ultrafine particles. This again confirms the two physical and chemical origins of brake wear particles, namely abrasion and vapor condensation followed by agglomeration and coagulation [68, 100]. The modes caused by abrasion were mainly covering a size range from $d_{p,aero} = 0.6\text{-}3\,\mu m$. The signal was seeming cut-off at diameters of 4 µm to 6 µm. Larger particles were obviously lost either within the setup tubing or were deposited on the wheel rim or the brake components.

PM_{10} concentrations were found in the range of $0.1\text{-}36\,mg/m^3$. The background signal was about one magnitude higher than the ambient air particle mass concentration, which was around $0.01\,mg/m^3$. The constantly higher PM concentrations were not only related to braking but also caused by brake drag during cruising [89, 92]. Comparing the values in table 4.1 a drag ratio between 38-55 % was estimated.

Finally, it should be noted that due to the semi-open setup design a particle background concentration was present over the entire test. This may have covered minor emission peaks but in proportion, the prominent emission peaks from brake events were always detectable.

4.4.3 Cumulative Analysis and Emission Factors

A simple ranking regarding emission behavior of the two brake materials was obtained by comparing $\Delta m_{\text{extrapol}}$ for each test run (compare table 3.1). The total PM_{10} for the conventional material was 316 mg cycle^{-1} brake^{-1} and about 13 % less for the repeated run. The novel material showed a similar emission behavior between the two test drives but with about 22.5 % smaller absolute values.

A thorough analysis was made using the EFs. Particle number and PM_{10}-EFs

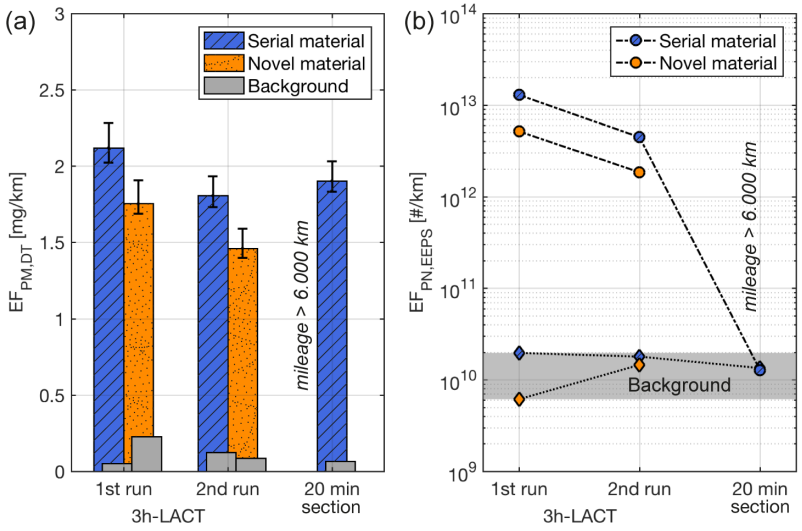

Figure 4.12 – **Emission factors** from two 3h-LACT drives with conventional (blue, dashed) and novel (orange, dotted) material compositions. Conventional material with a higher mileage ($> 6,000$ km) is shown for the critical 20 min test section. In (a) the PM_{10}-EFs (TSI Dusttrak) and the background estimations are shown. The error bars refer to worst case assumptions when applying corrections regarding aspiration and setup flow. Particle number EFs (TSI EEPS) are shown in (b) and the signal background estimation is shown as grey background. Note, the particle number EFs include volatile particles and should not be compared to regulated exhaust particle number EFs. Reprinted with permission from Farwick zum Hagen et al. [134]. © 2019 Elsevier.

were calculated in the same way as described by equation 4.2. As it is shown in figure 4.12 (a), the PM_{10}-EFs of the conventional material were in the range of 1.8-2.1 mg km^{-1} brake^{-1}. The EFs of the novel material were about 18 % smaller and in the range of 1.4-1.7 mg km^{-1} brake^{-1}. The decreasing EF-trend with cycle repetition indicates a further decrease of the EF for an even longer usage of the material. But even for the other conventional material, which was used for more than 6,000 km, a

very similar value was found. These observations are in agreement with the findings of the previous chapter. During the dynamometer measurements the PM_{10}-EFs became stable after initially higher values due to the running-in process of the material [92]. The stabilized PM_{10}-EFs of the on-road measurements were about 1/3 of those of the dynamometer. The different results were mainly related to the higher particle losses inside the vehicle setup and the "naturally" losses on the vehicle components [25]. These differences will be discussed in the next paragraph in more detail.

The particle number EFs are presented in figure 4.12 (b). For the conventional material an EF of $1.3\times10^{13}\,\mathrm{km}^{-1}$ brake^{-1} was found for the first run. With repetition it decreased by about 66 % to $4.5\times10^{12}\,\mathrm{km}^{-1}$ brake^{-1}. For the novel material the absolute values were about 60 % smaller and during the second run an EF of $1.8\times10^{12}\,\mathrm{km}^{-1}$ brake^{-1} was found. In general, the EFs were about 2-3 order of magnitudes above the background level. Note, that such high EFs resulted from high particle number concentrations in the ultrafine size range, which also include volatile particles [132]. As already mentioned, the ultrafine particles were generated through material evaporation in high brake temperature sections. Looking at the temperature indicator in figure 4.11, these sections were not representative for realistic driving as the brake temperature was artificially increased by the sampling setup. In contrast, the EF of the conventional material with 6,000 km mileage was found close to the background concentration (i.e., the detection limit of the instrument). Extending the explanation by Namgung et al. [100] for ultrafine particle formation from brakes, the evaporation process of the organic compounds inside the brake lining is believed to be final. This is consistent with the decreasing emission behavior that was obtained during the dynamometer measurements. Furthermore, it confirms the material's history-dependency regarding ultrafine particle emissions that was associated to it.

4.4.4 Emissions per Brake Stop

Similar to the analysis in section 3.4.3, the total emissions per brake stop were calculated. Here as well the data were extrapolated by the actual setup flow and corrected according to the aspiration efficiency. The total particle number per brake stop is shown in figure 4.13.

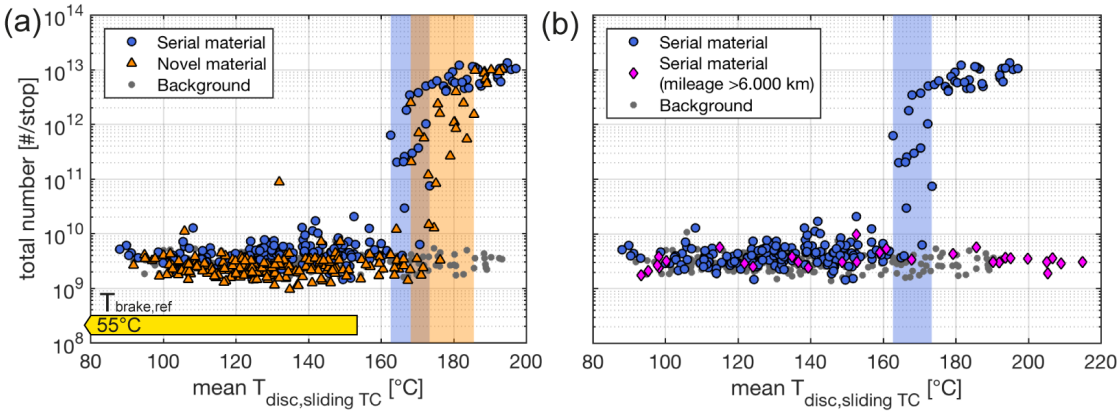

Figure 4.13 – Particle number emissions for each brake event of the second run of the 3h-LACT cycle. In (a) conventional (blue) and novel material compositions (orange) are compared. The mean brake temperature range of the non-enclosed reference brake is indicated by the yellow bar and does not exceed 153°C. Temperatures do not reach $\bar{T}_{\mathrm{crit}}$ and no ultrafine particles would be formed. In (b) the conventional material (blue) is compared with the conventional material of significantly longer driving history (magenta) during 20 min LACT section. Particle number emission increase is highlighted. The blue and orange shading indicate $\bar{T}_{\mathrm{crit}}$ at which particle number increase is occurring. Reprinted with permission from Farwick zum Hagen et al. [134]. © 2019 Elsevier.

Particle number. In analogy to the results obtained on the dynamometer, the emissions were nearly constant for brake temperatures below $\bar{T}_{\mathrm{crit}}$. The constant emission values were again close to the background level, which was in the range of 1-10$\times 10^{9}$ stop^{-1} brake^{-1}. At $\bar{T}_{\mathrm{crit}}$ a steep increase of the emission values was observed to up to 1×10^{13} stop^{-1} brake^{-1}, which was reaching the detection limit of the instrument. The $\bar{T}_{\mathrm{crit}}$ values were found at 168°C and 178°C for the conventional and novel material, respectively. The different values suggest that $\bar{T}_{\mathrm{crit}}$ is a material specific quantity. The higher $\bar{T}_{\mathrm{crit}}$ of the novel material led also to the lower EFs

over the entire cycle. The yellow bar indicates the mean brake temperature of the reference brake. During the 3h-LACT the maximal temperature was found at 153°C, which was clearly below $\bar{T}_{\mathrm{crit}}$. Thus, for realistic driving the brake temperature stayed below $\bar{T}_{\mathrm{crit}}$ and consequently ultrafine particle emissions were not expected. For the measurements with the used conventional material, the $\bar{T}_{\mathrm{crit}}$ could not be determined although the test were performed at even higher brake temperatures.

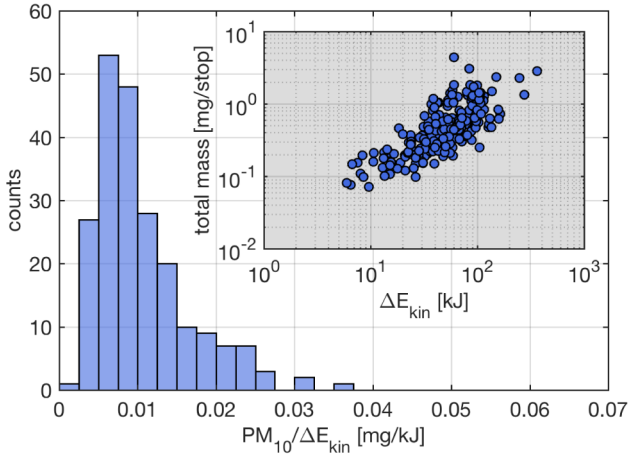

Figure 4.14 – PM$_{10}$ per dissipated energy ΔE_{kin} for each brake stop (conventional material, second 3h-LACT run). The TSI Dusttrak data is calibrated and corrected regarding actual setup flow and aspiration efficiency. Reprinted with permission from Farwick zum Hagen et al. [134]. ©2019 Elsevier.

Particle mass. The total particle mass per brake stop was set into relation to the dissipated energy ΔE_{kin}. The energy difference was roughly estimated by using the initial and final velocities of each brake event and assuming a wheel load of 615.8 kg at the front axis.

The total PM$_{10}$ per brake stop is plotted versus ΔE_{kin} in the inset of figure 4.14 (compare also figure 4.11). The values varied over a wide span from 0.0024 mg kJ^{-1} brake^{-1} to 0.0725 mg kJ^{-1} brake^{-1}, but as the histogram shows, the majority of data point was found around 0.01 mg kJ^{-1} brake^{-1}. The average value was very similar and independent from the friction material (compare table 4.1). Compared to the dynamometer measurements, the actual values were about 60 % smaller. The deviating results will be discussed in the next chapter.

4.5 Summary

Investigating brake wear particles on-road, a novel measurement setup was developed, installed, and tested on road with a midsize passenger vehicle under realistic driving conditions. The semi-closed setup design conserved the natural air flow direction at the brake, while sampling brake wear at the outside of the wheel rim. A cone-shaped collector at the wheel rim aimed the full aspiration of the generated brake wear. The brake aerosol was routed from the collector to the trunk of the car, where the measurement devices were located.

The setup was characterized by particle loss calculations, which revealed high transport efficiencies for $PM_{2.5}$. Larger sized particles were found to be more susceptible for getting lost. These particles were additionally expected to be deposited on vehicle components.

Furthermore, the setup was experimentally characterized regarding air flow, aspiration efficiency, and signal contamination through background sampling. The air flow was found to be velocity-dependent with a decreasing air flow for an increasing vehicle velocity. This influenced the aspiration efficiency of the dust collector as well. While the entire airborne brake wear fraction was expected to be sampled for vehicle speeds up to 50 km/h, for higher speeds the aspiration efficiency decreased. But since most brake stops of the driven 3h-LACT cycle occurred at lower vehicle velocities, an average aspiration of 93 % could be expected. A contamination of the measured signal through background particle concentrations (e.g., tire/road wear) was excluded as its contribution was found to be negligibly small.

Although compromises regarding aspiration, setup flow, and particle losses were made, the measured signals were of high accuracy. Using the 3h-LACT cycle, two test drives with two different brake materials were performed. In case of particle number emissions, EFs of $4.5\times10^{12}\,\mathrm{km^{-1}}$ brake^{-1} and $1.8\times10^{12}\,\mathrm{km^{-1}}$ brake^{-1} were found for the conventional and novel (WC-CoCr coated disc and friction lining with geopolymers) brake materials, respectively. The high EFs originated from ultrafine particle generation at high brake temperatures. The particles were believed to be of volatile nature. Since the setup design limited the brake cooling, the obtained brake temperatures were artificially increased. For normal brake cooling the brake temperature stayed below $\bar{T}_{\mathrm{crit}} = 178°\mathrm{C}$, which indicated that during realistic on-

road driving with the present material, no ultrafine particle emissions are expected. Furthermore, the particle number emissions were found to be history-dependent. Used friction material with more than 6,000 km mileage did not show any particle emissions in the ultrafine size range. This suggested a final evaporation of organic compounds inside the friction lining.

The obtained PM_{10}-EFs were found to be in the range of 1.4-2.1 mg km^{-1} $brake^{-1}$. It was found that the new material emitted about 18 % less. Independently of the material composition, the PM_{10} emission per dissipated energy was found to be about 0.01 mg kJ^{-1} $brake^{-1}$.

CHAPTER 5

Results in Literature Context and Discussion

Both of the presented measurement approaches, either for the laboratory or the vehicle on-road tests, were capable for repeatable and robust brake wear measurements. The test data were used to calculate characteristic wear parameters, such as EFs, brake drag contributions, and PM_{10} per dissipated brake energy. Attention was given on conducting the tests in a very comparable manner: this included tests with the same brake material, similar preconditioning, and the same drive cycles. Furthermore, both setups were based on similar measurement concepts. However, not all of the obtained wear parameters were closely matching. The wear parameters and potential deviations will be discussed in this chapter. In addition, a classification into the literature context is made.

Ultrafine particles at high T_{brake}. One of the findings was the increased particle number emission with increasing brake temperature. While at low brake temperatures stable emissions were found, at $\bar{T}_{\mathrm{crit}}$ a rapid increase of ultrafine particles was observed. Independently of the measurement approach, for the conventional brake material the $\bar{T}_{\mathrm{crit}}$ was found at about 170-178°C [92, 134]. These observations were already indicated by Garg et al. [24]. For different brakes, they found different $\bar{T}_{\mathrm{crit}}$ values. The physical mechanism of this effect was described by Namgung et al. [100], who concluded particle formation through an evaporation process followed by condensation and agglomeration. Alemani et al. [133] reported similar observations from a pin-on-disc investigation. However, none of these studies simulated realistic

driving conditions. It was not clear, whether or not ultrafine emissions occur during real-world driving. The present study gave clear evidence that for realistic driving the brake temperatures stayed below $\bar{T}_{\mathrm{crit}}$ and consequently ultrafine emissions were not expected. Furthermore, in the present study, a shift of $\bar{T}_{\mathrm{crit}}$ to higher temperatures was found for every cycle repetition. The fact that during the vehicle tests with the used brake material ($> 6,000$ km mileage) not any ultrafine particle mode was observed, supports this hypothesis. Thus, it is concluded that ultrafine emissions strongly depend on the material history. Since the lifetime of conventional brake material is much greater than 6,000 km and the fact that realistic driving generates temperatures below $\bar{T}_{\mathrm{crit}}$, it is believed that ultrafine particle generation during braking is very unlikely for normal driving.

Table 5.1 – **Emission factors** for light duty vehicles sorted according to the type of study. In some cases, the EFs were recalculated in order to match comparable units.

Reference	Type of study	Particle mass [mg km^{-1} veh^{-1}]	Particle number [km^{-1} brake^{-1}]
Garg et al. 2000 [24]	Dynamometer	2.9-7.5	[a] 1×10^{4}-5.2×10^{6} [a] 7×10^{10}-4.7×10^{12}
Sanders et al. 2003 [79]	Dynamometer	1.5-8.1	-
Iijima et al. 2008 [82]	Dynamometer	[a] 5.8	-
Perricone et al. 2016 [90]	Dynamometer	[a,b] 41.1-105.6 (LM) [a,b] 27.6 (NAO)	[a] $8\text{-}91\times10^{10}$ [a] 1.5×10^{12}
Hagino et al. 2016 [89]	Dynamometer	0.04-1.4	-
Farwick zum Hagen et al. 2019 [92]	Dynamometer	[b] 13.5 (3h-LACT) [b] 12.2-16.8 (WLTP)	$1\text{-}9\times10^{10}$ (3h-LACT) $1\text{-}2\times10^{10}$ (WLTP)
Farwick zum Hagen et al. 2019 [134]	Vehicle on-road	[b] 5.4 (3h-LACT)	4.5×10^{12} (3h-LACT) (note: $T_{\mathrm{setup}} > T_{\mathrm{ref}}$)
Rauterberg-Wulff 1999 [115]	Receptor model	1 (highway-tunnel)	-
Abu-Allaban et al. 2003 [106]	Receptor model	0-12 (average)	-
Luhana et al. 2004 [116]	Receptor model	6.9 (tunnel)	-
Bukowiecki et al. 2010 [17]	Receptor model	8±4 (urban street) 1.6±1.1 (highway)	-
Gietl et al. 2010 [68]	Receptor model	10.7	-
Hulskotte et al. 2014 [140]	Receptor model	8-15	-

[a] Converted to same units by assuming 1 brake stop for 1 km driving distance

[b] Converted to vehicle based EFs by multiplying with factor 3

Emission factors. The EF results of both measurement approaches are summarized in table 5.1 together with the findings of other studies. In case of the dynamometer results of the present study, the data from the tests conducted with advanced vehicle simulations were presented because they were more representative for realistic driving. This allowed a better comparability with data from the on-road vehicle investigation. Since most of the literature EFs related to particle mass were given as vehicle based EFs, the PM_{10}-EFs reported earlier were converted. Assuming a brake power distribution between front and rear brakes of about 70:30, a multiplication of the EF by factor 3, was assumed to be an appropriate choice for projection.

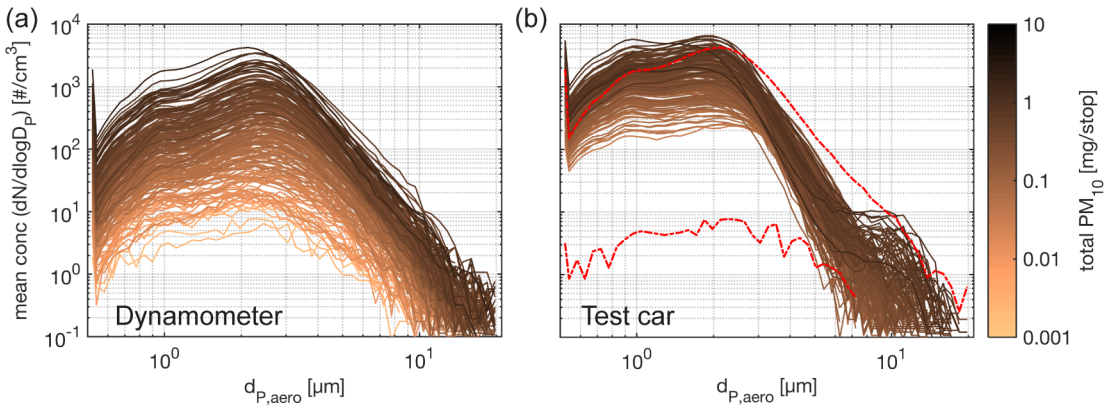

Figure 5.1 – Correlation of total PM_{10} and particle number size distributions for (a) dynamometer and (b) test car measurements. The data is obtained by TSI APS (averaged particle number size distributions) and TSI DT (total PM_{10}). A separate curve is plotted for each brake event of the 3h-LACT cycle. The red lines in (b) show the distributions obtained on the dynamometer for minimal and maximal PM_{10} values.

The PM_{10}-EFs of the 3h-LACT cycle were found to be different between the two measurement approaches: EFs of 13.5 mg km^{-1} veh^{-1} and 5.4 mg km^{-1} veh^{-1} were found for the laboratory and the on-road vehicle investigation, respectively [92, 134]. The smaller EF obtained during the on-road vehicle tests was caused by higher particle losses inside the vehicle measurement setup. The particle loss calculation predicted significant losses for particles larger than 7 µm. Whereas on the dynamometer, lower particle losses were predicted. These empirical calculations were confirmed by the experimental data. In figure 5.1 the mean number distribution is compared to the total PM_{10} for every brake event. On the dynamometer

the particle number size distributions seemed to be equally distributed for all PM_{10} values. On the test vehicle a similar correlation was found only for particles smaller than 2-3 µm. But for larger sized particles, the shape of the distribution varied: for particles larger than 2-3 µm the number concentration fell significantly. In this range, almost all curves were found on top of each other. This evidenced higher losses of coarse particles during the on-road measurements as a result of either limited transport efficiencies inside the setup or the deposition of particles on vehicle sites [25]. Furthermore, the smaller vehicle EFs originated also from the increased coast-down behavior of the fully equipped test car. Although parasitic drag was simulated on the dynamometer as well, the pre-measurements with the modified test car showed an even higher natural deceleration. In conclusion, the dynamometer EF appears to be most reliable because it was less affected by the setup instrumentation. However, the on-road EF was of similar order of magnitude and thus it served as a reasonable proof of the laboratory investigations.

Comparing the EFs with the values reported in literature, very contradictory results were found. Most of the reported EFs were of smaller values in the range of about 2-8 mg km^{-1} veh^{-1}. It is easy to understand that in case of receptor modeling the EFs depend strongly on the measurement site. But in case of direct measurements, i.e., on dynamometers, some studies also report very small EFs of only $\approx$1.5 mg km^{-1} veh^{-1}. However, these values were related to different pad materials that were tested. For example, Sanders et al. [79] reported less PM emissions for NAO pads. The highest emission rates were found for LM pad compositions. Similarly, Hagino et al. [89] reported very small EFs. Their investigations were most likely performed with NAO pads as well. But in addition, their sampling efficiency of the setup is unknown. Since only very small airborne fractions were reported, a small particle yield might be a potential reason for lower EFs. In contrast, Perricone et al. [90] found significantly higher EFs. These results were mainly influenced by the static test cycle that included besides moderate braking also more severe deceleration with 0.4 g. Obviously, the measurement setups as well as the conducted drive cycles influence the EFs significantly. In comparison, the reported EFs of the present work are still in the midfield of the reported values.

In case of particle number, very different EFs were reported. These results were obtained exclusively by direct measurements. Considering all EFs that were referring to the entire particle size range (from nano- to several micrometer), values in

range of $1\times10^{10}\,\mathrm{km^{-1}\,brake^{-1}}$ to $4.7\times10^{12}\,\mathrm{km^{-1}\,brake^{-1}}$ were reported. As already described earlier, these values were strongly influenced by the effect of ultrafine particle formation at high brake temperatures. Since both of the reporting literature studies (see table 5.1) performed the measurements under artificial test cycles, it is assumed that the brake temperature was also artificially increased during the tests. Thus, for realistic test drives - as they were performed within the present work - much lower brake temperatures are expected and consequently the EFs would be much smaller.

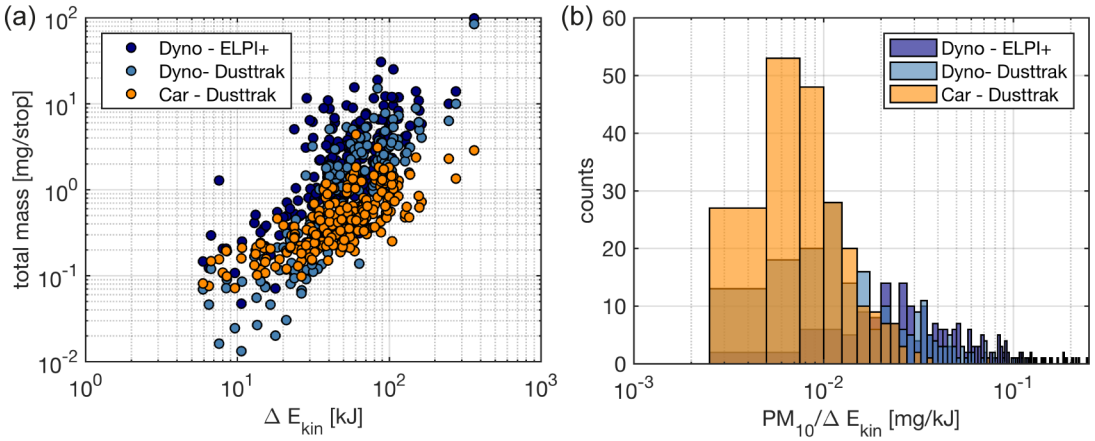

Figure 5.2 – Comparison of dynamometer and test car measurements. (a) PM_{10} per dissipated energy ΔE_{kin} for each brake stop and (b) shows the histogram.

PM_{10} per dissipated energy. Another important emission parameter is the emission rate in terms of PM_{10} per ΔE_{kin}. The results of the different measurement approaches are shown in figure 5.2. Considering the Dusttrak device, mean emission parameters of $0.026\,\mathrm{mg\,kJ^{-1}\,brake^{-1}}$ and $0.01\,\mathrm{mg\,kJ^{-1}\,brake^{-1}}$ were found for the dynamometer and the on-road vehicle investigation, respectively [92, 134]. Compared to the dynamometer, the vehicle values were about 60 % smaller, which was due to higher particle losses inside the on-road measurement setup and the rather simple estimation of the dissipated energy. For the on-road investigation, the ΔE_{kin} were overestimated as they excluded any parasitic drag effects (compare section 4.2.1). In consequence, the resulting emission rate, PM_{10} per ΔE_{kin}, became smaller. For the dynamometer measurements, the values were expressed more ac-

curately since the brake dissipated the entire rotational energy, which was also used within the calculation.
In conclusion, it is recommended to use the dynamometer results for calculating vehicle based emission rates. Assuming a multiplication by factor 3 when converting from brake to vehicle units, an emission rate of about $0.08\,\mathrm{mg\,kJ^{-1}veh^{-1}}$ is expected. This emission rate is only marginally smaller than the recently used value of $0.1\,\mathrm{mg\,kJ^{-1}veh^{-1}}$ in an emission inventory study by Ricardo [141].

Brake drag. Particle emission during cruising was already reported in literature [81]. Hagino et al. [88] reported this effect initially and reported different brake drag contributions ranging from 22-56 % depending on the brake maneuver. They interpreted these emissions as particle release from the disc and pad surface during the acceleration phase. Perricone et al. [90] also observed particle emissions during acceleration phases and spoke of "particle showers". The present work gave further insight into this effect: particles were not only released from the pad and disc surface but rather generated through a continuous dragging of the pads at the disc surface [92]. For the 3h-LACT cycle a brake drag contribution of 34 % and 51 % were found for the laboratory and on-road investigation, respectively [92, 134]. The higher drag contribution during the vehicle test may originated from the higher background contribution. The results are consistent with literature.

CHAPTER 6

Summary and Conclusion

Brake wear contributes considerably to traffic related PM. Besides tire wear and road abrasion, brake wear emissions are expected to increase in the near future because of a rising demand for mobility, growing vehicle fleets, and missing legislation for non-exhaust vehicle emissions. As PM emissions are usually associated with health concerns, brake wear is also taken seriously. Thus, in recent years, a lot of research addressed brake wear emissions: measurement setups were developed and important findings on the emission behavior were revealed. However, the investigation of brake wear particles under realistic driving conditions remained unattended. Characteristic emission parameters, such as EFs or emission rates representative for on-road driving, were unknown.

The present work focused on investigating brake wear emissions under realistic test conditions in order to obtain results representative for real-world driving. The investigations were carried out on the basis of a midsize passenger car that was assumed to reflect a widely-used vehicle type in Europe. Two novel measurement setups were developed: one for a brake dynamometer in the laboratory and the other one for vehicle measurements on-road. The measurement concept of both setups was similar, namely that airborne brake dust was drawn from the brake to the sampling point as a whole. This enabled a proper emission quantification. In the laboratory, the brake was enclosed by a chamber and the air flow was kept constant during the entire test. A rather low air flow of $250\,\mathrm{m^3/h}$ allowed measurements with a high signal sensitivity. The used air was initially filtered, which suppressed the

background contribution. The setup design was characterized by CFD simulations in order to find optimal air flow conditions. Particle loss calculations predicted high particle transport efficiencies for nearly all particle sizes. In case of the vehicle setup, the wheel rim served as chamber as it was used as an original enclosure around the brake. The dust was collected through a cone-shaped sampler at the outside of the wheel by which the natural air flow direction at the brake was conserved. For practical reasons, this setup drew samples from ambient air so that a minor background contribution was always present. By means of tracer gas experiments, a variation of the sampling efficiency and a reduction of the setup air flow with increasing vehicle velocity was found. The decreasing setup air flow led to an insufficient brake cooling that artificially raised the brake temperatures. Although the vehicle measurement setup revealed limitations regarding sampling efficiency, particle transport efficiency, and brake cooling, its measurements served well for validating the results obtained on the dynamometer.

The brake wear investigations were performed under real-world driving maneuvers. Two test cycles were chosen, namely the 3h-LACT cycle and the WLTP cycle. On the dynamometer both cycles were driven, while some of the tests were performed under even more realistic vehicle simulations. This included the simulation of realistic brake temperatures and parasitic drag. For the vehicle tests, the 3h-LACT cycle was used as driving profile.

One of the main findings, which was obtained with both measurement approaches, was the generation of ultrafine particles at macroscopic brake temperatures beyond approximately 175°C. At this temperature, an evaporation process of organic compounds in the pad linings is assumed. The ultrafine particles resulted from condensation and agglomeration of vapor. Since the $\bar{T}_{\mathrm{crit}}$ was shifting to higher temperatures with every cycle repetition, it is believed that for different compounds different evaporation onset temperatures exists. The effect is believed to be final because brake material with high mileage was not emitting ultrafine particles at all. Thus, the emission of ultrafine particles from brakes is believed to be a material specific characteristic that depends strongly on the driving history. Furthermore, for realistic driving, the brake temperatures remained below $\bar{T}_{\mathrm{crit}}$ and in consequence, ultrafine particle generation did not occur. Thus, ultrafine particle formation is assumed to be very unlikely during realistic driving.

PM_{10}-EFs were estimated to be 4.5 mg km^{-1} brake^{-1}, which seems to be a reason-

able result for LM content brake pads compared to literature. The corresponding mean emission rate was found to be $0.026\,\mathrm{mg\,kJ^{-1}\,brake^{-1}}$. Depending on the measurement technique applied, this value might be higher. In terms of particle number, the EFs were in the range of 1-9$\times 10^{10}\,\mathrm{km^{-1}\ brake^{-1}}$. In case of artificially increased brake temperatures beyond $\bar{T}_{\mathrm{crit}}$, the EFs were found to be at least two orders of magnitude higher.

Separate measurements gave further insight into the effect of particle emissions during cruising. The tests evidenced particle generation through abrasion due a permanent contact of the brake pads with the rotating disc. During the 3h-LACT a brake drag contribution of 34 % was found for the dynamometer tests.

As a conclusion, the present work presents innovative methodologies for brake wear measurements and reveals realistic emission parameters of a conventional car brake. Two measurement approaches were presented, but as a recommendation, brake wear particle measurements should be performed on brake dynamometers. This allowed tests with less technical restrictions, higher test-to-test reproducibility and robustness, and better cost efficiency. However, the on-road vehicle measurements served as meaningful verification of the laboratory results. Further on-road test should be carried out in order to gain more information for vehicle simulations in the laboratory - especially regarding brake temperature. The presented measurement setups and procedures may serve as orientation for future work.

Bibliography

[1] D. A. Lashof and D. R. Ahuja. *Relative contributions of greenhouse gas emissions to global warming.* Nature, 344, 6266, pp. 529–531, 1990.

[2] T. R. Karl and K. E. Trenberth. *Modern global climate change.* Science, 302, 5651, pp. 1719–1723, 2003.

[3] T. Adhanom Ghebreyesus. *Opening address at the first WHO global conference on air pollution and health.* `https://www.who.int/dg/speeches/2018/conference-on-air-pollution/en/`, 2018. [Online; accessed 04-June-2019].

[4] World Health Organization. *Ambient air pollution: Health impacts.* `https://www.who.int/airpollution/ambient/health-impacts/en/`, 2019. [Online; accessed 04-June-2019].

[5] European Envirnment Agency. *Environment and human health.* Report, 2013.

[6] European Committee for Standardization. *EN 481:1993. Size fraction definitions for measurement of airborne particles.* Official Journal of the European Union, 1993.

[7] A. Valavanidis, K. Fiotakis, and T. Vlachogianni. *Airborne particulate matter and human health: Toxicological assessment and importance of size and composition of particles for oxidative damage and carcinogenic mechanisms.* Journal of Environmental Science and Health, Part C: Environmental Carcinogenesis and Ecotoxicology Reviews, 26, 4, pp. 339–362, 2008.

[8] F. Dominici, R. D. Peng, M. L. Bell, L. Pham, A. McDermott, S. L. Zeger, and J. M. Samet. *Fine particulate air pollution and hospital admission for*

cardiovascular and respiratory diseases. JAMA, the Journal of the American Medical Association, 295, 10, pp. 1127–1134, 2006.

[9] K. H. Kim, E. Kabir, and S. Kabir. *A review on the human health impact of airborne particulate matter*. Environment International, 74, pp. 136–143, 2015.

[10] J. Schwartz. *Particulate air pollution and chronic respiratory disease*. Environmental Research, 62, 1, pp. 7–13, 1993.

[11] C. A. Pope III., R. T. Burnett, M. J. Thun, E. E. Calle, D. Krewski, K. Ito, and G. D. Thurston. *Lung cancer, cardiopulmonary mortality, and long-term exposure to fine particulate air pollution*. JAMA, the Journal of the American Medical Association, 287, 9, pp. 1132–1141, 2002.

[12] European Envirnment Agency. *Air quality in Europe - 2015 report*. Report, 2015.

[13] The European Parliament and the Council of the European Union. *Directive 2008/50/ec*. Official Journal of the European Union, 2008.

[14] World Health Organization. *Air quality guidelines. Global update 2005*. Report, 2005.

[15] M. Tista, M. Gager, S. Haider, I. Pucher, and B. Ullrich. *European Union emission inventory report 1990-2016 under the UNECE convention on long-range transboundary air pollution (LRTAP)*. Report 1977-8449, European Environment Agency, 2018.

[16] D. Wakeling, T. Murrels, D. Carslaw, J. Norris, and L. Jones. *The contribution of brake wear emissions to particulate matter in ambient air*. FAT-Report, 2017.

[17] N. Bukowiecki, P. Lienemann, M. Hill, M. Furger, A. Richard, F. Amato, A. S. H. Prévôt, U. Baltensperger, B. Buchmann, and R. Gehrig. *PM10 emission factors for non-exhaust particles generated by road traffic in an urban street canyon and along a freeway in Switzerland*. Atmospheric Environment, 44, 19, pp. 2330–2340, 2010.

[18] R. M. Harrison, A. M. Jones, J. Gietl, J. Yin, and D. C. Green. *Estimation of the contributions of brake dust, tire wear, and resuspension to nonexhaust traffic particles derived from atmospheric measurements.* Environmental Science and Technology, 46, 12, pp. 6523–6529, 2012.

[19] P. Wåhlin, R. Berkowicz, and F. Palmgren. *Wear and environmental aspects of composite materials for automotive braking industry.* Atmospheric Environment, 40, 12, pp. 2151–2159, 2006.

[20] S. Lawrence, R. Sokhi, K. Ravindra, H. Mao, H. D. Prain, and I. D. Bull. *Source apportionment of traffic emissions of particulate matter using tunnel measurements.* Atmospheric Environment, 77, pp. 548–557, 2013.

[21] Umwelt Bundesamt. *Feinstaub-Belastung.* `https://www.umweltbundesamt.de/daten/luft/feinstaub-belastung#textpart-1`, 2019. [Online; accessed 04-June-2019].

[22] The LOWBRASYS project partners and the European Commission. *The LOWBRASYS project.* `http://www.lowbrasys.eu/en/`, 2015. [Online; accessed 7-June-2019].

[23] PMP-Group. *Particle Measurement Program (PMP) of the United Nations Working Party on pollution and energy (UNECE-GRPE).* `https://wiki.unece.org/pages/viewpage.action?pageId=2523173`, 2019. [Online; accessed 12-Feb-2019].

[24] B. D. Garg, S. H. Cadle, P. A. Mulawa, P. J. Groblicki, C. Laroo, and G. A. Parr. *Brake wear particulate matter emissions.* Environmental Science and Technology, 34, 21, pp. 4463–4469, 2000.

[25] P. G. Sanders, T. M. Dalka, M. M. Maricq, and R. H. Basch. *Brake dynamometer measurement of airborne brake wear debris.* SAE 2002 World Congress, 2002.

[26] G. Perricone, J. Wahlström, and U. Olofsson. *Towards a test stand for standardized measurements of the brake emissions.* Proceedings of the Institution of Mechanical Engineers, Part D: Journal of Automobile Engineering, 230, 11, pp. 1521–1528, 2015.

[27] P. A. Baron, K. Willeke, and P. Kulkarni. *Aerosol Measurement: Principles, Techniques, and Applications*. Wiley & Sons, 3rd ed., 2011.

[28] U. Baltensperger, S. Nyeki, and M. Kalberer. *Atmospheric Particulate Matter*. In: C. N. Hewitt and A. V. Jackson. *Handbook of Atmospheric Science: Principles and Applications*. Blackwell Science Ltd, 2003.

[29] M. Mathissen. *Development of experimental methods to investigate non-exhaust particle emissions from a light duty vehicle*. Doctoral thesis, Bergische Universität Wuppertal, 2012.

[30] W. Hinds. *Aerosol Technology: Properties, Behavior, and Measurement of Airborne Particles*. Wiley, 2nd ed., 2012.

[31] J. F. Davis. *Aerosol in the atmosphere*. `https://allaboutaerosol.com/aerosol-in-the-atmosphere/`, 2019. [Online; accessed 29-Apr-2019].

[32] TSI Incorporated. *Aerodynamic Particle Sizer Model 3321. Theory of operation*. Brochure, 2012.

[33] Dekati Ltd. *PM10 Impactor*. Brochure, 2018.

[34] TSI Incorporated. *Dusttrak II Aerosolmonitore. Modelle 8530 8530EP und 8532*. Brochure, 2014.

[35] TSI Incorporated. *Optical Particle Sizer Model 3330*. Manual.

[36] TSI Incorporated. *Engine Exhaust Particle Sizer Spectrometer Model 3090*. Brochure, 2016.

[37] TSI Incorporated. *Engine Exhaust Particle Sizer Spectrometer Model 3090*. Manual.

[38] Dekati Ltd. *ELPI+*. Manual, 2016.

[39] Dekati Ltd. *ELPI+*. Brochure, 2018.

[40] B. Breuer and K. H. Bill. *Bremsenhandbuch*. Springer Vieweg, 4th ed., 2013.

[41] M. Eriksson. *Friction and contact phenomena of disc brakes related to squeal*. Doctoral thesis, Uppsala University, 2000.

[42] P. A. Tipler and G. Mosca. *Physik*. Spektrum, 6th ed., 2009.

[43] M. Eriksson, F. Bergman, and S. Jacobson. *On the nature of tribological contact in automotive brakes*. Wear, 252, pp. 26–36, 2002.

[44] J. Bijwe. *Composites as friction materials: Recent developments in non-asbestos fiber reinforced friction materials - a review*. Polymer Composites, 18, 3, pp. 378–396, 1997.

[45] G. W. Stachowiak and D. Chan. *Review of automotive brake friction materials*. Proceedings of the Institution of Mechanical Engineers, Part D: Journal of Automobile Engineering, 218, 9, pp. 953–966, 2004.

[46] A. Thorpe and R. M. Harrison. *Sources and properties of non-exhaust particulate matter from road traffic: A review*. Science of the Total Environment, 400, 1-3, pp. 270–282, 2008.

[47] T. Grigoratos and G. Martini. *Brake wear particle emissions: A review*. Environmental Science and Pollution Research, 22, 4, pp. 2491–2504, 2015.

[48] M. Alemani. *Particle emissions from car brakes: The influence of contact conditions on the pad-to-rotor interface*. Doctoral thesis, KTH Royal Institute of Technology, 2017.

[49] M. Eriksson, J. Lord, and S. Jacobson. *Wear and contact conditions of brake pads: Dynamical in situ studies of pad on glass*. Wear, 249, 3-4, pp. 272–278, 2001.

[50] A. Day. *Braking of Road Vehicles*. Butterworth-Heinemann, 1st ed., 2014.

[51] J. Grochowicz and T. Grabiec. *Potential for commonization of brake testing for globally marketed vehicles*. SAE International, 2009.

[52] Y. M. Chan, P. Agamuthu, and R. Mahalingam. *Solidification and stabilization of asbestos waste from an automobile brake manufacturing facility using cement*. Journal of Hazardous Materials, 77, 1-3, pp. 209–226, 2000.

[53] R. A. Lemen. *Asbestos in brakes: Exposure and risk of disease*. American Journal of Industrial Medicine, 45, 3, pp. 229–237, 2004.

[54] V. Roubicek, H. Raclavska, D. Juchelkova, and P. Filip. *Wear and environmental aspects of composite materials for automotive braking industry.* Wear, 265, 1-2, pp. 167–175, 2008.

[55] K. W. Liew and U. Nirmal. *Frictional performance evaluation of newly designed brake pad materials.* Materials and Design, 48, pp. 25–33, 2013.

[56] P. G. Boulter, A. J. Thorpe, R. M. Harrison, and A. G. Allen. *Road vehicle non-exhaust particulate matter: Final report on emission modelling.* Report, 2006.

[57] P. C. Verma, L. Menapace, A. Bonfanti, R. Ciudin, S. Gialanella, and G. Straffelini. *Braking pad-disc system: Wear mechanisms and formation of wear fragments.* Wear, 322-323, pp. 251–258, 2015.

[58] M. Eriksson, F. Bergman, and S. Jacobson. *Surface characterisation of brake pads after running under silent and squealing conditions.* Wear, 232, 2, pp. 163–167, 1999.

[59] W. Österle, M. Griepentrog, T. Gross, and I. Urban. *Chemical and microstructural changes induced by friction and wear of brakes.* Wear, 251, pp. 1469–1476, 2001.

[60] W. Österle and I. Urban. *Friction layers and friction films on PMC brake pads.* Wear, 257, 1-2, pp. 215–226, 2004.

[61] W. Österle, C. Prietzel, and A. I. Dmitriev. *Investigation of surface film nanostructure and assessment of its impact on friction force stabilization during automotive braking.* International Journal of Materials Research, 101, 5, pp. 669–675, 2010.

[62] P. Filip, L. Kovarik, and M. A. Wright. *Automotive brake lining characterization.* SAE International, p. 21, 1997.

[63] J. Kukutschova, V. Roubicek, K. Malachova, Z. Pavlickova, R. Holuza, J. Kubackova, D. MacCrimmon, and P. Filip. *Wear mechanism in automotive brake materials, wear debris and its potential environmental impact.* Wear, 267, 5, pp. 807–817, 2009.

[64] W. Österle and I. Urban. *Third body formation on brake pads and rotors.* Tribology International, 39, 5, pp. 401–408, 2006.

[65] M. Eriksson and S. Jacobson. *Tribological surfaces of organic brake pads.* Tribology International, 33, 12, pp. 817–827, 2000.

[66] G. P. Ostermeyer. *On the dynamics of the friction coefficient.* Wear, 254, 9, pp. 852–858, 2003.

[67] S. Lim and M. Ashby. *Overview no. 55 wear-mechanism maps.* Acta Metallurgica, 35, pp. 1–24, 1987.

[68] J. K. Gietl, R. Lawrence, A. J. Thorpe, and R. M. Harrison. *Identification of brake wear particles and derivation of a quantitative tracer for brake dust at a major road.* Atmospheric Environment, 44, 2, pp. 141–146, 2010.

[69] J. Kukutschova, P. Moravec, V. Tomasek, V. Matejka, J. Smolik, J. Schwarz, J. Seidlerova, K. Safarova, and P. Filip. *On airborne nano/micro-sized wear particles released from low-metallic automotive brakes.* Environmental Pollution, 159, 4, pp. 998–1006, 2011.

[70] M. Federici, C. Menapace, A. Moscatelli, S. Gialanella, and G. Straffelini. *Effect of roughness on the wear behavior of HVOF coatings dry sliding against a friction material.* Wear, 368-369, pp. 326–334, 2016.

[71] C. Menapace, M. Leonardi, V. Matějka, S. Gialanella, and G. Straffelini. *Dry sliding behavior and friction layer formation in copper-free barite containing friction materials.* Wear, 398-399, pp. 191–200, 2018.

[72] M. Mosleh, P. J. Blau, and D. Dumitrescu. *Characteristics and morphology of wear particles from laboratory testing of disk brake materials.* Wear, 256, 11-12, pp. 1128–1134, 2004.

[73] U. Olofsson, L. Olander, and A. Jansson. *A study of airborne wear particles generated from a sliding contact.* Journal of Tribology, 131, 4, 2009.

[74] J. Wahlström, A. Söderberg, L. Olander, A. Jansson, and U. Olofsson. *A pin-on-disc simulation of airborne wear particles from disc brakes.* Wear, 268, 5-6, pp. 763–769, 2010.

[75] M. Alemani, O. Nosko, I. Metinoz, and U. Olofsson. *A study on emission of airborne wear particles from car brake friction pairs.* SAE International Journal of Materials and Manufacturing, 9, 1, 2015.

[76] O. Nosko, J. Vanhanen, and U. Olofsson. *Emission of 1.3-10 nm airborne particles from brake materials.* Aerosol Science and Technology, 51, 1, pp. 91–96, 2016.

[77] O. Nosko and U. Olofsson. *Quantification of ultrafine airborne particulate matter generated by the wear of car brake materials.* Wear, 374-375, pp. 92–96, 2017.

[78] S. Cha, P. Carter, and R. Bradow. *Simulation of automobile brake wear dynamics and estimation of emissions.* SAE International, 1983.

[79] P. G. Sanders, N. Xu, T. M. Dalka, and M. M. Maricq. *Airborne brake wear debris: Size distributions, composition, and a comparison of dynamometer and vehicle tests.* Environmental Science and Technology, 37, 18, pp. 4060–4069, 2003.

[80] O. von Uexküll, S. Skerfving, R. Doyle, and M. Braungart. *Antimony in brake pads - a carcinogenic component?* Journal of Cleaner Production, 13, 1, pp. 19–31, 2005.

[81] A. Iijima, K. Sato, K. Yano, H. Tago, M. Kato, H. Kimura, and N. Furuta. *Particle size and composition distribution analysis of automotive brake abrasion dusts for the evaluation of antimony sources of airborne particulate matter.* Atmospheric Environment, 41, 23, pp. 4908–4919, 2007.

[82] A. Iijima, K. Sato, K. Yano, M. Kato, K. Kozawa, and N. Furuta. *Emission factor for antimony in brake abrasion dusts as one of the major atmospheric antimony sources.* Environmental Science and Technology, 42, 8, pp. 2937–2942, 2008.

[83] M. Riediker, M. Gasser, A. Perrenoud, P. Gehr, and B. Rothen-Rutishauser. *A system to test the toxicity of brake wear particles.* 12$^{\text{th}}$ International ETH-Conference on Combustion Generated Nanoparticles, 2008.

[84] J. Wahlström. *Towards a simulation methodology for prediction of airborne wear particles from disc brakes.* Licentiate thesis, 2009.

[85] J. Wahlström, L. Olander, and U. Olofsson. *Size, shape, and elemental composition of airborne wear particles from disc brake materials.* Tribology Letters, 38, 1, pp. 15–24, 2009.

[86] K. Augsburg, R. Horn, and H. Sachse. *Characterization of particulate emissions of vehicle wheel brakes.* 56$^{\text{th}}$ International Scientific Colloquium - Ilmenau University of Technology, 2011.

[87] K. Augsburg, H. Sachse, S. Krischok, R. Horn, M. Rieker, and U. Dierks. *Investigation of brake wear particles.* Report, 2012.

[88] H. Hagino, M. Oyama, and S. Sasaki. *Airborne brake wear particle emission due to braking and accelerating.* Wear, 334-335, pp. 44–48, 2015.

[89] H. Hagino, M. Oyama, and S. Sasaki. *Laboratory testing of airborne brake wear particle emissions using a dynamometer system under urban city driving cycles.* Atmospheric Environment, 131, pp. 269–278, 2016.

[90] G. Perricone, M. Alemani, I. Metinoz, V. Matějka, J. Wahlström, and U. Olofsson. *Towards the ranking of airborne particle emissions from car brakes - a system approach.* Proceedings of the Institution of Mechanical Engineers, Part D: Journal of Automobile Engineering, 2016.

[91] F. H. Farwick zum Hagen, M. Mathissen, T. Grabiec, T. Hennicke, M. Rettig, J. Grochowicz, R. Vogt, and T. Benter. *Brake wear particle measurement setup for quantitative emission analysis.* EuroBrake, EB2017-MDS-016, 2017.

[92] F. H. Farwick zum Hagen, M. Mathissen, T. Grabiec, T. Hennicke, M. Rettig, J. Grochowicz, R. Vogt, and T. Benter. *Study of brake wear particle emissions: Impact of braking and cruising conditions.* Environmental Science and Technology, 53, 9, pp. 5143–5150, 2019.

[93] K. Augsburg, D. Hesse, F. Wenzel, and G. Eichner. *Measuring and characterization of brake dust particles.* EuroBrake, EB2017-VDT-040, 2017.

[94] S. Gramstat, A. Cserhati, D. Lugovyy, and M. Schröder. *Investigations of brake particle emissions - testing method, vehicle preculiarities and friction material influence.* EuroBrake, EB2017-VDT-016, 2017.

[95] D. Lugovyy, M. Schröder, S. Gramstat, and R. Waninger. *Brake particle emissions - characterization of brake lining materials.* EuroBrake, EB2018-VDT-016, 2018.

[96] C. Agudelo, P. Deacon, A. Tiwari, A. Hortet, R. Anderson, R. Markiewicz, and M. Marschall. *Systematic assessment of the influence of test setup, test procedure, and friction material on brake emissions during inerta dynamometer tests.* EuroBrake, EB2017-VDT-026, 2017.

[97] I. Plenne, C. Nickolaus, D. Welp, R. Steege, R. Reuter, J. Lange, Z. Hadzhiivanov, and M. Samel. *Investigation of brake emission reduction potentials of different measures.* EuroBrake, EB2018-VDT-013, 2018.

[98] J. LaDou, P. Landrigan, J. C. Bailar, V. Foa, and A. Frank. *A call for an international ban on asbestos.* CMAJ: Canadian Medical Association Journal, 164, 4, pp. 489–490, 2001.

[99] J. Kukutschova, V. Roubicek, M. Maslan, D. Jancik, V. Slovak, K. Malachova, Z. Pavlickova, and P. Filip. *Wear performance and wear debris of semimetallic automotive brake materials.* Wear, 268, 1-2, pp. 86–93, 2010.

[100] H. G. Namgung, J. B. Kim, S. H. Woo, S. Park, M. Kim, M. S. Kim, G. N. Bae, D. Park, and S. B. Kwon. *Generation of nanoparticles from friction between railway brake disks and pads.* Environmental Science and Technology, 50, 7, pp. 3453–3461, 2016.

[101] H.-G. Namgung, J. B. Kim, M.-S. Kim, M. Kim, S. Park, S.-H. Woo, G.-N. Bae, D. Park, and S.-B. Kwon. *Size distribution analysis of airborne wear particles released by subway brake system.* Wear, 372-373, pp. 169–176, 2017.

[102] M. Mathissen, V. Scheer, R. Vogt, and T. Benter. *Investigation on the potential generation of ultrafine particles from the tire-road interface.* Atmospheric Environment, 45, 34, pp. 6172–6179, 2011.

[103] J. H. Kwak, H. Kim, J. Lee, and S. Lee. *Characterization of non-exhaust coarse and fine particles from on-road driving and laboratory measurements.* Science of the Total Environment, 458-460, pp. 273–282, 2013.

[104] J. Kwak, S. Lee, and S. Lee. *On-road and laboratory investigations on non-exhaust ultrafine particles from the interaction between the tire and road pavement under braking conditions.* Atmospheric Environment, 97, pp. 195–205, 2014.

[105] J. Wahlström and U. Olofsson. *A field study of airborne particle emissions from automotive disc brakes.* Proceedings of the Institution of Mechanical Engineers, Part D: Journal of Automobile Engineering, 229, 6, pp. 747–757, 2014.

[106] M. Abu-Allaban, J. A. Gillies, A. W. Gertler, R. Clayton, and D. Proffitt. *Tailpipe, resuspended road dust, and brake-wear emission factors from on-road vehicles.* Atmospheric Environment, 37, 37, pp. 5283–5293, 2003.

[107] N. Bukowiecki, P. Lienemann, M. Hill, R. Figi, A. Richard, M. Furger, K. Rickers, G. Falkenberg, Y. Zhao, S. S. Cliff, A. S. Prévôt, U. Baltensperger, B. Buchmann, and R. Gehrig. *Real-world emission factors for antimony and other brake wear related trace elements: Size-segregated values for light and heavy duty vehicles.* Environmental Science and Technology, 43, 21, pp. 8072–8078, 2009.

[108] T. Grigoratos and M. Giorgio. *Non-exhaust traffic related emissions. Brake and tyre wear PM.* Report, JRC, 2014.

[109] J. J. Schauer, G. C. Lough, M. M. Shafer, W. F. Christensen, M. F. Arndt, J. T. DeMinter, and J.-S. Park. *Characterization of metals emitted from motor vehicles.* Research report (Health Effects Institute), 3, 133, 2006.

[110] M. P. Keuken, M. Moerman, M. Voogt, M. Blom, E. P. Weijers, T. Röckmann, and U. Dusek. *Source contributions to PM2.5 and PM10 at an urban background and a street location.* Atmospheric Environment, 71, pp. 26–35, 2013.

[111] G. Dongarra, E. Manno, and D. Varrica. *Possible markers of traffic-related emissions.* Environmental Monitoring and Assessment, 154, 1-4, pp. 117–125, 2009.

[112] J. Pey, X. Querol, and A. Alastuey. *Discriminating the regional and urban contributions in the North-Western Mediterranean: PM levels and composition.* Atmospheric Environment, 44, 13, 2010.

[113] P. Pant and R. M. Harrison. *Estimation of the contribution of road traffic emissions to particulate matter concentrations from field measurements: A review.* Atmospheric Environment, 77, pp. 78–97, 2013.

[114] J. Wahlström, A. Söderberg, L. Olander, and U. Olofsson. *A disc brake test stand for measurement of airborne wear particles.* Lubrication Science, 21, 6, pp. 241–252, 2009.

[115] A. Rauterberg-Wulff. *Beitrag des Reifen- und Bremsenabriebs zur Russemission an Strassen.* VDI-Verlag, 1998.

[116] L. Luhana, R. Sokhi, L. Warner, H. Mao, P. Boulter, I. McCrae, W. Julian, and D. Osborn. *Characterisation of exhaust particulate emissions from road vehicles (PARTICULATES).* European Commission - DG TrEn, 5$^{\text{th}}$ Framework Programme, 2004.

[117] B. Y. H. Liu and J. K. Agarwal. *Experimental observation of aerosol deposition in turbulent flow.* Journal of Aerosol Science, 5, 2, pp. 145–148, 1974.

[118] S. K. Friedlander. *Smoke, Dust and Haze: Fundamentals of Aerosol Behavior.* Wiley-Interscience, 1977.

[119] N. Yamano and J. E. Brockmann. *Aerosol sampling and transport efficiency calculation (ASTEC) and application to surtsey/DCH aerosol sampling system.* Sandia National Laboratories, Albuquerque, NM, 20, 21, p. 157, 1989.

[120] D. Y. H. Pui, F. Romay-Novas, and B. Y. H. Liu. *Experimental study of particle deposition in bends of circular cross section.* Aerosol Science and Technology, 7, 3, pp. 301–315, 1987.

[121] A. R. McFarland, H. Gong, A. Muyshondt, W. B. Wente, and N. K. Anand. *Aerosol deposition in bends with turbulent flow.* Environmental Science and Technology, 31, pp. 3371–3377, 1997.

[122] R. I. Crane and R. L. Evans. *Inertial deposition in a bent pipe.* Journal of Aerosol Science, 8, 3, pp. 161–170, 1977.

[123] S. P. Belyaev and L. M. Levin. *Techniques for collection of representative aerosol samples.* Aerosol Science, 5, pp. 325–338, 1974.

[124] International Organization for Standardization. *Stationary source emissions - manual determination of mass concentration of particulate matter.* Norm: ISO 9096:2017(en), 2017.

[125] TSI Incorporated. *Indoor air quality handbook.* Handbook, 2013.

[126] S. P. Belyaev and L. M. Levin. *Investigation of aerosol aspiration by photographing particle tracks under flash illumination.* Aerosol Science, 3, pp. 127–140, 1972.

[127] M. Mathissen, J. Grochowicz, C. Schmidt, R. Vogt, F. H. Farwick zum Hagen, T. Grabiec, H. Steven, and T. Grigoratos. *A novel real-world braking cycle for studying brake wear particle emissions.* Wear, 414-415, pp. 219–226, 2018.

[128] M. Mathissen and C. Evans. *Lowbrasys brake wear cycle - 3h-LACT.* Mendeley data, 2019.

[129] M. Mathissen, J. Grochowicz, C. Schmidt, R. Vogt, F. H. Farwick zum Hagen, T. Grabiec, H. Steven, and T. Grigoratos. *WLTP-based real-world brake wear cycle.* Mendeley data, 2018.

[130] F. Talati and S. Jalalifar. *Analysis of heat conduction in a disk brake system.* Heat and Mass Transfer, 45, 8, pp. 1047–1059, 2009.

[131] A. Mamakos, M. Arndt, D. Hesse, F. Wenzel, and K. Augsburg. *Particle emissions from different types of brake pads - particle number results.* Report, 45$^{\text{th}}$ PMP meeting, 2017.

[132] G. Perricone, V. Matějka, M. Alemani, J. Wahlström, and U. Olofsson. *A test stand study on the volatile emissions of a passenger car brake assembly.* Atmosphere, 10, 5, 2019.

[133] M. Alemani, J. Wahlström, and U. Olofsson. *On the influence of car brake system parameters on particulate matter emissions.* Wear, 396-397, pp. 67–74, 2018.

[134] F. H. Farwick zum Hagen, M. Mathissen, T. Grabiec, T. Hennicke, M. Rettig, J. Grochowicz, R. Vogt, and T. Benter. *On-road vehicle measurements of brake wear particle emissions.* Atmospheric Environment, 217, 2019.

[135] M. Mathissen, V. Scheer, F. Farwick zum Hagen, T. Grabiec, and T. Hennicke. *Vorrichtung und Verfahren zur Messung von Bremspartikelemissionen.* Patent, DE 10 2017 200 941 B4, Deutsches Patent- und Markenamt, 2019.

[136] M. Mathissen, V. Scheer, U. Kirchner, R. Vogt, and T. Benter. *Non-exhaust pm emission measurements of a light duty vehicle with a mobile trailer.* Atmospheric Environment, 59, pp. 232–242, 2012.

[137] H. Tsukahara, T. Ishida, and M. Mayumi. *Gas-phase oxidation of nitric oxide: Chemical kinetics and rate constant.* Nitric Oxide: Biology and Chemistry, 3, 3, pp. 191–198, 1999.

[138] J. Wahlström, Y. Lyu, V. Matějka, and A. Söderberg. *A pin-on-disc tribometer study of disc brake contact pairs with respect to wear and airborne particle emissions.* Wear, 384-385, pp. 124–130, 2017.

[139] J. Vlcek, L. Drongova, M. Topinkova, V. Matejka, J. Kukutschova, M. Vavro, and V. Tomkova. *Identification of phase composition of binders from alkali-activated mixtures of granulated blast furnace slag and fly ash.* Ceramics-Silikaty, 58, 1, pp. 79–88, 2014.

[140] J. H. J. Hulskotte, G. D. Roskam, and H. A. C. Denier van der Gon. *Elemental composition of current automotive braking materials and derived air emission factors.* Atmospheric Environment, 99, pp. 436–445, 2014.

[141] Ricardo. *Air quality modelling on the contribution of brake wear emissions to particulate matter concentrations using a high-resolution brake use inventory.* FAT-Report, in press.

Erklärung der Urheberschaft

Hiermit versichere ich, Ferdinand H. Farwick zum Hagen, dass ich die vorliegende Arbeit selbstständig verfasst und keine anderen als die angegebenen Quellen und Hilfsmittel benutzt habe, dass alle Stellen der Arbeit, die wörtlich oder sinngemäß aus anderen Quellen übernommen wurden, als solche kenntlich gemacht sind und dass die Arbeit in gleicher oder ähnlicher Form noch keiner Prüfungsbehörde vorgelegt wurde.

Ort, Datum Unterschrift